

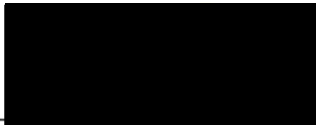
# Stoichiometry and Stability of Binary Phase Crystals Formed Between Acetylene and Nitrous Oxide/Carbon Dioxide


by

Terence Edward Rowat  
B.Sc., University of Victoria, 1993


A Thesis Submitted in Partial Fulfillment of the  
Requirements for the Degree of  
**MASTER OF SCIENCE**  
in the  
Department of Chemistry


We accept this thesis as conforming  
to the required standard

  
\_\_\_\_\_  
Dr. T. E. Gough, Supervisor (Department of Chemistry)

  
\_\_\_\_\_  
Dr. C. Böhne, Departmental Member (Department of Chemistry)

  
\_\_\_\_\_  
Dr. C. X. W. Qian, Departmental Member (Department of Chemistry)

  
\_\_\_\_\_  
Dr. R. K. Keeler, Outside Member (Department of Physics & Astronomy)

  
\_\_\_\_\_  
Dr. R. Illner, External Examiner (Department of Mathematics & Statistics)

© TERENCE EDWARD ROWAT, 1997

University of Victoria

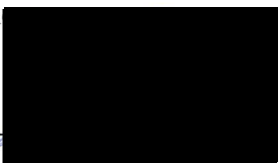
All rights reserved. This thesis may not be reproduced in whole or in part, by  
photocopy or other means, without the permission of the author.

Supervisor: Dr. T.E. Gough

## Abstract

Fourier transform infrared spectroscopy was used to record the spectra of crystalline films containing varying amounts of acetylene with either carbon dioxide or nitrous oxide. These binary films were prepared by pulsed expansion of the mixed gas onto a liquid nitrogen cooled window. The presence of new absorption bands indicate the presence of a binary phase with a concentration independent stoichiometry. The stoichiometry for the binary phase  $\text{CO}_2 \cdot \text{C}_2\text{H}_2$  was determined to be 1:1. Two binary phases (labelled  $\alpha$  and  $\beta$ ) of  $\text{N}_2\text{O} \cdot \text{C}_2\text{H}_2$  were also shown to have a 1:1 stoichiometry. The binary phase  $\text{CO}_2 \cdot \text{C}_2\text{H}_2$  was found to be metastable with respect to its pure phases. Evidence was shown which suggests the nuclei of formation of these binary phases are clusters formed in the early stages of the supersonic expansion.

Examin



---

Dr. T. E. Gough, Supervisor (Department of Chemistry)



---

Dr. C. Bohne, Departmental Member (Department of Chemistry)



---

Dr. C. X. W. Qian, Departmental Member (Department of Chemistry)



---

Dr. R. K. Keeler, Outside Member (Department of Physics & Astronomy)



---

Dr. R. Illner, External Examiner (Department of Mathematics & Statistics)

# Table of Contents

|                                  |             |
|----------------------------------|-------------|
| <b>Abstract</b>                  | <b>ii</b>   |
| <b>Table of Contents</b>         | <b>iv</b>   |
| <b>List of Tables</b>            | <b>vii</b>  |
| <b>List of Figures</b>           | <b>viii</b> |
| <b>Acknowledgements</b>          | <b>xii</b>  |
| <b>Dedication</b>                | <b>xiii</b> |
| <b>1 Introduction</b>            | <b>1</b>    |
| <b>2 Experimental Details</b>    | <b>4</b>    |
| 2.1 Introduction . . . . .       | 4           |
| 2.2 Sample Preparation . . . . . | 6           |
| 2.2.1 Gas Mixing Board . . . . . | 6           |
| 2.2.2 Cooled Window . . . . .    | 8           |

TABLE OF CONTENTS

v

|          |  |           |
|----------|--|-----------|
| 2.3      | Nozzle Performance . . . . .                                       | 9         |
| 2.3.1    | Free Jet Expansion . . . . .                                       | 11        |
| 2.3.2    | Cooled Equilibrium Cell . . . . .                                  | 13        |
| 2.4      | Interferometric Spectrometer . . . . .                             | 15        |
| 2.4.1    | Advantages of FTIR Spectrometers over Dispersive Instruments       | 23        |
| <b>3</b> | <b>The Carbon Dioxide - Acetylene Binary Phase</b>                 | <b>25</b> |
| 3.1      | Introduction . . . . .   | 25        |
| 3.2      | Experimental Conditions and Results . . . . .                      | 28        |
| 3.2.1    | Equilibrium Studies . . . . .                                      | 28        |
| 3.2.2    | Non-Equilibrium Studies . . . . .                                  | 32        |
| 3.3      | Discussion . . . . .   | 46        |
| 3.4      | Conclusion . . . . .   | 51        |
| <b>4</b> | <b>Nitrous Oxide - Acetylene Cryofilm</b>                          | <b>55</b> |
| 4.1      | Introduction . . . . .   | 55        |
| 4.2      | Experimental Conditions . . . . .                                  | 57        |
| 4.3      | Results . . . . .  | 67        |
| 4.4      | Discussion . . . . .   | 68        |
| <b>5</b> | <b>Growth and Stability of the Binary Phase</b>                    | <b>75</b> |
| 5.1      | The Stability of the Binary Phases . . . . .                       | 75        |
| 5.1.1    | The CO <sub>2</sub> ·C <sub>2</sub> H <sub>2</sub> Phase . . . . . | 76        |

|   |            |
|---|------------|
| <i>TABLE OF CONTENTS</i>  | vi         |
| 5.1.2 The $N_2O \cdot C_2H_2$ Phase . . . . .                     | 91         |
| 5.2 Nucleation and Growth of the Binary Phase . . . . .           | 99         |
| 5.2.1 Cluster Formation in a Free Jet Expansion . . . . .         | 99         |
| 5.2.2 Cluster Growth as a Precursor to Binary Formation . . . . . | 101        |
| 5.3 Discussion . . . . .  | 107        |
| <b>6 Summary</b>  | <b>111</b> |
| <b>Bibliography</b>   | <b>113</b> |

# List of Tables

|     |  |     |
|-----|--|-----|
| 3.1 | Experimental conditions used for the recording of spectra in the carbon dioxide - acetylene series . . . . . | 41  |
| 3.2 | Absorption frequencies ( $\text{cm}^{-1}$ ) of $\text{C}_2\text{H}_2$ and $\text{CO}_2$ . . . . .            | 42  |
| 3.3 | Relative intensities for acetylene $\nu_3$ and carbon dioxide $\nu_1 + \nu_3$ . . . . .                      | 50  |
| 4.1 | Experimental conditions used for the recording of spectra in the nitrous oxide - acetylene series . . . . .  | 65  |
| 4.2 | Absorption frequencies ( $\text{cm}^{-1}$ ) of $\text{C}_2\text{H}_2$ and $\text{N}_2\text{O}$ . . . . .     | 66  |
| 4.3 | Relative intensities for $\nu_3$ acetylene and $\nu_1 + \nu_3$ nitrous oxide. . . . .                        | 71  |
| 5.1 | Conversion of $\text{CO}_2 \cdot \text{C}_2\text{H}_2$ into pure components . . . . .                        | 83  |
| 5.2 | Exponents of Time in the Avrami Equation . . . . .   | 110 |

# List of Figures

|     |  |    |
|-----|--|----|
| 1.1 | The normal vibration modes of $C_2H_2$ . . . . .                                   | 3  |
| 1.2 | The normal vibration modes of $CO_2$ . . . . .                                     | 3  |
| 1.3 | The normal vibration modes of $N_2O$ . . . . .                                     | 3  |
| 2.1 | A schematic diagram of the experimental setup . . . . .                            | 5  |
| 2.2 | Apparatus used to prepare cryofilms . . . . .                                      | 7  |
| 2.3 | Nozzle geometries . . . . .  | 10 |
| 2.4 | Pressure build-up inside nozzle during a typical pulse . . . . .                   | 10 |
| 2.5 | Centerline properties versus distance in the free jet . . . . .                    | 14 |
| 2.6 | Cooled solution cell . . . . .   | 16 |
| 2.7 | Schematic of the BOMEM interferometric spectrometer . . . . .                      | 18 |
| 2.8 | Typical interferogram . . . . .  | 19 |
| 3.1 | Spectra of an equimolar $CO_2$ - $C_2H_2$ mixture in the equilibrium cell. . . . . | 30 |
| 3.2 | Pure acetylene spectra showing lattice translation modes . . . . .                 | 31 |

|      |  |    |
|------|--|----|
| 3.3  | Spectra of the $\nu_1+\nu_3$ band of $\text{CO}_2$ for various $\text{CO}_2\text{-C}_2\text{H}_2$ mixtures rich in $\text{CO}_2$ . . . . .   | 35 |
| 3.4  | Spectra of the $\nu_1+\nu_3$ band of $\text{CO}_2$ for various $\text{CO}_2\text{-C}_2\text{H}_2$ mixtures containing roughly equal amounts of $\text{CO}_2$ and $\text{C}_2\text{H}_2$ . . . . .                          | 36 |
| 3.5  | Spectra of the $\nu_1+\nu_3$ band of $\text{CO}_2$ for various $\text{CO}_2\text{-C}_2\text{H}_2$ mixtures rich in $\text{C}_2\text{H}_2$ . . . . .  | 37 |
| 3.6  | Spectra of the $\nu_3$ band of $\text{C}_2\text{H}_2$ for various $\text{CO}_2\text{-C}_2\text{H}_2$ mixtures rich in $\text{CO}_2$ . . . . .  | 38 |
| 3.7  | Spectra of the $\nu_3$ band of $\text{C}_2\text{H}_2$ for various $\text{CO}_2\text{-C}_2\text{H}_2$ mixtures rich in $\text{CO}_2$ containing roughly equal amounts of $\text{CO}_2$ and $\text{C}_2\text{H}_2$ . . . . . | 39 |
| 3.8  | Spectra of the $\nu_3$ band of $\text{C}_2\text{H}_2$ for various $\text{CO}_2\text{-C}_2\text{H}_2$ mixtures rich in $\text{C}_2\text{H}_2$ . . . . .   | 40 |
| 3.9  | Spectra of the $\nu_2$ band of $\text{C}_2\text{H}_2$ in the binary phase . . . . .  | 47 |
| 3.10 | Intensity ratio of acetylene to carbon dioxide . . . . .   | 53 |
| 3.11 | Systematic variation graph for the $\text{CO}_2\text{-C}_2\text{H}_2$ system . . . . .   | 54 |
| 4.1  | Spectra of the $\nu_1+\nu_3$ band of $\text{N}_2\text{O}$ for various $\text{N}_2\text{O-C}_2\text{H}_2$ mixtures rich in $\text{N}_2\text{O}$ . . . . .   | 59 |
| 4.2  | Spectra of the $\nu_1+\nu_3$ band of $\text{N}_2\text{O}$ for various $\text{N}_2\text{O-C}_2\text{H}_2$ mixtures containing roughly equal amounts of $\text{N}_2\text{O}$ and $\text{C}_2\text{H}_2$ . . . . .            | 60 |
| 4.3  | Spectra of the $\nu_1+\nu_3$ band of $\text{N}_2\text{O}$ for various $\text{N}_2\text{O-C}_2\text{H}_2$ mixtures rich in $\text{C}_2\text{H}_2$ . . . . .   | 61 |

|      |  |    |
|------|--|----|
| 4.4  | Spectra of the $\nu_3$ band of $C_2H_2$ for various $N_2O$ - $C_2H_2$ mixtures rich in $N_2O$ . . . . .  | 62 |
| 4.5  | Spectra of the $\nu_3$ band of $C_2H_2$ for various $N_2O$ - $C_2H_2$ mixtures containing roughly equal amounts of $N_2O$ and $C_2H_2$ . . . . . | 63 |
| 4.6  | Spectra of the $\nu_3$ band of $C_2H_2$ for various $N_2O$ - $C_2H_2$ mixtures rich in $C_2H_2$ . . . . .  | 64 |
| 4.7  | Spectra of the $\nu_2$ band of $C_2H_2$ in the binary phase . . . . .  | 69 |
| 4.8  | Intensity ratio of acetylene to nitrous oxide . . . . .  | 70 |
| 4.9  | Systematic variation graph for the $N_2O$ - $C_2H_2$ system . . . . .  | 73 |
| 4.10 | Systematic variation graph for the $N_2O$ - $C_2H_2$ system: $\alpha$ and $\beta$ amounts combined . . . . .                                     | 74 |
| 5.1  | Decomposition of $CO_2$ - $C_2H_2$ : the $\nu_1 + \nu_3$ region of $CO_2$ . . . . .  | 77 |
| 5.2  | Decomposition of $CO_2$ - $C_2H_2$ : the $\nu_3$ region of $C_2H_2$ . . . . .  | 78 |
| 5.3  | Decomposition of $CO_2$ - $C_2H_2$ : the $\nu_2$ region of $CO_2$ . . . . .  | 79 |
| 5.4  | Decomposition of $CO_2$ - $C_2H_2$ : the $\nu_5$ region of $C_2H_2$ . . . . .  | 80 |
| 5.5  | Graph showing conversion of the binary carbon dioxide-acetylene phase to pure components and fit to the Avrami equation . . . . .                | 82 |
| 5.6  | Determination of the value 'n' by manipulation of the Avrami equation  | 86 |
| 5.7  | Graph showing conversion of the binary carbon dioxide-acetylene phase to pure components and fit to the modified Avrami equation . . . . .       | 87 |
| 5.8  | Polynomial Fit to Fibrillar Model . . . . .  | 89 |

|      |  |     |
|------|--|-----|
| 5.9  | Decomposition of $\text{CO}_2\cdot\text{C}_2\text{H}_2$ : the $\nu_2$ region of $\text{CO}_2$ showing isosbestic points . . . . .          | 92  |
| 5.10 | Decomposition of $\text{CO}_2\cdot\text{C}_2\text{H}_2$ : the $\nu_5$ region of $\text{C}_2\text{H}_2$ showing isosbestic points . . . . . | 93  |
| 5.11 | Conversion of $\alpha\text{-N}_2\text{O}\cdot\text{C}_2\text{H}_2$ . . . . .   | 95  |
| 5.12 | Conversion of $\alpha\text{-N}_2\text{O}\cdot\text{C}_2\text{H}_2$ . . . . .   | 96  |
| 5.13 | Growth of the nitrous oxide-acetylene binary phases . . . . .  | 98  |
| 5.14 | Condensation of an Expanding Gas . . . . .   | 101 |
| 5.15 | Centerline pressure versus distance in the free jet . . . . .  | 103 |
| 5.16 | Equilibrium Geometry of Heteronuclear Dimers . . . . .   | 106 |

## Acknowledgements

I wish to extend my appreciation to every member of the Gough research group: Dr. Jack Barnes, Marko Banjavčić, Marcell Stoer, and TangYu Wang. They were always willing to lend a hand or a suggestion. I couldn't help but sharpen my science skills by just being around them.

I would like to thank my supervisor, Dr. Terry Gough, for being my mentor and sharing his wisdom with me.

I also wish to thank my parents, my wife's parents and my brothers for their encouragement. To Mama, your memory will always be an inspiration for me. Finally, my greatest debts of gratitude go to my soul-mate, Brenda, whose love and support I shall always cherish and to the Creator of this wonderfully complex universe.

To Brenda,

NEWTON  
JAN. 10. 1901

# Chapter 1

## Introduction

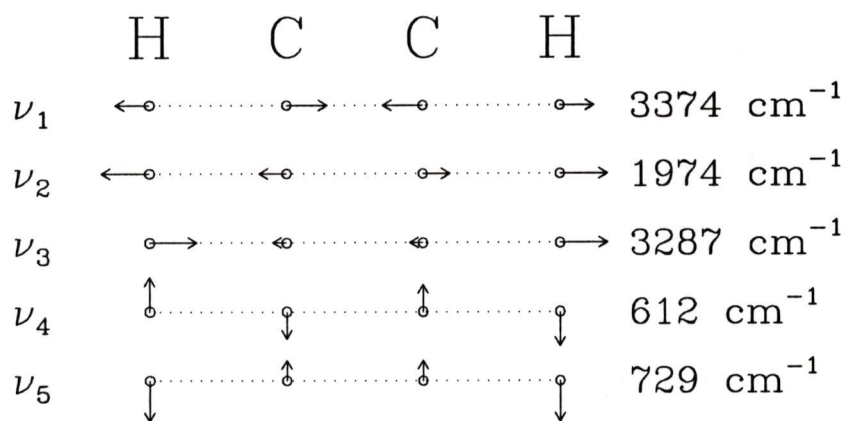
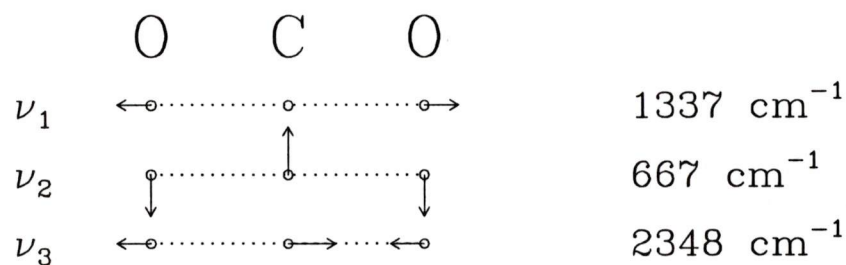
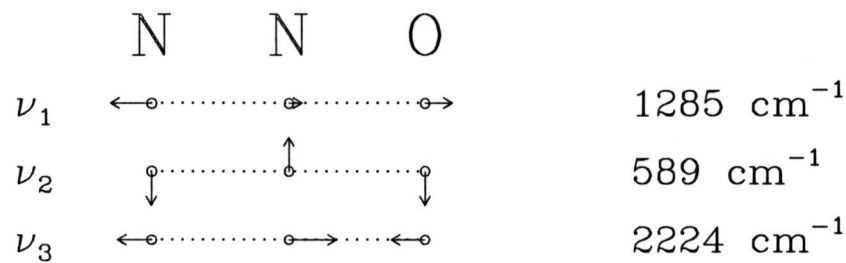
Recently, the presence of a novel binary phase containing carbon dioxide and acetylene has been identified in the infrared spectra of microcrystalline particles produced under the non-equilibrium conditions of a diffusive trapping cell [1, 2]. Evidence was presented showing that carbon dioxide and acetylene are present in the binary crystalline phase in a fixed molecular ratio, independent of initial mixture concentrations.

The purpose of this thesis was to prepare and study a bulk sample of the same crystalline phase. To our knowledge, this had not been done before. This was to be accomplished under equilibrium (i.e. slow cooling of a gas mixture through the liquid phase to the solid phase), if at all possible. If not, a method using conditions similar to those used in the diffusive trapping technique would be devised in order to produce a binary solid film. This would further enhance our ability to study this new

binary phase. The following questions could then, in time, be addressed: What is the stoichiometry of the binary phase? What is the crystal structure? How stable is the binary phase with respect to the pure phases of carbon dioxide and acetylene? What are the absolute intensities of infrared absorptions? Invariably, more questions would arise as the study progresses. Since infrared spectroscopy is the primary analysis tool in this thesis, we expect that questions such as crystal structure will not be fully answered.

This thesis will discuss the preparation and subsequent study of the crystalline binary phases containing carbon dioxide/acetylene or nitrous oxide/acetylene. Chapter 2 deals with the experimental details of the work including a brief introduction to Fourier transform spectroscopy. In Chapter 3, the method of preparation of the binary phase of carbon dioxide and acetylene is discussed as well as the determination of stoichiometry and relative intensities between selected infrared absorption bands. The same method of preparation and analysis is applied to a binary system of nitrous oxide and acetylene. The results are detailed in Chapter 4. The growth and stability of the binary phases are covered in Chapter 5. A brief summary and possible future work are given in Chapter 6.

The fundamental infrared vibrations of the gases used in this study are shown in Figures 1.1 to 1.3.

Figure 1.1: The normal vibration modes of  $\text{C}_2\text{H}_2$ .Figure 1.2: The normal vibration modes of  $\text{CO}_2$ .Figure 1.3: The normal vibration modes of  $\text{N}_2\text{O}$ .

## Chapter 2

# Experimental Details

### 2.1 Introduction

The bulk of the experimental work for this thesis required the use of a Fourier transform infrared (FTIR) spectrometer to observe the film that has been vapour deposited onto a cooled window. The apparatus consists of a gas mixing board, a supersonic nozzle, a zinc selenide window, a vacuum chamber and a BOMEM DA3.002 FTIR spectrophotometer. These details are shown in Figure 2.1. Control of the spectrophotometer, data collection, co-addition of scans, and Fourier transformation are performed by a 66 MHz-486 microcomputers. A second computer provides an interface between the control computer and the interferometer.

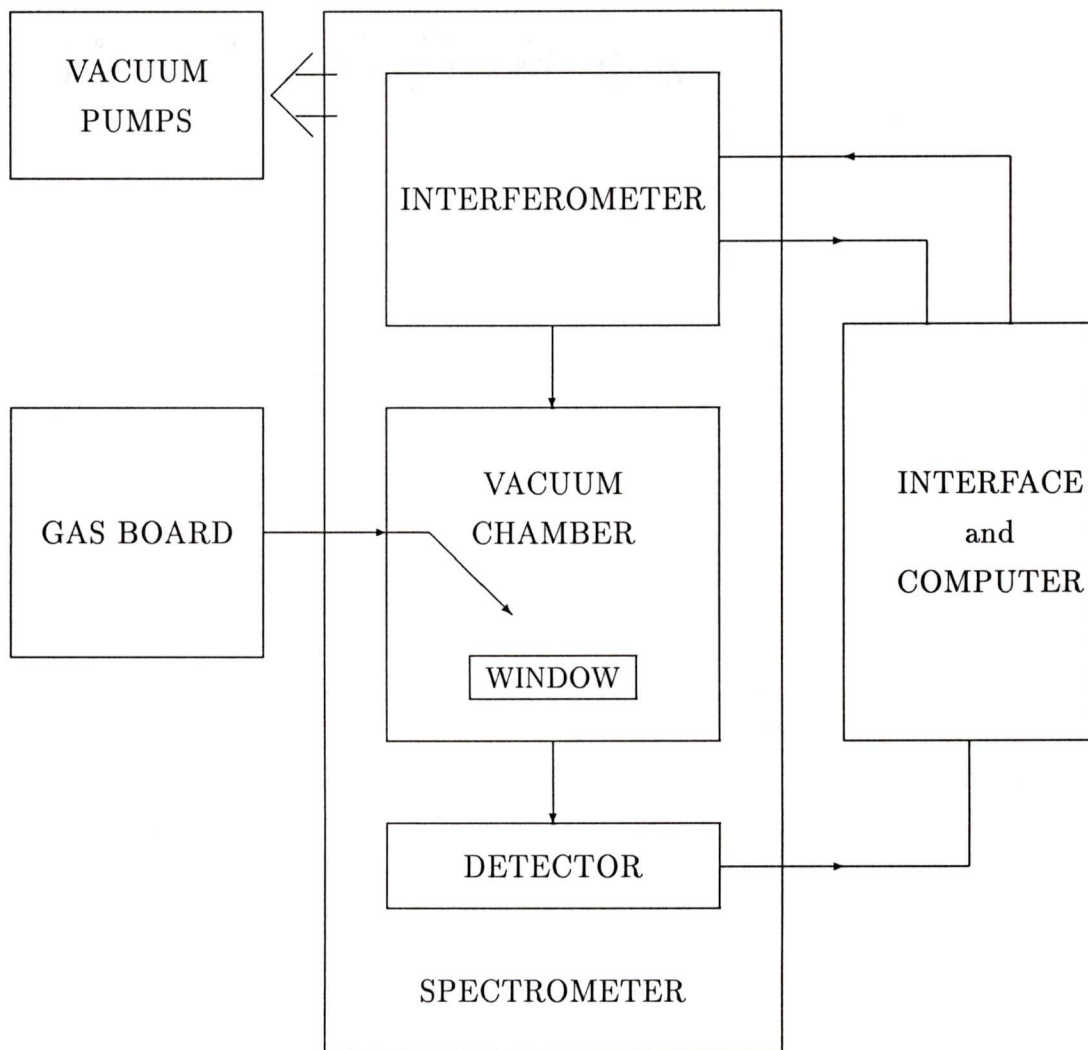


**Figure 2.1:** A schematic diagram of the experimental setup.

## 2.2 Sample Preparation

### 2.2.1 Gas Mixing Board

As shown in Figure 2.2 the systems carbon dioxide-acetylene and nitrous oxide-acetylene are mixed in known proportions by passing the gases each through a separate Side-Trak model 840 mass flow controller. The mass flow controllers were calibrated for their respective gas and are accurate to  $\pm 1\%$  of full scale linearity over 15 to 25°C. Typical flow range used in the calibration of each flow controller and in the study was 0.5 to 9.5 SCCM (standard cubic centimeters per minute). The gases combine in a mixing chamber filled with glass beads. The pressure in the mixing chamber is held constant by pumping the gas mixture from the chamber through a needle valve. A pulsed solenoid valve is also attached to the chamber. It is through this valve that the gas mixture is delivered to a liquid nitrogen cooled zinc selenide (ZnSe) window via a 200  $\mu\text{m}$  diameter nozzle.

The nozzle and cooled window are contained within a vacuum sample chamber. A rotary vacuum pump in conjunction with a liquid nitrogen cryopump maintains the pressure inside the sample chamber at approximately  $10^{-1}$  Torr. The primary purpose of the low pressure is to remove atmospheric water,  $\text{CO}_2$  and other contaminants. The vacuum chamber is situated in a BOMEM FTIR spectrometer in order to study the film deposited onto the cooled window spectroscopically.

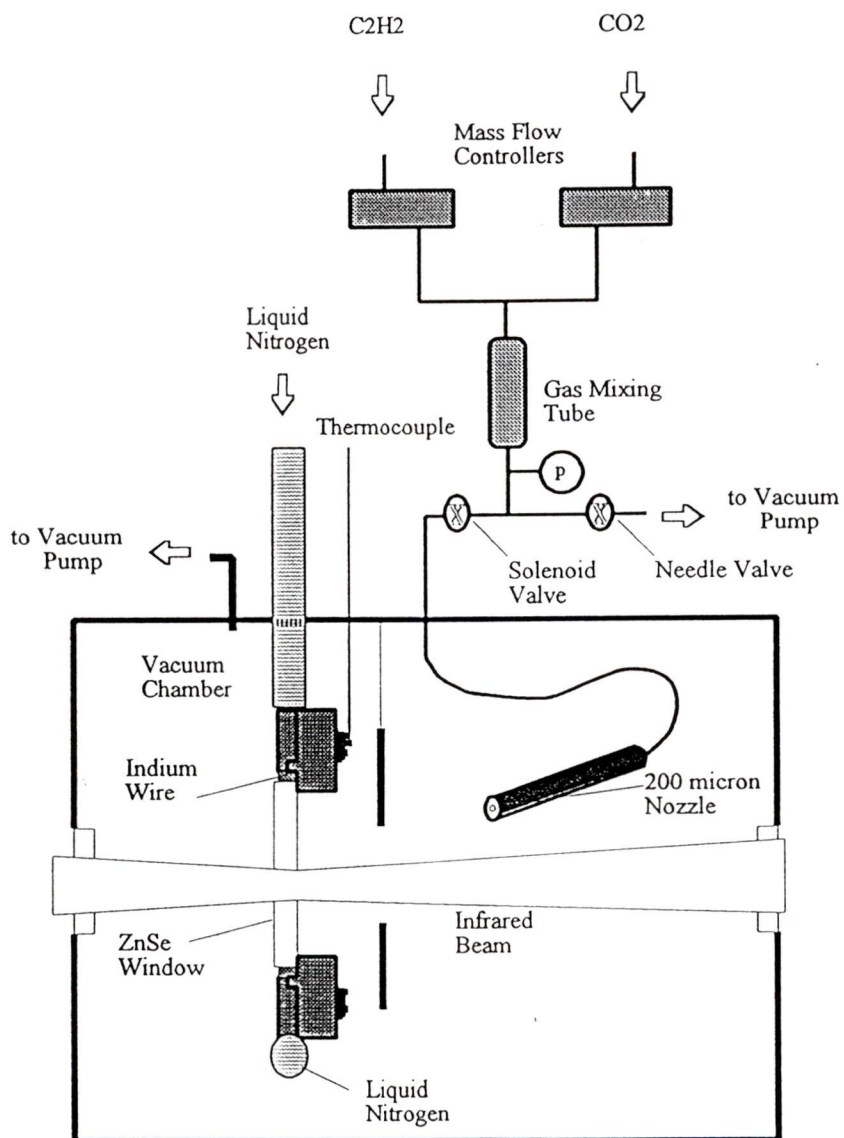


**Figure 2.2:** Gas mixing board, nozzle, and liquid nitrogen cooled ZnSe window used in the preparation of binary cryofilms.

### 2.2.2 Cooled Window

Zinc selenide has a low absorptivity; 70% transmission through a 10 mm thick window in the region 550 to 4000  $\text{cm}^{-1}$  [3]. It is extremely uniform, homogeneous, non-hygroscopic and chemically stable. As shown in Figure 2.2, brass flanges house the ZnSe window. Indium wire compressed between two brass flanges and against the edge of the window is used to hold the window and to provide a good thermal contact with the brass flanges [4]. Indium is soft and the thermal expansion coefficients of brass and ZnSe are very similar [5], allowing rapid and deep cooling of the assembly without cracking the window.

The temperature was held constant near 90 K by flowing liquid nitrogen through a 1/2 inch pipe soldered to one flange. A thermocouple is connected to the other brass flange to monitor the temperature. Because of the small volume of liquid nitrogen in the pipe with respect to the size of the window assembly, a low sample chamber pressure was necessary in order to cool the flanges down to near liquid nitrogen temperatures. It is assumed that the ZnSe window reaches the same temperature as the brass due to the high thermal conductivity of indium ( $0.837 \text{ W cm}^{-1} \text{ K}^{-1}$ ) [5] and the fair thermal conductivity of ZnSe ( $0.18 \text{ W cm}^{-1} \text{ K}^{-1}$ ) [3]. The temperature is held constant for several minutes to ensure that thermal equilibrium has been reached before any vapour is deposited onto the ZnSe window.

## 2.3 Nozzle Performance

Figure 2.3 shows the cross-sections of four nozzle geometries commonly used in molecular beam experiments. The nozzle used in this study is a 200  $\mu\text{m}$  diameter cylindrical nozzle having a circular orifice with a length-to-diameter ratio of approximately unity.

Computer generated electrical pulses were used to control the solenoid valve separating the nozzle from the mixing chamber. Pulse duration and interval timing was calibrated with an oscilloscope. The pressure inside the mixing chamber was usually held at 60 Torr. In most cases, the solenoid valve was set to open only once for a duration of 500 ms. In this period of time the stagnation pressure ( $P_0$ ) in the tubing between the solenoid valve and the nozzle orifice reached the same pressure as in the mixing chamber. Figure 2.4 shows the temporal build-up and subsequent decay of  $P_0$  inside the nozzle. The flow rate through the nozzle is pressure dependent ( $F \propto P_0 d^2$ ) and thus reaches a maximum at 500 ms. The flow rate at this pressure, calculated by the initial slope of the decay, was found to be 10.9 SCCM (standard cubic centimeters per minute). SCCM refers to the flow of 1  $\text{cm}^3$  of a gas at 1 atm and 0°C in one minute.

The setup described above should result in supersonic expansion flow from the nozzle. We believe that this condition is critical to the formation of the binary complex  $\text{CO}_2\cdot\text{C}_2\text{H}_2$ . The rationale behind this will be discussed in Chapter 5. A brief discussion on physical properties of the gas leaving the nozzle will be dealt with here.

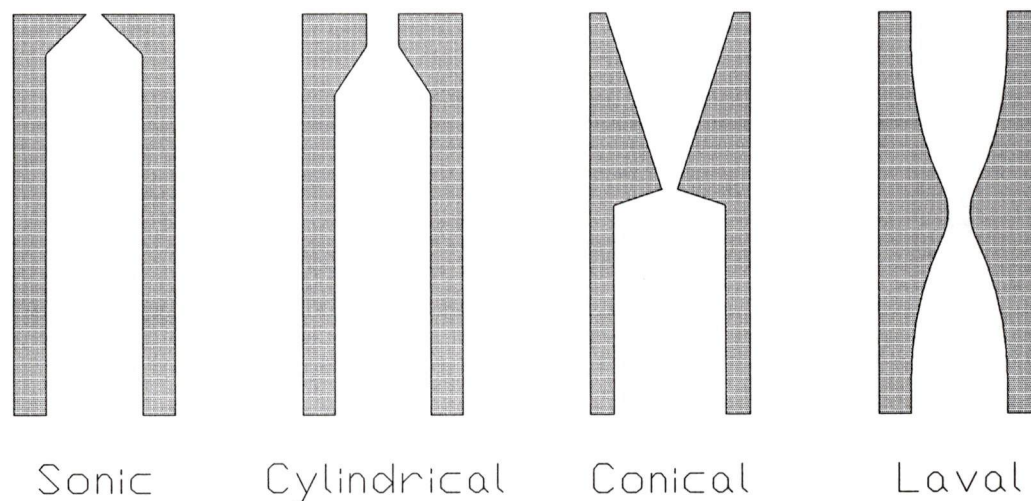


**Figure 2.3:** Cross-section of nozzle geometries used commonly in molecular beam experiments.

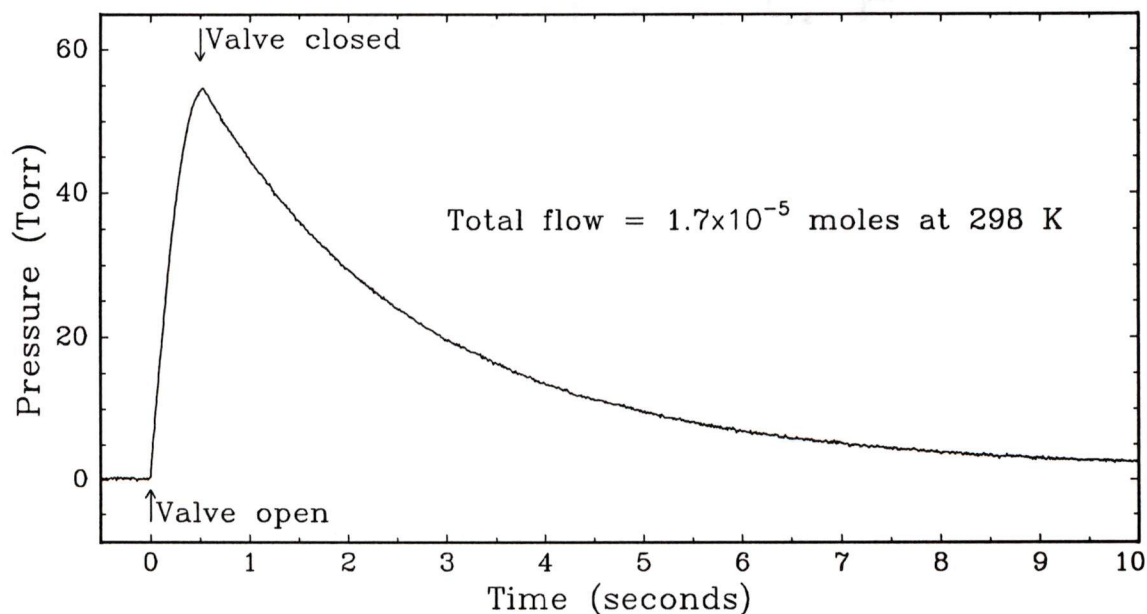


**Figure 2.4:** Pressure build-up inside the nozzle during a typical 500 ms solenoid valve opening time, indicated by the arrows. The pressure in the mixing chamber is initially 60 Torr. Pressure decay is due to gas leaking through the 200  $\mu\text{m}$  diameter opening.

### 2.3.1 Free Jet Expansion

A gas flowing through a nozzle with an imposed pressure difference of  $(P_0 - P_b)$  accelerates toward the nozzle exit. If the nozzle converges toward the nozzle exit, the acceleration is enhanced due to the decreasing area, such that, the gas flow reaches the speed of sound at the exit.  $P_0$  is the source pressure. The pressure in the sample chamber will be referred to as the background pressure  $P_b$ . If the pressure ratio  $P_0/P_b$  exceeds a critical value  $G \equiv ((\gamma + 1)/2)^{\gamma/(\gamma-1)}$  then the mean velocity at the nozzle exit is equal to the local speed of sound.  $\gamma$  is the molar heat capacity ratio  $C_p/C_v$ , a property of the fluid species.

When the gas expands out of the nozzle and into a vacuum the pressure at the nozzle exit is roughly equal to  $P_0/2$ . The flow is underexpanded at this point, so the gas density continues to decrease; the random thermal energy is converted into directed kinetic energy of a supersonic flow field. This correlates to decreasing temperature and pressure. The mean velocity of the flow increases independent of  $P_b$ . This is because the flow is moving faster than information propagates.

The molar heat capacity ratio for  $C_2H_2$  is 1.241, thus  $G$  is 1.8. A background pressure of  $10^{-1}$  is typical in the present setup. With a source pressure of 60 Torr the pressure ratio,  $P_0/P_b \approx 600$ . A supersonic, or free jet, expansion is therefore taking place since  $P_0/P_b \gg G$ . This fact can be used to characterize the properties of temperature and pressure in the flow field for the present experimental setup.  $T$  and  $P$  may be determined from the distance dependent Mach number ( $M$ ). For an ideal

gas, the speed of sound is  $a = \sqrt{\gamma RT/W}$  and  $M \equiv V/a$ .  $V$  is velocity. Approximate values of  $T$  and  $P$  can be computed from the following equations.

$$(T/T_0) = \left(1 + \frac{\gamma - 1}{2} M^2\right)^{-1} \quad (2.1)$$

$$(P/P_0) = \left(1 + \frac{\gamma - 1}{2} M^2\right)^{-\gamma/(\gamma-1)} \quad (2.2)$$

$C_p$  and  $\gamma$  are assumed to be constant for the entire range of temperatures. As well, ideal gas behaviour, and continuum flow are assumed.

The variation of  $M$  with distance may be calculated using Equation 2.3. Note that it is independent of source and background conditions and molecular weight. The coefficients and equations were given by Murphy [6] (see also Scoles [7]). The fits are for circular nozzles and assume that the entropy is constant (isentropic) throughout the flow.  $x/d$  is the ratio distance to nozzle throat diameters.

| Source   | $\gamma$ | $C_1$ | $C_2$   | $C_3$  | $C_4$   | A     | B      |
|----------|----------|-------|---------|--------|---------|-------|--------|
| Circular | 5/3      | 3.232 | -0.7563 | 0.3937 | -0.0729 | 3.337 | -1.541 |
| Circular | 7/5      | 3.606 | -1.742  | 0.9226 | -0.2069 | 3.192 | -1.610 |
| Circular | 9/7      | 3.971 | -2.327  | 1.326  | -0.311  | 3.609 | -1.950 |

$$0 < \frac{x}{d} < 0.5 : \quad M = 1.0 + A \left(\frac{x}{d}\right)^2 + B \left(\frac{x}{d}\right)^3$$

$$\frac{x}{d} > 0.5 : \quad M = \left(\frac{x}{d}\right)^{(\gamma-1)} \left[ C_1 + \frac{C_2}{\left(\frac{x}{d}\right)} + \frac{C_3}{\left(\frac{x}{d}\right)^2} + \frac{C_4}{\left(\frac{x}{d}\right)^3} \right] \quad (2.3)$$

The Mach number, temperature and pressure of the flow field are shown in Figure 2.5 as a function of distance in nozzle throat diameters. A value of  $\gamma = 9/7$  was used for these approximations since  $\gamma = 1.241, 1.304, 1.275$  for  $C_2H_2, CO_2$  and  $N_2O$ , respectively. The cooled window is 150 nozzle throat diameters from the nozzle exit. The flow field will continue along the path shown in Figure 2.5 as long as no other processes occur. Processes such as cluster formation and Mach shock will be discussed in Chapter 5. Other processes such as collisions with thermalized species returning from the walls shield and window are too complex to model. It is safe to assume, however, that a good deal of cooling occurs during the initial expansion such that the internal temperature prior to collision with the window may be at or even below the window temperature.

### 2.3.2 Cooled Equilibrium Cell

In an attempt to condense bulk binary phase  $CO_2-C_2H_2$  under thermodynamic equilibrium conditions, a solution cell capable of withstanding high pressures and low temperatures was constructed. It was hoped that binary gas mixtures of  $CO_2$  and  $C_2H_2$  could be condensed in the cell to yield in bulk the same binary crystalline phase seen by Gough and Wang [1]. The cell, pictured in Figure 2.6, is similar in design to the cooled window. Each ZnSe window is fixed to brass flanges by compressing indium wire between two flanges and the window. The two window assemblies are bolted together and sealed with indium. This configuration allows the path length

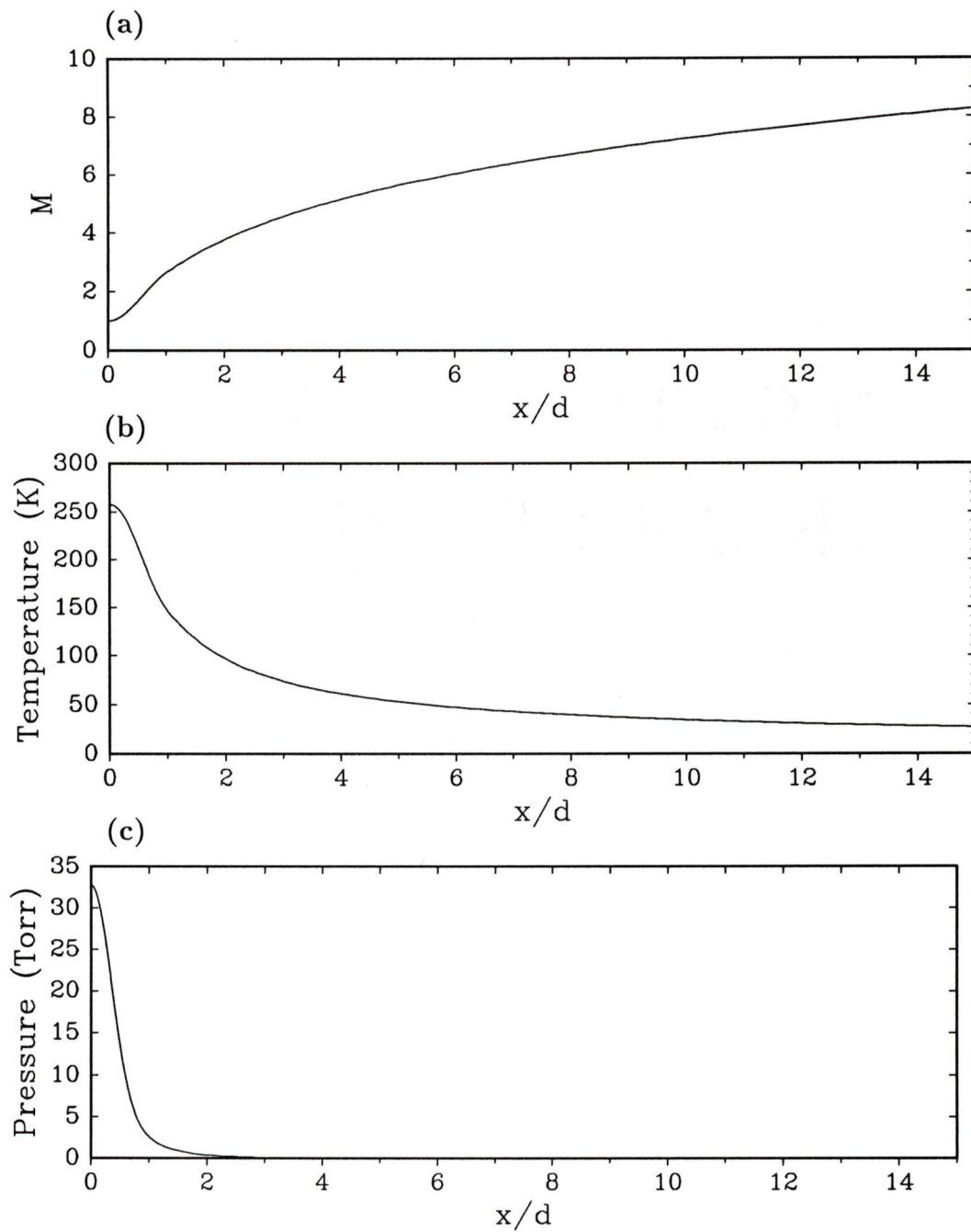


**Figure 2.5:** Free jet centerline  $M$ ,  $T$  and  $P$  versus distance in source diameters. Free jet temperature and pressure are calculated from Equations 2.1 and 2.2 using  $M$  and  $\gamma = 9/7$ . The  $M$  values are calculated from Equation 2.3.

between the two windows to be varied. By tightening the bolts, the path length was reduced to as thin as several hundred microns. Because of the minute size of the inlet and the low temperature, clogging is a potential problem. This was overcome by filling the evacuated cell to roughly two atmospheres with the sample gas. The cell was cooled slowly until droplets appeared on the window. At this point the temperature of the cell was held constant as it was filled by keeping the gas supply pressure several hundred Torr higher than the vapour pressure of the liquid. Once the cell was sufficiently filled, the gas supply was shut off. Slow cooling was then resumed. The temperature of the cell was controlled with cooled dry nitrogen gas. The flow rate of the  $N_2$  gas (controlled by a needle valve) determined the temperature of the cell.

The construction of the cell allowed simultaneous vapour pressure and FTIR spectral data to be taken at various temperatures ranging from room temperature to 85 K. The cell was able to withstand high pressures as well as rapid cooling.

## 2.4 Interferometric Spectrometer

The primary instrument employed in this work is the BOMEM (FTIR) spectrometer. The essential elements are shown in Fig 2.7. The heart of the BOMEM spectrometer is a Michelson-type interferometer. A general discussion of interferometry may be found in the literature [9–12] as well as more detailed mathematical treatments [13, 14]. A description of the more relevant aspects of the spectrometer and the general principles

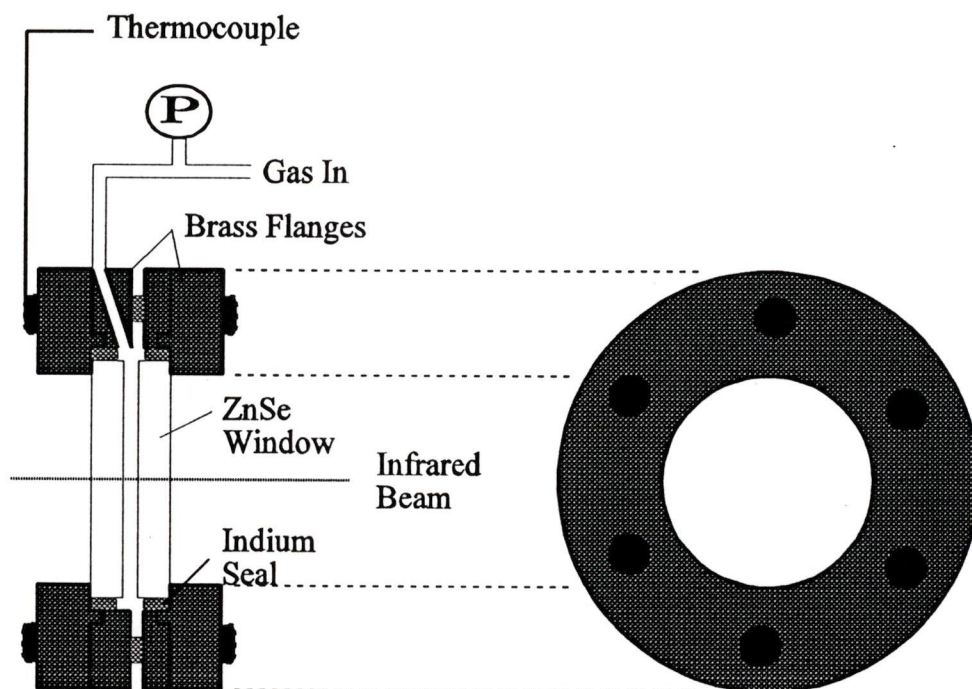


**Figure 2.6:** Liquid nitrogen cooled solution cell made with brass flanges and zinc selenide windows, sealed with indium wire.

of interferometry will be dealt with here.

Broad spectrum radiation (mid-infrared) from the source (globar) passes through a variable diameter aperture. The aperture diameter must be large enough to obtain high throughput efficiency from the source yet not so large that the resolution is affected. The radiation is collimated by mirror C before impinging on a potassium bromide beam splitter. Ideally, half of the radiation is reflected towards mirror  $M_1$  while the other half is transmitted toward mirror  $M_2$ . The two mirrors are situated perpendicular to one another; one is fixed while the other is movable. When the two mirrors are equal distance from the beam splitter the reflected beams recombine in phase, having travelled the same distance. The intensity recorded with the detector at this point,  $I(0)$ , is at its maximum value. As  $M_1$  is displaced the two recombined beams interfere with one another. The interference patterns for each wavelength of light are superimposed on one another, and the intensity is modulated in accordance with this displacement and with the frequency content of the incident radiation. Thus, an interferogram may be recorded in terms of intensity as a function of optical path difference. The function plotted,  $I(x)$ , is of the form:

$$I(x) - \frac{1}{2}I(0) = \int_0^{\infty} B(\sigma) \cos(2\pi\sigma x) d\sigma \quad (2.4)$$

Optical path difference,  $x$ , is twice the distance travelled by the movable mirror,  $I(x)$  is the radiation intensity recorded at the source, and  $\sigma$  is the wavenumber ( $\sigma = \nu/c$ ) given in  $\text{cm}^{-1}$ . Figure 2.8 shows a typical interferogram recorded with the BOMEM

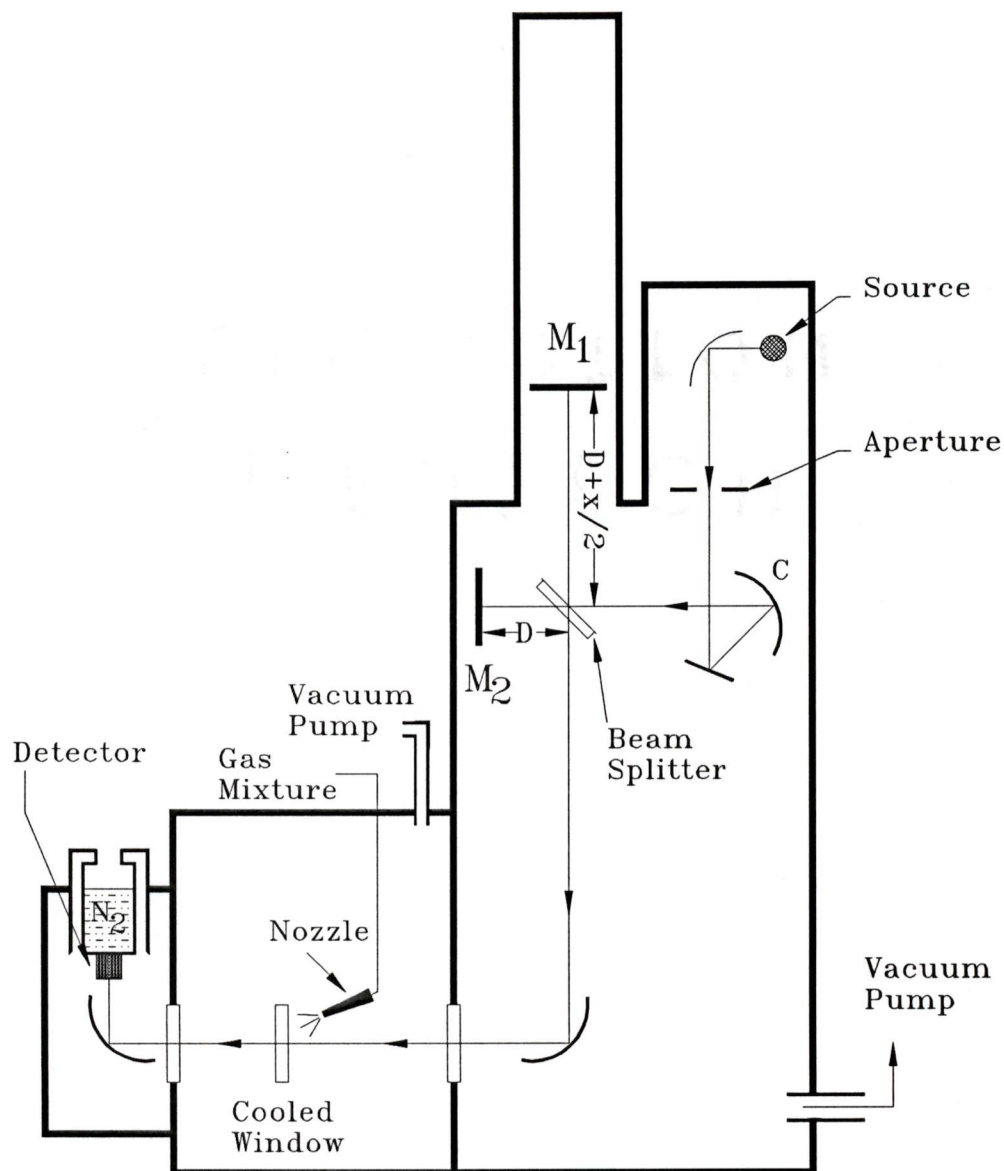


**Figure 2.7:** A schematic diagram showing the essential elements of the BOMEM DA3.002 FTIR spectrometer. Collimated radiation from the temperature stabilized globar is split into two equal intensity beams by the KBr beam splitter.  $M_1$  is the moving mirror and  $M_2$  is stationary. The recombined beam exiting the interferometer is channeled through the sample chamber and focused onto a liquid nitrogen cooled MCT detector.

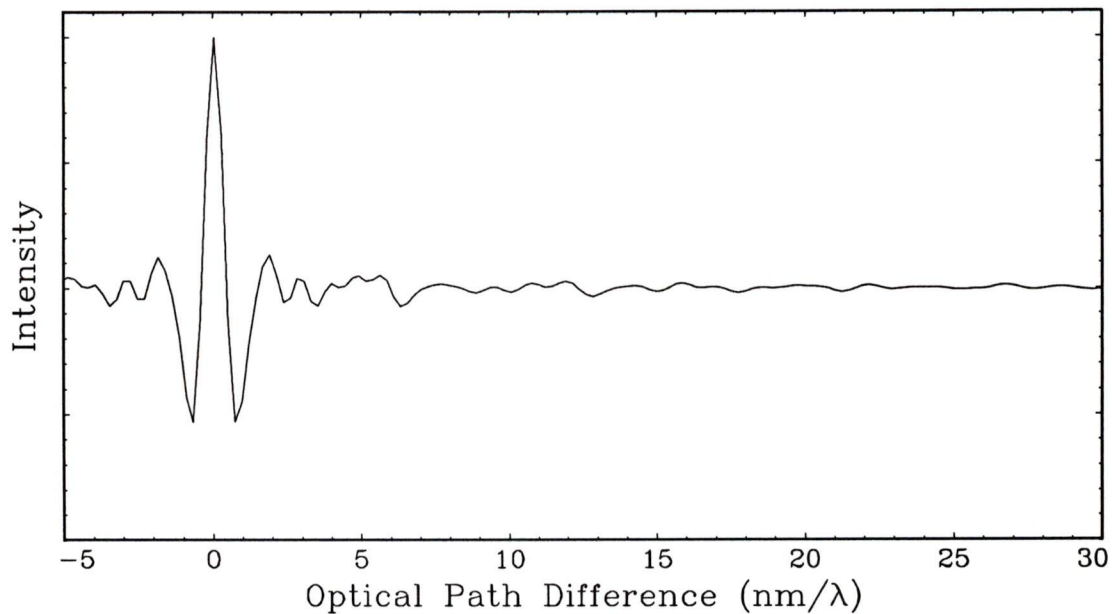


**Figure 2.8:** A typical interferogram. Each distance unit represents one wavelength of radiation from the HeNe laser,  $\lambda=632.8$  nm.

in the absence of a sample.

By Fourier analysis, the interferogram is converted into a spectrum. Since an optical path difference of infinity is impossible, the Fourier transform integral,

$$B(\sigma) = \int_0^{\infty} \left[ I(x) - \frac{1}{2}I(0) \right] \cos(2\pi\sigma x) dx, \quad (2.5)$$

is approximated by summation with the maximum displacement of the movable mirror ( $L$ ) determining the upper limit. Because of this approximation, the maximum resolution attainable is roughly equal to  $1/L$   $\text{cm}^{-1}$ .

Instrumental resolution also depends upon the area of the aperture. Ideally, the

radiation beam should be collimated. In reality, since the global source is not a point source, the beam shape is not a cylinder but a cone. As a result, light rays hit the moving mirror at angles other than  $90^\circ$ . This is known as angular divergence. The optical path difference,  $x_i$ , for each light ray is dependent upon the angle between its direction of propagation and the optical axis:

$$x = 2L \cos \theta \quad (2.6)$$

where  $L$  = the total displacement of the moving mirror and  $\theta$  = the angle between the direction of propagation and the optical axis.

The differences in  $x$  cause destructive interference, reducing the intensity of light returning to the beam splitter. This effect increases as the mirror moves farther away from the beam splitter. As  $L$  approaches  $1/\sigma\theta_m^2$  the interferogram amplitude approach 0. Thus, resolution is limited by  $\sigma\theta_m^2$  (ie.  $1/L$ ).  $\sigma$  is the wavenumber of the radiation.  $\sigma\theta_m^2$  is the maximum angle of divergence and is directly proportional to the area of the aperture. Note that reduction in aperture size which allows higher resolution also reduces the throughput of light yielding a worse signal-to-noise ratio.

Normally, a sufficiently small aperture is chosen such the aperture has no consequence on the resolution. Thus, the maximum displacement chosen for  $M_1$  determines the resolution of the instrument. The BOMEM FTIR spectrometer is capable of an optical path difference of 250.0 cm which relates to a maximum resolution of 0.002  $\text{cm}^{-1}$ . In order to reduce scanning time and noise, a resolution of 0.500  $\text{cm}^{-1}$  was

typically used in the course of this work. This low resolution is justified by the fact that most peaks observed had a full width at half the maximum height (FWHM) larger than  $1.0 \text{ cm}^{-1}$ .

In order to co-add successive scans and obtain the spectrum via a Fourier transformation, it is necessary to have a unique reference point that is reliable and highly repetitive from scan to scan. It is preferable that this point is at a zero path difference ( $x=0$ ). Since broadband radiation produces an easily recognizable pattern at  $x=0$  (see Figure 2.8), white light produced from an intense incandescent lamp is passed through the same optical path such that it runs parallel with the radiation from the source. After passing through the interferometer, the recombined white light beam is collected onto a photodiode detector. From the white light interferogram, the zero path difference (zpd) is determined for each mirror scan. This point is then used to initialize each successive scan.

A second additional beam of radiation is also passed through the same optical path. It is a highly monochromatic (with a wavelength of 632.8 nm), frequency stabilized, helium-neon (HeNe) laser beam. The purpose of the HeNe laser beam is to accurately identify the mirror displacement from the zero path difference by simply counting the fringes produced from the HeNe laser passing through the interferometer. The interference pattern resulting from monochromatic radiation passing through a Michelson interferometer is sinusoidal with a maximum intensity occurring for each moving mirror displacement of  $l = l_0 \pm (n \times \lambda/2)$  for  $n=0, 1, 2, 3, \dots$ .  $\lambda$  is the wavelength

of the monochromatic radiation. In other words, the two beams reflected off  $M_1$  and  $M_2$  constructively interfere whenever the optical path difference is an integral number of wavelengths. This is referred to as a laser fringe reference system. It provides very precise mirror position determination independent of mirror velocity and regularly spaced sampling intervals. The minima as well as the maxima from the laser interferogram are used as the sampling intervals. An intensity measurement is thus recorded at each mirror displacement of  $\lambda/4$  to yield a highly accurate interferogram.

The efficiency of the interferometer depends upon the planarity and stability of the mirror and mirror drive system. In the BOMEM, the two mirrors are kept perpendicular to one another during the complete translation of  $M_1$  by dynamic alignment of  $M_2$ . The design of the mirror drive system with a torque motor and tensioned belt drive allows for a very smooth translation of the moving mirror at constant velocity.

As mentioned a temperature stabilized infrared radiating globar (200 to 10000  $\text{cm}^{-1}$  frequency range) is used as the source in the present experiments. Unwanted frequencies may be filtered out with a shallow cut-off filter situated prior to the aperture.

The beam splitter is a polished single crystal of potassium bromide (KBr) coated with several dielectric layers in order to transmit 50% of the light. The crystal has a frequency range of 450 to 9000  $\text{cm}^{-1}$ . Since KBr is sensitive to water and because atmospheric water vapour and carbon dioxide exhibit very strong (and thus bothersome) infrared absorptions, the entire spectrometer is continuously evacuated.

One other option is to purge the system with dry nitrogen gas, but this is not as effective in removing water and carbon dioxide as evacuation. Purging is also more costly and less easily controlled.

A liquid nitrogen cooled mercury-cadmium-tellurium (MCT) detector was used to collect all spectra in this work. It is a photo-voltaic detector with a spectral range 400 to 5000  $\text{cm}^{-1}$  and a fast-response, which allows the movable mirror to scan at a velocity of 0.50  $\text{cm sec}^{-1}$ .

### 2.4.1 Advantages of FTIR Spectrometers over Dispersive Instruments

An interferogram, a plot of infrared detector response versus optical path difference, contains all of the spectral elements. A consequence of this is the Fellgett or multiplex advantage over conventional dispersion spectrometers. If there are  $N$  spectral elements, each spectral element is studied simultaneously for a total time  $T$  which is required to record the interferogram. By contrast, a conventional instrument requires a total time of  $T \times N$  to record a spectrum with a similar signal-to-noise ratio. For equal total times of observation, the signal-to-noise ratio of an interferometric spectrometer will be greater by a factor of  $\sqrt{N}$ .

The resolution of an FTIR spectrometer is enhanced by increasing the displacement of the movable mirror. The slit width in a dispersive spectrometer must be

decreased, thereby reducing the energy throughput and greatly decreasing the signal-to-noise ratio from the detector. In addition to high resolution from short scan times, an FTIR spectrometer gives highly accurate and reproducible frequency determinations. This leads to the feasibility of signal averaging which increases the signal-to-noise ratio.

It is because of these strengths that the BOMEM FTIR spectrometer is ideal in the present study. Moderately high resolution spectra with a high signal-to-noise ratio are necessary since the bands of interest are weak and narrow. Speed in obtaining these spectra is also essential in case the product is metastable.

## Chapter 3

# The Carbon Dioxide - Acetylene

## Binary Phase

### 3.1 Introduction

Recently, spectroscopic evidence was presented for the existence of a novel binary crystalline solid consisting of carbon dioxide and acetylene held together by van der Waals forces [1]. These binary complexes were formed as microcrystallites suspended in a modified version of what Gough *et al.* [8,15] refer to as the diffusive trapping cell. Briefly, they were prepared by the following approach. The gases were mixed together and diluted in a non-condensable carrier gas (helium). The mixture was introduced into a cooling tube in which a temperature gradient was maintained; from

room temperature at the inlet to 90 K at the outlet. As the gas passed through the tube the mixture cooled until it eventually condensed. The result was submicron microcrystallites suspended in helium. The microcrystallites passed from the cooling tube into a spectroscopic cell to be studied with a FTIR spectrometer.

Depending on the concentration of the mixture in the flow, the spectra contained features which were characteristic of either pure carbon dioxide, pure acetylene, or a new mixed phase. Mixtures rich in  $\text{CO}_2$ , for instance, yielded pure  $\text{CO}_2$  and pure  $\text{C}_2\text{H}_2$  microcrystallites. The same phenomenon was observed for mixtures rich in  $\text{C}_2\text{H}_2$ . It may be concluded that each chromophore condenses separately at a different stage in the cooling tube. For a certain range of mixtures between these two extremes, however, frequency shifts were observed from each of the pure absorption bands. This shift in position was determined to be due to the presence of a new mixed phase containing carbon dioxide and acetylene in a specific stoichiometric ratio. In this range of mixtures, the partial pressures are such that the condensation temperatures of the two gases are similar. Thus, they are able to co-condense at the same stage of the cooling tube. This equilibrium approach did not provide a complete understanding of the mechanism of complex growth. It does not explain why in a mixture rich in  $\text{CO}_2$ , the  $\text{C}_2\text{H}_2$  does not exist in the binary phase, so nonequilibrium effects, such as the dynamics of the nucleation and growth of crystalline solids, were considered. This led to a model of the nucleation and growth of the binary phase in the particular environment.

The concentration of the mixture entering the spectroscopic cell was not guaranteed to be the same as the mixture entering the cooling tube. Because the vapour pressures of carbon dioxide and acetylene are different, differing amounts will condense on the walls of the cooling tube on their way to the cell. Therefore, the stoichiometry of the new phase could not be determined by systematic variation of the concentrations entering the apparatus. A less definitive approach was used to determine the stoichiometry. The relative intensities of absorptions characteristic of each component in the mixed phase were compared with the absolute intensity ratio in the gas phase. A stoichiometry of  $\text{CO}_2 \cdot (\text{C}_2\text{H}_2)_2$  was thus determined. However, this required that the absolute intensities of the absorptions do not change upon going from the gas phase to the mixed solid phase.

The present work was undertaken in an attempt to confirm the stoichiometry of the binary phase without any assumptions concerning the absolute intensities of infrared absorption. Initially, the intention was to prepare the carbon dioxide-acetylene complex in bulk under equilibrium conditions. It was not possible to prepare the binary solid by freezing a mixed solution of  $\text{CO}_2$  and  $\text{C}_2\text{H}_2$ . A successful method was later developed which deposits the binary solid onto a cold window. The results of these new methods are outlined in this chapter.

## 3.2 Experimental Conditions and Results

### 3.2.1 Equilibrium Studies

In an attempt to construct a phase diagram of carbon dioxide - acetylene system, various gas mixtures of acetylene with carbon dioxide were introduced into an evacuated steel container and cooled slowly until the mixture condensed. The vapour pressure of the liquid was then monitored as the liquid was further cooled through the freezing point and subsequently re-cooled. Hysteresis showed that the cooling was sufficiently slow to allow equilibrium to be established. The melting point of acetylene was found to depress as much as 25 K for mixtures containing large amounts of carbon dioxide. However, the measured vapour pressure of the solid was equal to the combined equilibrium vapour pressures of the pure components within experimental error. This suggested that the binary phase was not present.

In order to determine conclusively whether or not the binary phase was present, a cooled equilibrium solution cell was fabricated. The cell is shown in Figure 2.6. Various liquid mixtures of carbon dioxide and acetylene were prepared in the cell. Spectra of these mixtures were taken at various temperatures as the cell was cooled past the freezing point. Figure 3.1(a) shows the  $\nu_1 + \nu_3$  combination absorption band of  $\text{CO}_2$  for an equimolar sample of carbon dioxide and acetylene. The film is  $0.5 \mu\text{m}$  thick. Spectrum labelled 'i' represents the liquid and spectrum labelled 'ii' represents the solid. The environment in the liquid is clearly different than in the solid. The

position of the liquid band at  $3699.5\text{ cm}^{-1}$  shows that the environment of the carbon dioxide is similar to that of the binary solid phase (see Table 3.2). Freezing, however, leads to phase separation rather than complex formation. The position of the solid band at  $3707.2\text{ cm}^{-1}$  verifies that  $\text{CO}_2$  is in the pure solid environment.

From the results of Gough and Wang [1], the appearance of a peak at  $1963\text{ cm}^{-1}$ , in the region of the infrared inactive  $\nu_2$  symmetric C-C stretching mode of  $\text{C}_2\text{H}_2$ , is indicative of the presence of a binary phase. This vibration was observed presumably because of a lowering of site symmetry. As shown in Figure 3.1(b), a peak is present in this region of the liquid spectrum and absent in the solid, confirming the above conclusion that the binary complex is not formed by an equilibrium process.

Spectra of a thick crystalline sample of acetylene are shown in Figure 3.2. The sample is roughly  $100\text{ }\mu\text{m}$  thick. The  $\nu_2$   $\text{C}_2\text{H}_2$  band is absent, however, combinations between this fundamental and lattice translation modes is observed. One such band is a sum band  $\nu_2 + \nu_T$  located at  $2061\text{ cm}^{-1}$  (spectrum labelled 95 K). The less intense difference band,  $\nu_2 - \nu_T$ , is located at  $1854\text{ cm}^{-1}$  and the center between these two bands is  $1957.5\text{ cm}^{-1}$ . The second lattice mode combination,  $\nu_2 + \nu_{T'}$ , is located at  $2026\text{ cm}^{-1}$ , and  $\nu_2 - \nu_{T'}$  is found at  $1871\text{ cm}^{-1}$ . The center between these two bands is  $1958.5\text{ cm}^{-1}$ . The average of these two center values yields an approximate value of  $1958\text{ cm}^{-1}$ . This is in agreement with the Raman value for  $\nu_2$  in liquid acetylene ( $1961\text{ cm}^{-1}$ ) [16].

Acetylene is known to undergo a phase transition at about 133 K [17]. The low

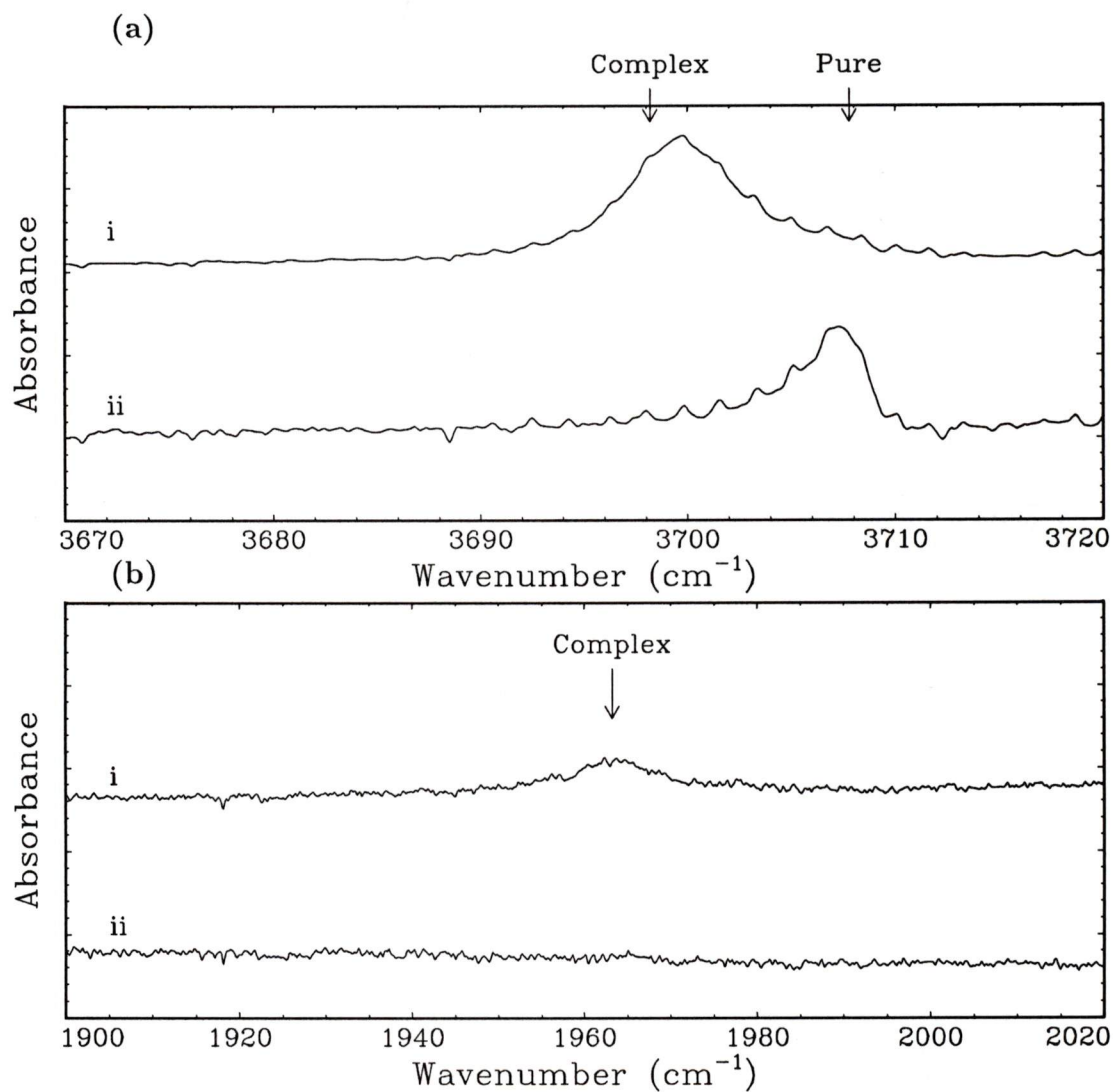


**Figure 3.1:** Spectra of an equimolar  $\text{CO}_2\text{-C}_2\text{H}_2$  mixture in the equilibrium cell. Liquid spectra i are recorded at 165 K. Solid spectra ii are recorded at 157 K.

(a) The  $\nu_1 + \nu_3$  band of  $\text{CO}_2$ .

(b) The  $\nu_2$  band of  $\text{C}_2\text{H}_2$ .

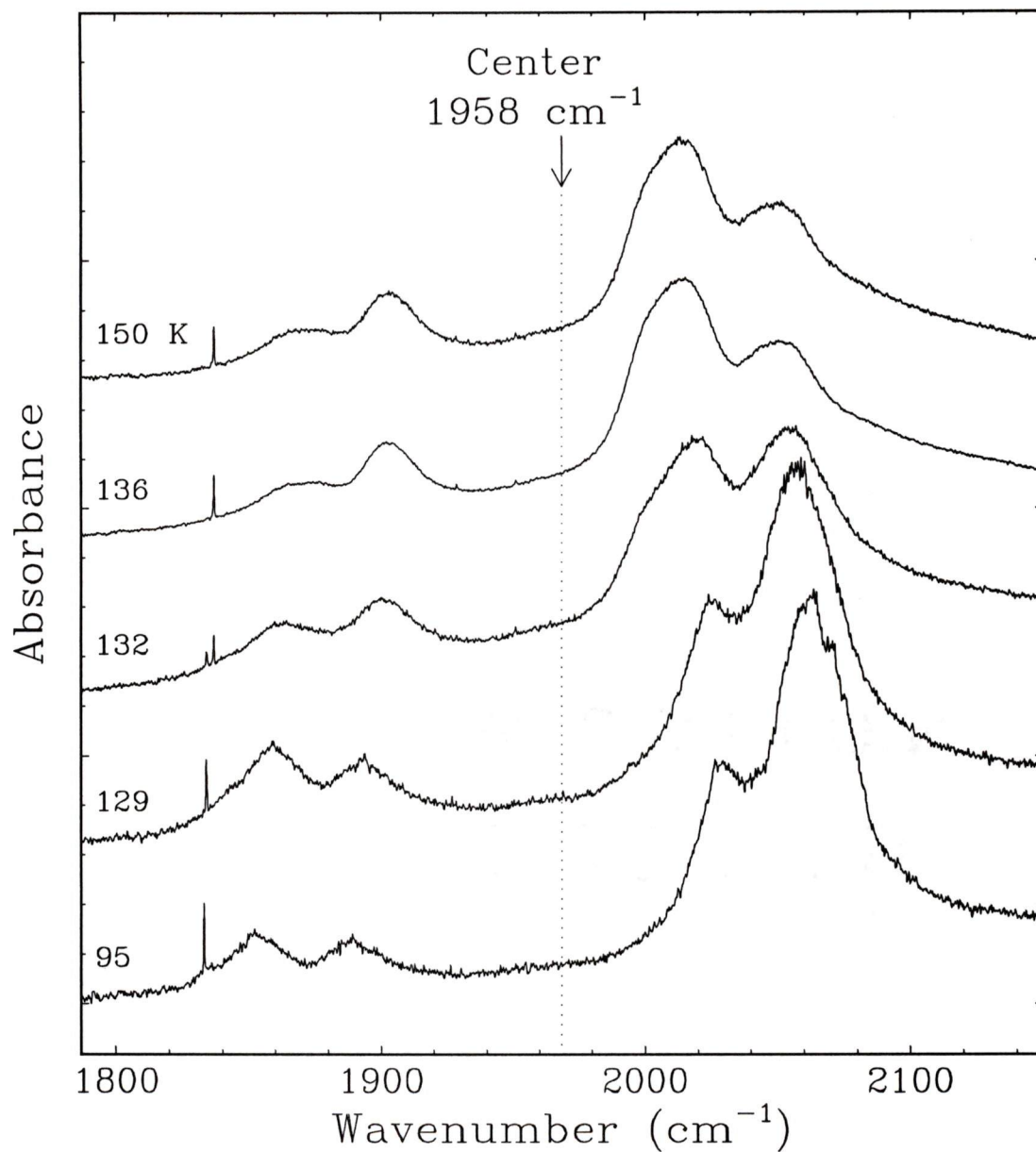


**Figure 3.2:** The combination bands of the  $\nu_2$  symmetric C-C stretch of  $C_2H_2$  with crystal lattice translation modes. The sample is solid acetylene  $100 \mu\text{m}$  thick produced by freezing the pure liquid. The series above shows the gradual warming of the sample over 45 minutes.

temperature phase is believed to be orthorhombic with two molecules per unit cell while the higher temperature phase is face-centered cubic with four molecules per unit cell. Figure 3.2 shows a distinct change occurring at 132 K. The very narrow peak at  $1833\text{ cm}^{-1}$  in the 95 K spectrum is due to the  $\nu_2$  fundamental of  $\text{C}_2\text{HD}$  [17]. This peak abruptly shifts to  $1837\text{ cm}^{-1}$  upon transition to the cubic phase. This phase transition was found to be completely reversible.

### 3.2.2 Non-Equilibrium Studies

The results described above strongly suggest that a binary phase containing  $\text{CO}_2$  and  $\text{C}_2\text{H}_2$  is thermodynamically less stable than the pure phases. Because of this the complex may not be formed under equilibrium conditions, but under kinetically favoured conditions; such as the process of non-equilibrium nucleation. In order to make the binary phase, a method had to be formulated which used non-equilibrium nucleation in a quantitative way in order that the stoichiometry could be determined directly without making any assumptions about absolute absorption intensities.

The experimental apparatus was discussed in Chapter 2 and shown in Figure 2.2. The nozzle and low pressure in the sample chamber provide a free jet expansion (see Section 2.3.1), and thus, the possibility of non-equilibrium nucleation of the binary phase. Subsequent deposition of the product onto a cold window provides the quantitative aspect of the present approach, assuming the concentration in the spray remains the same in the cryofilm after deposition. This assumption is based upon a

high sticking coefficient of both  $\text{CO}_2$  and  $\text{C}_2\text{H}_2$  onto the ZnSe surface and a very low vapour pressure of both solids at 90 K ( $10^{-5}$  and  $10^{-4}$  Torr [5]).

In order to determine the stoichiometry,  $(\text{CO}_2)_m \cdot (\text{C}_2\text{H}_2)_n$ , of the new binary phase, a concentration dependent series of infrared spectra of mixed carbon dioxide - acetylene cryofilms was constructed. The concentration corresponding to the correct proportion of  $\text{CO}_2$  molecules to  $\text{C}_2\text{H}_2$  molecules should yield the largest absorbance of the binary phase and the smallest absorbance due to pure phases. The equilibrium solution approach to this method of stoichiometry determination is known as the method of continuous variation or Job's method [18].

Unless otherwise specified, all cryofilms were condensed onto a ZnSe window cooled to 90 K using a single 500 ms pulse from the mixing board; the temperature was then held constant at 90 K while each FTIR spectrum was recorded at a resolution of  $0.50 \text{ cm}^{-1}$  with 64 co-added scans. The spectral range is 550 to  $4000 \text{ cm}^{-1}$ . Each spectrum was recorded on a separate day to ensure a minimum amount of atmospheric water contamination on the cold window and to ensure the previous gas mixture had been removed from the system.

Table 3.1 gives the experimental conditions used in the preparation of each  $\text{CO}_2$ - $\text{C}_2\text{H}_2$  cryofilm. Each mass flow controller was calibrated in order to convert the applied voltage to a flow rate for the corresponding gas. Concentration, given in mole fraction of carbon dioxide ( $X_{\text{CO}_2}$ ), was varied across the entire range from pure  $\text{CO}_2$  to pure  $\text{C}_2\text{H}_2$ . The mole fraction was calculated from the flow rates

$$X_{\text{CO}_2} = \frac{F_{\text{CO}_2}}{F_{\text{CO}_2} + F_{\text{C}_2\text{H}_2}}. \quad (3.1)$$

Although all observable carbon dioxide and acetylene absorptions show frequency shifts, attention will be focused particularly on the acetylene  $\nu_3$  fundamental (asymmetric stretch) absorption and the carbon dioxide  $\nu_1 + \nu_3$  absorption (combination of the symmetric and asymmetric stretch). These transitions are sufficiently weak that they do not show morphological effects. For instance, spectra of more intense absorptions such as the  $\text{CO}_2$   $\nu_3$  fundamental tend to be more complex. Spurious reflection peaks due to rapid changes in the refractive index occur on the high frequency side of the transition. Also contributing to the complexity is the occurrence of multi-phonon absorptions [19]. The result of these processes is a highly asymmetric band shape and peak positions which vary with film thickness.

In these experiments, the bands in the  $\text{C}_2\text{H}_2$   $\nu_3$  and the  $\text{CO}_2$   $\nu_1 + \nu_3$  regions behave in a consistent and characteristic manner. The newly created binary phase peaks are near Lorentzian in shape and are sufficiently separated from the pure phase peaks; i.e. the  $\text{C}_2\text{H}_2$   $\nu_3$  frequency shift is twenty times larger than the FWHM and the  $\text{CO}_2$   $\nu_1 + \nu_3$  frequency shift is five times larger than the FWHM.

Figures 3.3 to 3.5 show FTIR spectra of the  $\nu_1 + \nu_3$  absorption of carbon dioxide for various  $\text{CO}_2$ - $\text{C}_2\text{H}_2$  mixtures. Figures 3.6 to 3.8 show FTIR spectra of the  $\nu_3$  absorption of acetylene for various  $\text{CO}_2$ - $\text{C}_2\text{H}_2$  mixtures. The spectra are labelled with gas mixture composition given in terms of  $\text{CO}_2$  mole fraction.

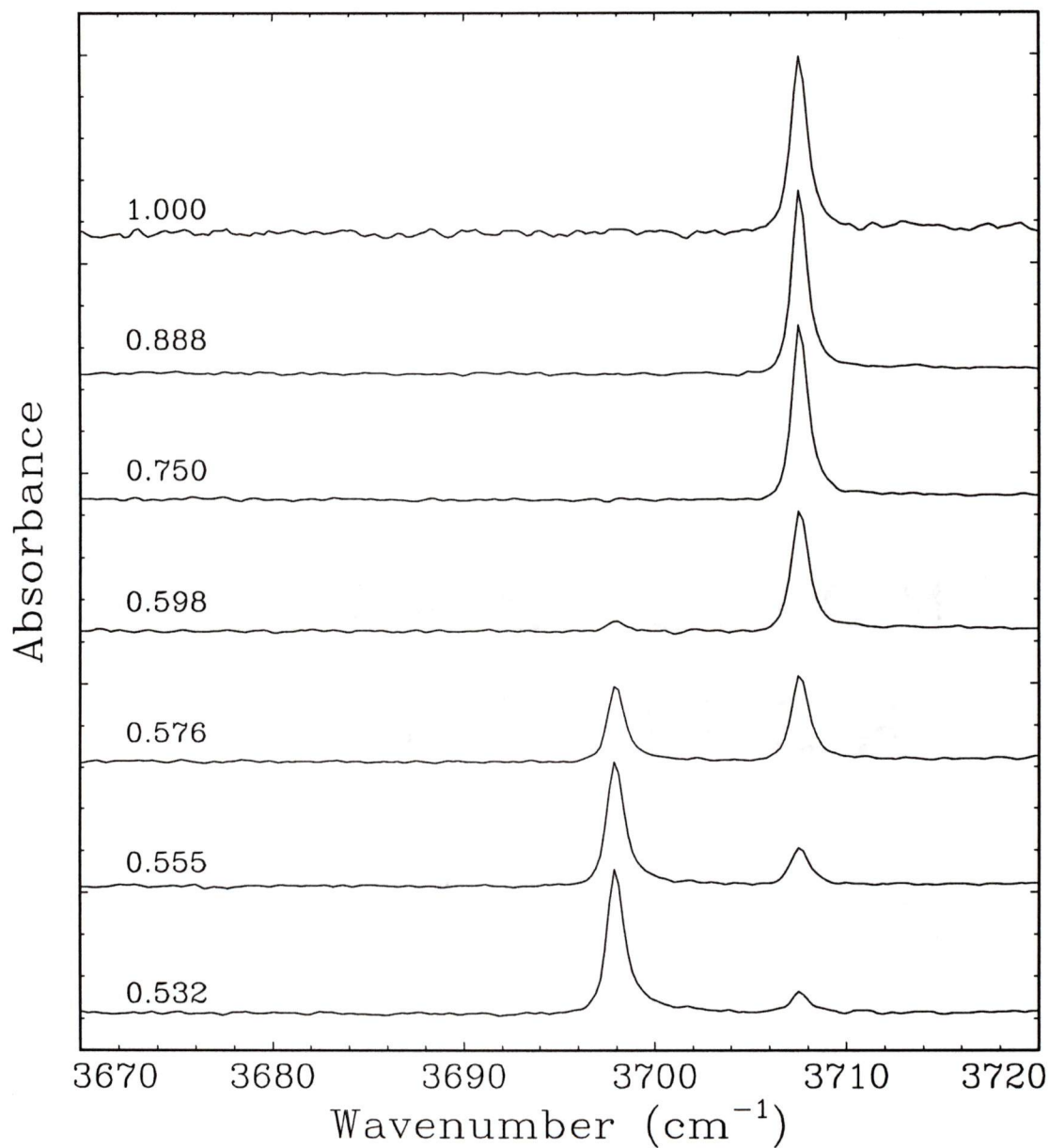


**Figure 3.3:** Spectra of the  $\nu_1 + \nu_3$  combination band of  $\text{CO}_2$  for various  $\text{CO}_2\text{-C}_2\text{H}_2$  mixtures rich in  $\text{CO}_2$ . The spectra are labelled with gaseous mixture composition given in mole fraction of  $\text{CO}_2$ . The experimental conditions for recording these spectra are listed in Table 3.1.

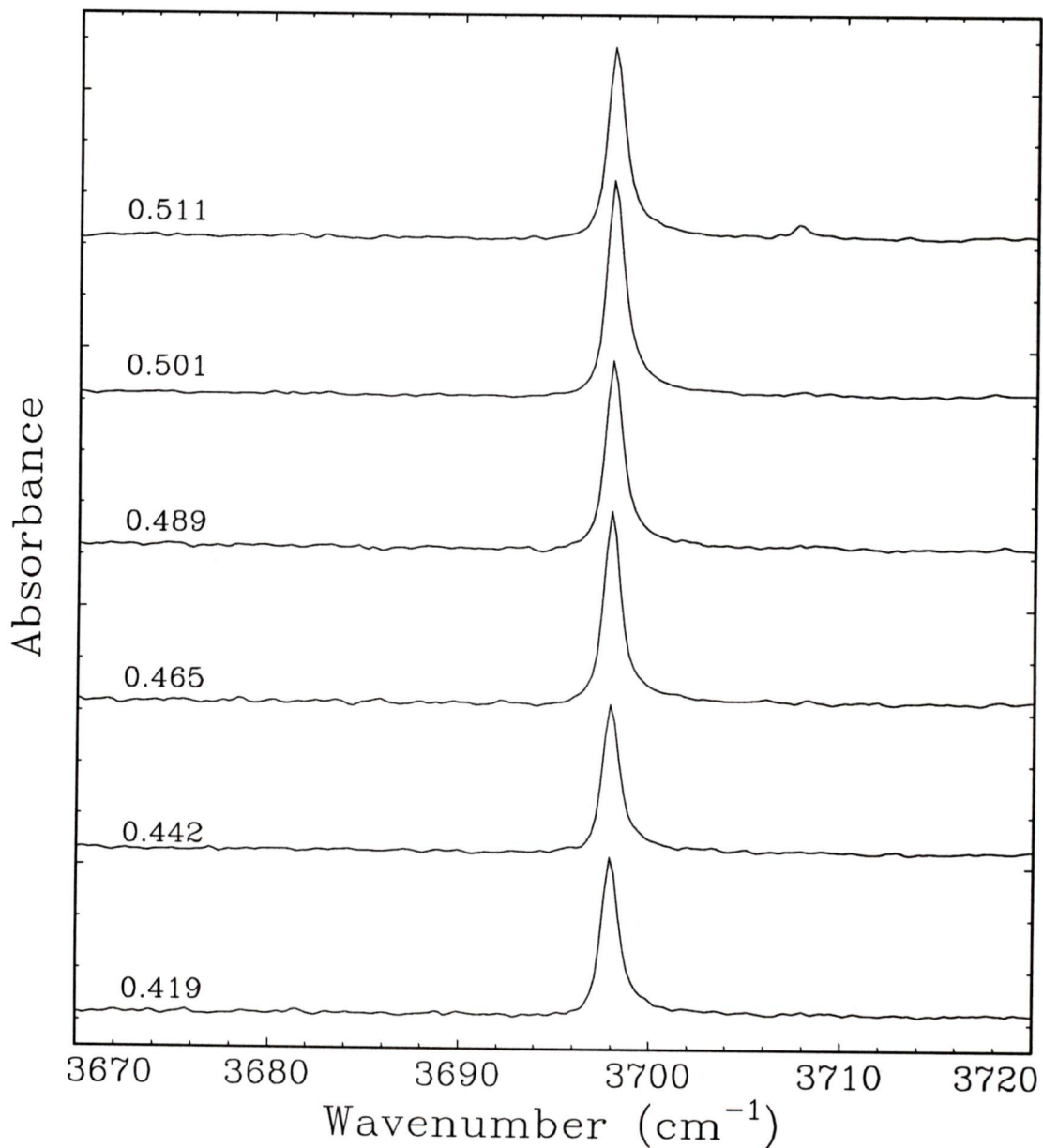


**Figure 3.4:** Spectra of the  $\nu_1 + \nu_3$  combination band of  $\text{CO}_2$  for various  $\text{CO}_2$ - $\text{C}_2\text{H}_2$  mixtures containing roughly equal amounts of  $\text{CO}_2$  and  $\text{C}_2\text{H}_2$ . The spectra are labelled with gaseous mixture composition given in mole fraction of  $\text{CO}_2$ . The experimental conditions for recording these spectra are listed in Table 3.1.

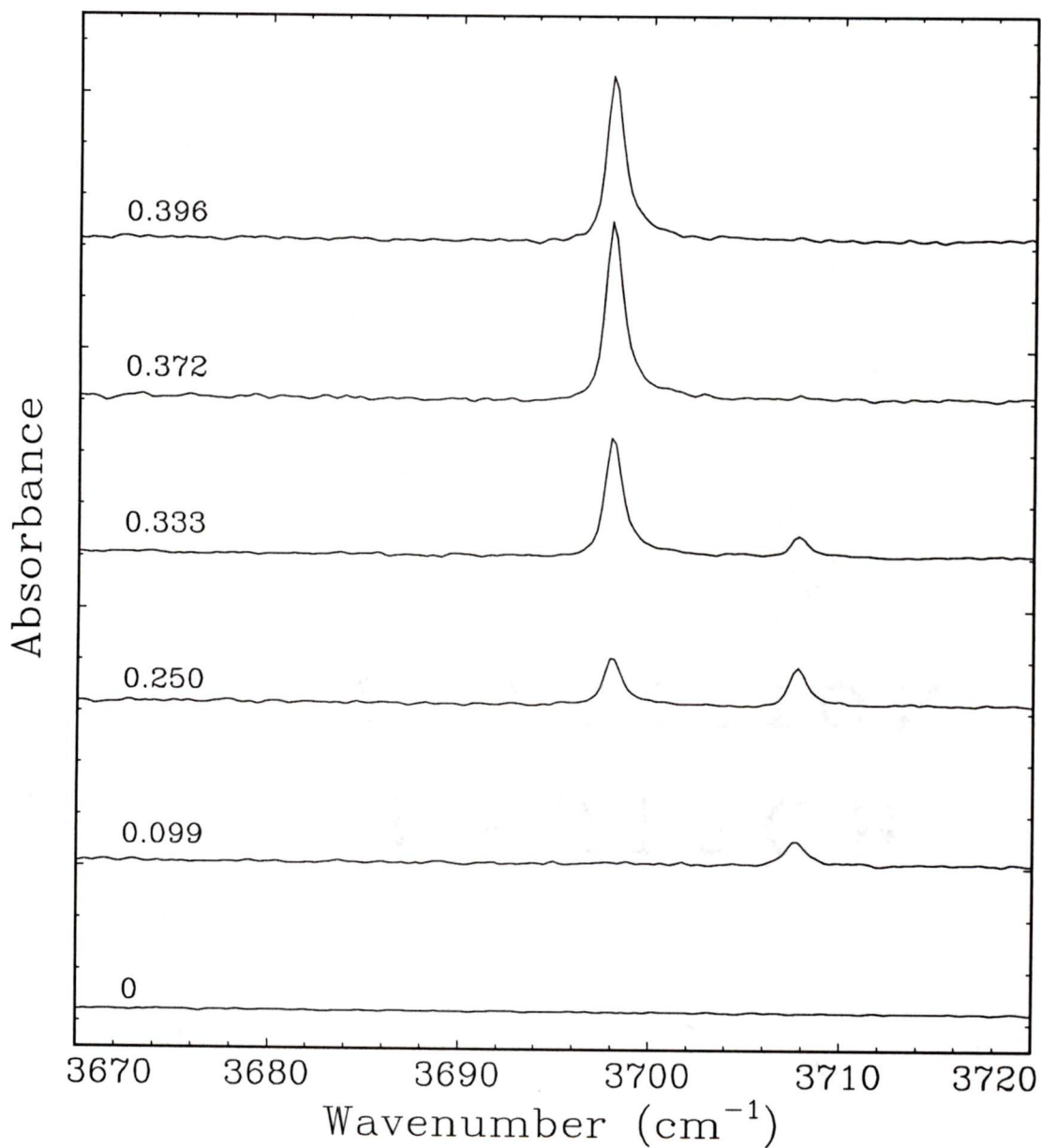


**Figure 3.5:** Spectra of the  $\nu_1 + \nu_3$  combination band of  $\text{CO}_2$  for various  $\text{CO}_2$ - $\text{C}_2\text{H}_2$  mixtures rich in  $\text{C}_2\text{H}_2$ . The spectra are labelled with gaseous mixture composition given in mole fraction of  $\text{CO}_2$ . The experimental conditions for recording these spectra are listed in Table 3.1.

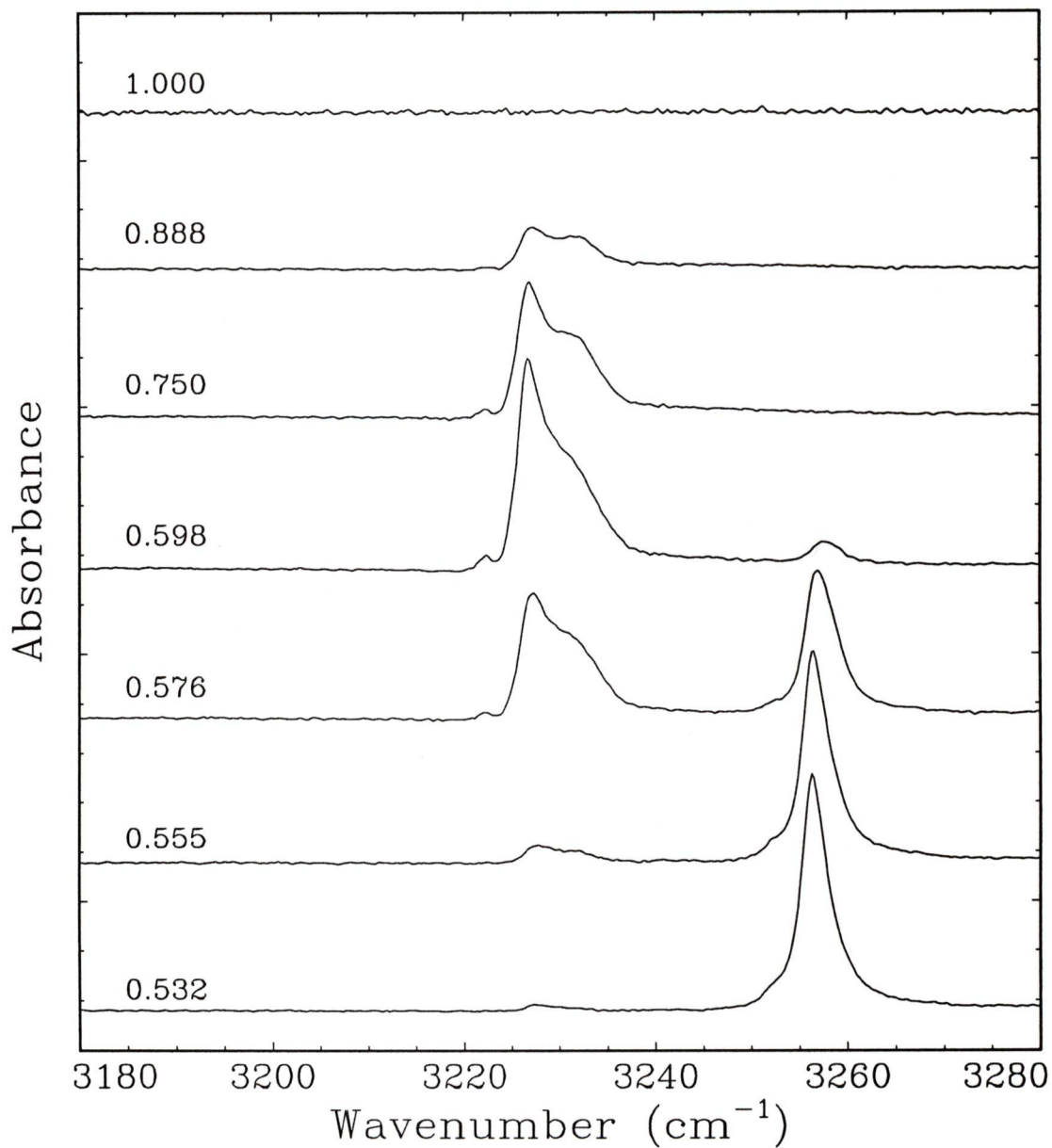


**Figure 3.6:** Spectra of the  $\nu_3$  fundamental band of  $C_2H_2$  for various  $CO_2$ - $C_2H_2$  mixtures rich in  $CO_2$ . The spectra are labelled with gaseous mixture composition given in mole fraction of  $CO_2$ . The experimental conditions for recording these spectra are listed in Table 3.1.

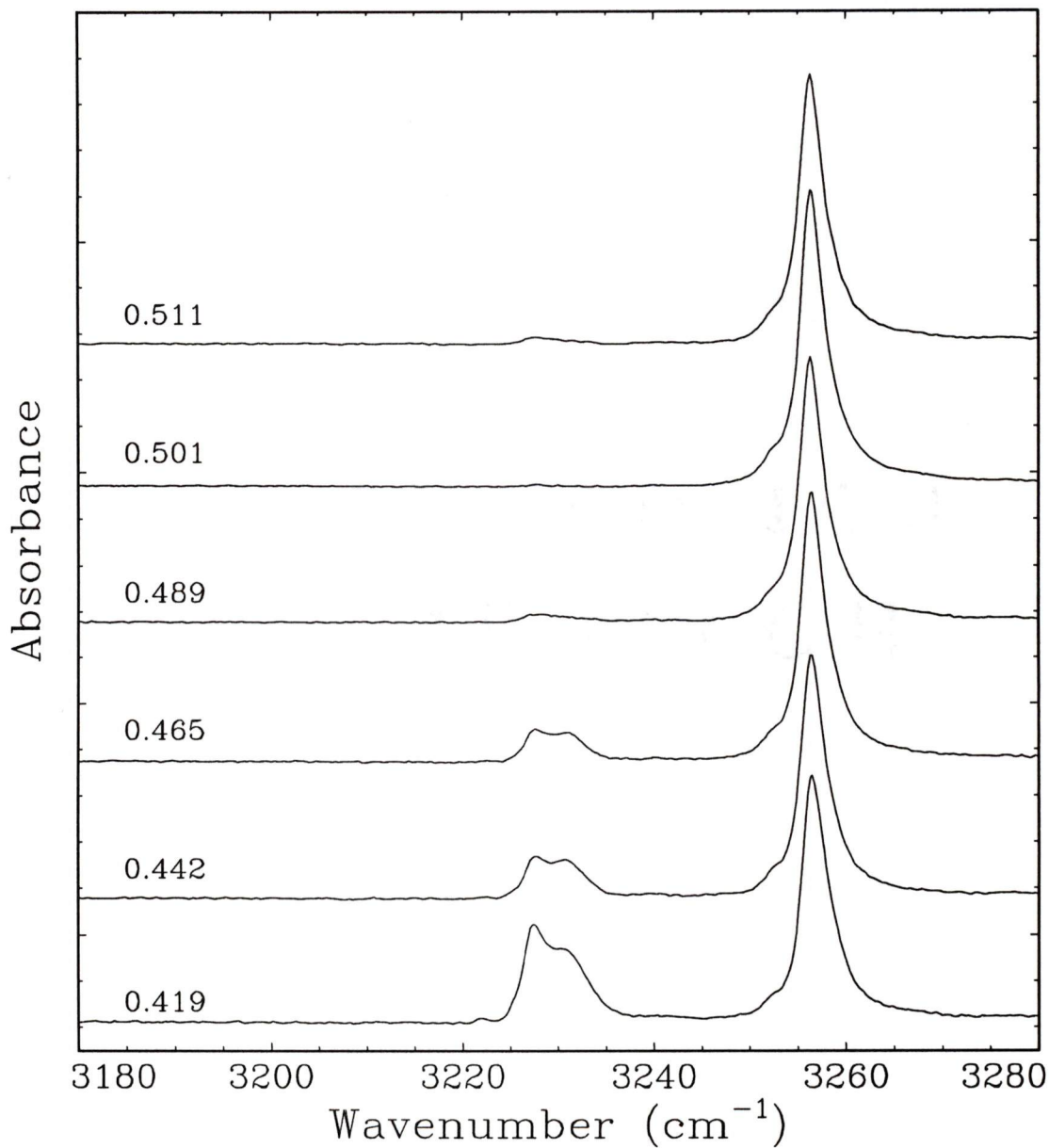


**Figure 3.7:** Spectra of the  $\nu_3$  fundamental band of  $C_2H_2$  for various  $CO_2$ - $C_2H_2$  mixtures containing roughly equal amounts of  $CO_2$  and  $C_2H_2$ . The spectra are labelled with gaseous mixture composition given in mole fraction of  $CO_2$ . The experimental conditions for recording these spectra are listed in Table 3.1.

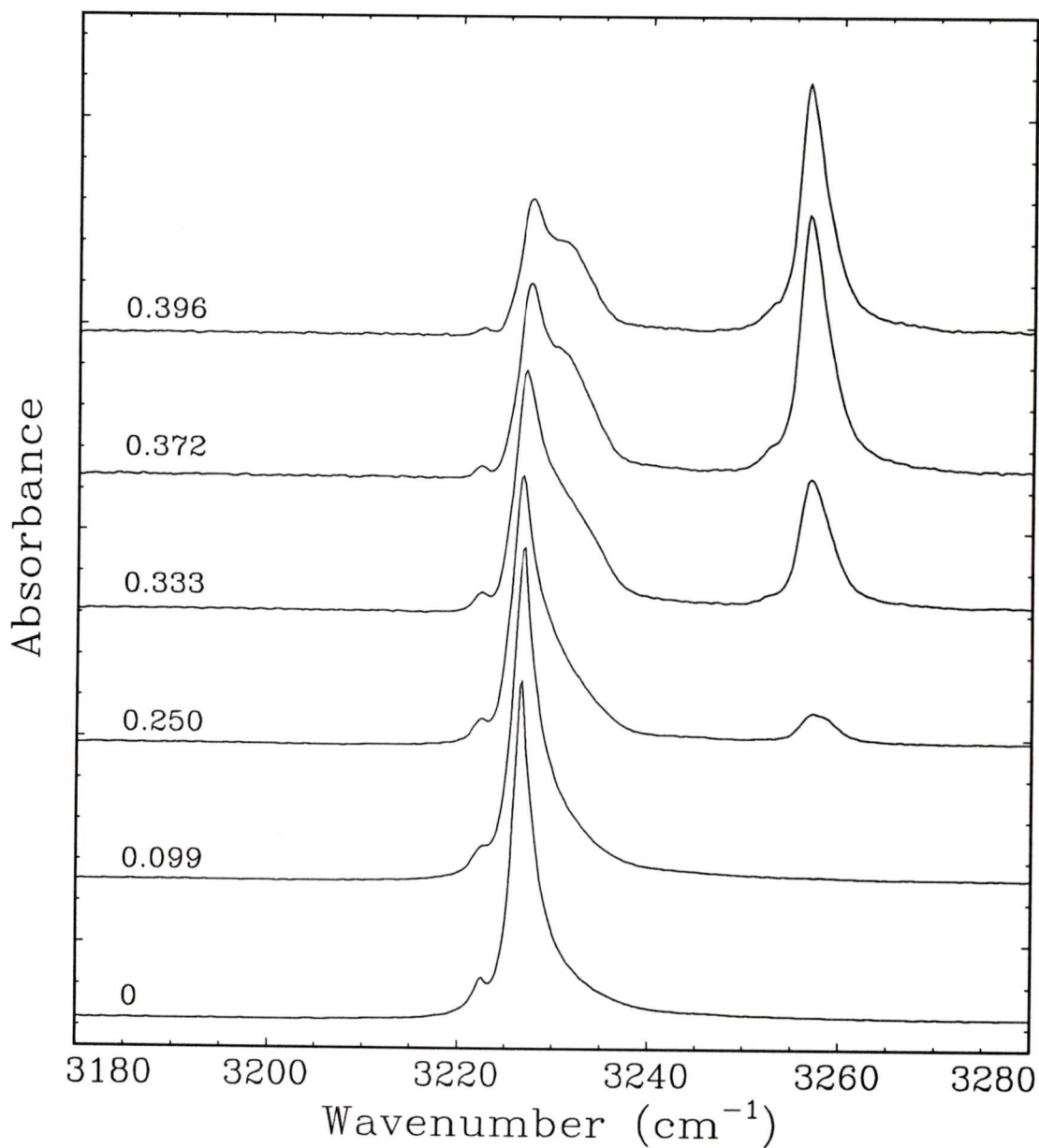


**Figure 3.8:** Spectra of the  $\nu_3$  fundamental band of  $C_2H_2$  for various  $CO_2$ - $C_2H_2$  mixtures rich in  $C_2H_2$ . The spectra are labelled with gaseous mixture composition given in mole fraction of  $CO_2$ . The experimental conditions for recording these spectra are listed in Table 3.1.

| Mole Fraction<br>CO <sub>2</sub> | V <sub>CO<sub>2</sub></sub><br>(mV) | F <sub>CO<sub>2</sub></sub><br>(SCCM) | V <sub>C<sub>2</sub>H<sub>2</sub></sub><br>(mV) | F <sub>C<sub>2</sub>H<sub>2</sub></sub><br>(SCCM) |
|----------------------------------|-------------------------------------|---------------------------------------|---|---|
| 0.0                              | 0.0                                 | 0.0                                   | 3.100   | 5.98  |
| 0.099                            | 0.263                               | 0.655                                 | 3.100   | 5.98  |
| 0.250                            | 0.127                               | 0.366                                 | 0.591   | 1.098   |
| 0.333                            | 0.214                               | 0.549                                 | 0.591   | 1.098   |
| 0.372                            | 0.261                               | 0.651                                 | 0.591   | 1.098   |
| 0.396                            | 0.292                               | 0.718                                 | 0.591   | 1.098   |
| 0.419                            | 0.326                               | 0.792                                 | 0.591   | 1.098   |
| 0.442                            | 0.362                               | 0.871                                 | 0.591   | 1.098   |
| 0.465                            | 0.401                               | 0.956                                 | 0.591   | 1.098   |
| 0.489                            | 0.444                               | 1.049                                 | 0.591   | 1.098   |
| 0.501                            | 0.468                               | 1.101                                 | 0.591   | 1.098   |
| 0.511                            | 0.488                               | 1.145                                 | 0.591   | 1.098   |
| 0.532                            | 0.536                               | 1.249                                 | 0.591   | 1.098   |
| 0.555                            | 0.590                               | 1.367                                 | 0.591   | 1.098   |
| 0.576                            | 0.648                               | 1.493                                 | 0.591   | 1.098   |
| 0.598                            | 0.712                               | 1.632                                 | 0.591   | 1.098   |
| 0.750                            | 1.475                               | 3.292                                 | 0.591   | 1.098   |
| 0.888                            | 4.35                                | 8.67                                  | 0.591   | 1.098   |
| 1.00                             | 4.35                                | 8.67                                  | 0.0   | 0.0   |

Table 3.1: Experimental conditions used for the recording of spectra in the carbon dioxide - acetylene series.  $V_{\text{CO}_2}$  and  $V_{\text{C}_2\text{H}_2}$  are the voltages applied to the corresponding mass flow controllers. Flow rates are given in standard cubic centimetres per minute (SCCM). The pressure in the gas mixing chamber was 60 Torr at the time of deposition. The temperature of the ZnSe window was held constant at 90 K during deposition and recording of spectra. One 500 ms pulse of gas was delivered for each film. Each spectrum was recorded at  $0.50 \text{ cm}^{-1}$  resolution and consists of 64 co-added scans. The spectral range is  $550 \text{ to } 4000 \text{ cm}^{-1}$ .

C<sub>2</sub>H<sub>2</sub> Infrared Frequencies

| Gas                   | Crystal <sup>a</sup><br>at 63 K | Pure Solid <sup>b</sup><br>at 90 K | Binary Phase <sup>b</sup><br>at 90 K | Frequency<br>Shift <sup>c</sup> | Assignment              |
|-----------------------|---------------------------------|------------------------------------|--------------------------------------|---------------------------------|-------------------------|
| 3296.8 <sup>d</sup>   | 3331                            | 3307.5                             | 3314.2                               | 6.7                             | $\nu_2 + \nu_4 + \nu_5$ |
| 3288.6 <sup>d</sup>   | 3226.3                          | 3227                               | 3256.5                               | 29.5                            | $\nu_3$                 |
|                       | 3220.5                          | 3223                               | 3252                                 | 29                              | <sup>13</sup> C $\nu_3$ |
| 2703 <sup>e</sup>     | 2726                            | 2736, 2718                         | 2712, 2704                           | -24, -14                        | $\nu_2 + \nu_5$         |
| 1973.8 <sup>f,k</sup> |                                 | (1958) <sup>g</sup>                | 1963.2                               | 5.3                             | $\nu_2$                 |
| 1327 <sup>h</sup>     | 1422, 1390<br>1377              | 1389.5                             | 1361.2                               | -28.3                           | $\nu_4 + \nu_5$         |
| 729.3 <sup>i</sup>    | 768.8, 760.6<br>747.5           | 768, 760<br>747.4                  | 752, 740.4                           | -12                             | $\nu_5$                 |

CO<sub>2</sub> Infrared Frequencies

| Gas <sup>f</sup> | Crystalline <sup>j</sup><br>at 77 K | Pure Solid <sup>b</sup><br>at 90 K | Binary Phase <sup>b</sup><br>at 90 K | Frequency<br>Shift | Assignment              |
|------------------|-------------------------------------|------------------------------------|--------------------------------------|--------------------|-------------------------|
| 3716             | 3707.8                              | 3707.8                             | 3698.2                               | -9.6               | $\nu_1 + \nu_3$         |
| 3609             | 3599.7                              | 3599.6                             | 3588.5                               | -11.1              | $2\nu_2 + \nu_3$        |
|                  | 2383                                | 2382.5                             |                                      |                    | reflection peak         |
| 2349.3           | 2345.3                              | 2343.6                             | 2337                                 | -6.6               | $\nu_3$                 |
|                  | 2327.1                              | 2327.1                             | 2325.2                               | -1.9               | <sup>18</sup> O $\nu_3$ |
| 2284.5           | 2282.5                              | 2282.5                             | 2277.1                               | -5.4               | <sup>13</sup> C $\nu_3$ |
| 667.3            | 660.3, 655.1                        | 659.7, 654.7                       | 648.9, 657.6                         | -8.3               | $\nu_2$                 |

<sup>a</sup> Reference [17]

<sup>b</sup> Sprayed cryofilm, this work.

<sup>c</sup> Frequency shift is the binary phase value minus the pure solid value.

<sup>d</sup> Reference [20]

<sup>e</sup> Reference [21]

<sup>f</sup> Reference [22]

<sup>g</sup> Calculated from  $\nu_T$  combination modes. See Figure 3.2.

<sup>h</sup> Reference [23]

<sup>i</sup> Reference [24]

<sup>j</sup> Reference [25]

<sup>k</sup> Raman active

Table 3.2: Absorption frequencies (cm<sup>-1</sup>) of C<sub>2</sub>H<sub>2</sub> and CO<sub>2</sub>.

## Results

In Figure 3.3, the spectrum labelled  $X_{\text{CO}_2}=1.000$  shows the  $\nu_1 + \nu_3$  combination band absorption of crystalline carbon dioxide with its peak maximum occurring at  $3707.8 \text{ cm}^{-1}$ . This agrees with the value given by Falk for pure crystalline carbon dioxide  $\nu_1 + \nu_3$  at 77 K [25]. At the higher acetylene concentration of  $X_{\text{CO}_2}=0.598$ , a new peak appears red shifted to  $3698.2 \text{ cm}^{-1}$  indicating a new environment for carbon dioxide. The peak due to pure  $\text{CO}_2$  diminishes as the  $\text{CO}_2$  concentration is decreased. Simultaneously, the peak due to the shifted environment grows until it alone is present at  $X_{\text{CO}_2}=0.501$ . The pure phase peak reappears at  $X_{\text{CO}_2}=0.333$ .

The acetylene series in Figure 3.8 is similar to the carbon dioxide series. The pure acetylene spectrum labelled  $X_{\text{CO}_2}=0$  shows a large, slightly asymmetric, absorption with a peak maximum at  $3227 \text{ cm}^{-1}$  and a much smaller peak at  $3220 \text{ cm}^{-1}$ . These peaks were assigned as crystalline  $\text{C}_2\text{H}_2 \nu_3$  and  $\nu_3(^{13}\text{C})$  by Bottger and Eggers [17]. As carbon dioxide is introduced, a new peak emerges (at  $X_{\text{CO}_2}=0.250$ ) blue shifted to  $3256.5 \text{ cm}^{-1}$  indicating a new environment for acetylene. With increasing  $\text{CO}_2$  mole fraction the new peak continues to grow, as its pure counterpart diminishes, until it alone is present at  $X_{\text{CO}_2}=0.501$ . The pure acetylene reappears in significant amounts at  $X_{\text{CO}_2}=0.576$ .

All other observable  $\text{CO}_2$  and  $\text{C}_2\text{H}_2$  absorptions in the  $550$  to  $4000 \text{ cm}^{-1}$  region show a similar behaviour. Table 3.2 shows the frequency shift for each observable absorption of acetylene and carbon dioxide. One spectroscopic feature of note is

the existence of a weak absorption at  $1963.2 \text{ cm}^{-1}$  in spectra of roughly equimolar mixtures of carbon dioxide and acetylene. This feature is not present in either the pure carbon dioxide or the pure acetylene spectra (see Figure 3.9), but was present in the mixed spectra recorded by Gough and Wang [1]. This reaffirms the notion that the same binary complex is being formed from the two approaches.

The greatest difference between the spectra using the present approach and the spectra using the diffusive trapping technique is found in the region of the  $\text{CO}_2$   $\nu_2$  bend absorption. This is understandable since bending mode absorptions are usually the most prone to changes in appearance due to differences in crystallinity and morphology of crystal particles. The carbon dioxide molecular group is  $D_{\infty h}$ , and the gas-phase  $\nu_2$  fundamental bending mode is doubly degenerate ( $\Pi_u$ ). The crystal structure is face-centered-cubic,  $T_h^6$ , with 4 molecules per unit cell, all on equivalent sites of symmetry  $C_{3i}$ . The  $\Pi_u$  mode is split through the  $C_{3i}$  into three components in the  $T_h^6$  factor group, only two of which are infrared active. The degeneracy of these modes is broken due to correlation field splitting [62]. The effects of crystal field splitting are due to interactions with the internal vibrations (i.e. vibrations analogous with gas-phase vibrations) of other molecules in the same unit cell of the crystal. Due to this intermolecular coupling, the potential energy will differ as the internal vibrations are in phase or partly out of phase in the unit cell. A single fundamental vibration can be split into up to  $m$  bands where  $m$  is the number of molecules in the unit cell.

The spectrum of pure carbon dioxide film prepared in this work exhibits a doublet with peak maxima at 654.7 and 659.7  $\text{cm}^{-1}$ . These peaks are narrow with the FWHM equal to 0.7 and 0.8  $\text{cm}^{-1}$ , respectively, suggesting the sample is very crystalline. The splitting is 5  $\text{cm}^{-1}$ , in agreement with the crystal spectra obtained by Falk [25].

The absorption spectrum of pure carbon dioxide microcrystallites produced in the diffusive trapping cell [2] appears quite different, than that of the bulk crystalline solid, in the  $\nu_2$  region of  $\text{CO}_2$ . These microcrystallites are typically less than 1  $\mu\text{m}$  in diameter and contain roughly  $10^9$  molecules. Two major bands are observed at 656.3 and 667.3  $\text{cm}^{-1}$  with relative integrated intensity 0.1:1. Note that although the  $\nu_2$  is split into two sharp components, implying crystallinity, the splitting, 10  $\text{cm}^{-1}$ , and intensity ratio are considerably different than the corresponding values of 5  $\text{cm}^{-1}$  and 0.8:1 in the bulk crystalline solid. These positions and intensities were reproduced from Mie theory [2, 28] using bulk optical constants. It was thus concluded that the particles of  $\text{CO}_2$  produced in the diffusive trapping cell were highly crystalline. The difference in appearance between spectra in the  $\nu_2$  region of the crystalline film and crystalline particles is a size effect, ultimately traceable to the discontinuity in the optical constants between those of the particle and those of the buffer gas: In the diffusive trapping cell a 1:50 mixture of carbon dioxide in helium buffer gas was used. An additional feature of the  $\nu_2$  bands is the presence of 4 side bands at the high frequency side of the main absorption. An electrostatic model [2, 27] was used to explain this feature in terms of the morphology of the microcrystallites.

In the spectrum of binary crystalline  $\text{CO}_2\text{-C}_2\text{H}_2$ , however, only a singlet at  $648.9\text{ cm}^{-1}$  is observed, suggesting that the carbon dioxide molecules are all arranged parallel to one another in identical environments. A second, much broader band with  $1/5$  the intensity of the previous band is observed at  $648.9\text{ cm}^{-1}$ . This is likely due to very small clusters of pure  $\text{CO}_2$  isolated within the binary crystal.

### 3.3 Discussion

The series of spectra in this work show remarkable similarities with the series of mixed  $\text{CO}_2\text{-C}_2\text{H}_2$  cluster spectra published by Gough and Wang [1]. Both methods show: the simultaneous appearance of shifted acetylene and shifted carbon dioxide absorption bands, the presence of a peak at  $1962\text{ cm}^{-1}$  only when the shifted bands are present, similar peak shapes and similar peak frequencies. Small variations in frequency and shape of the peaks may easily be attributed to the differences between the spectra of suspended microcrystallites and bulk crystal.

Another means of comparing the two methods is the ratio of the intensity of the shifted  $\nu_3$  absorption of acetylene divided by the intensity of the shifted  $\nu_1 + \nu_3$  absorption of carbon dioxide. Gough and Wang [1] found this ratio to be independent of initial flow concentrations, suggesting a distinct phase exists containing  $\text{CO}_2$  and  $\text{C}_2\text{H}_2$  in specific stoichiometry. This is true for the present method as well. Figure 3.10 shows the ratio of intensities to be constant over the entire range that the binary

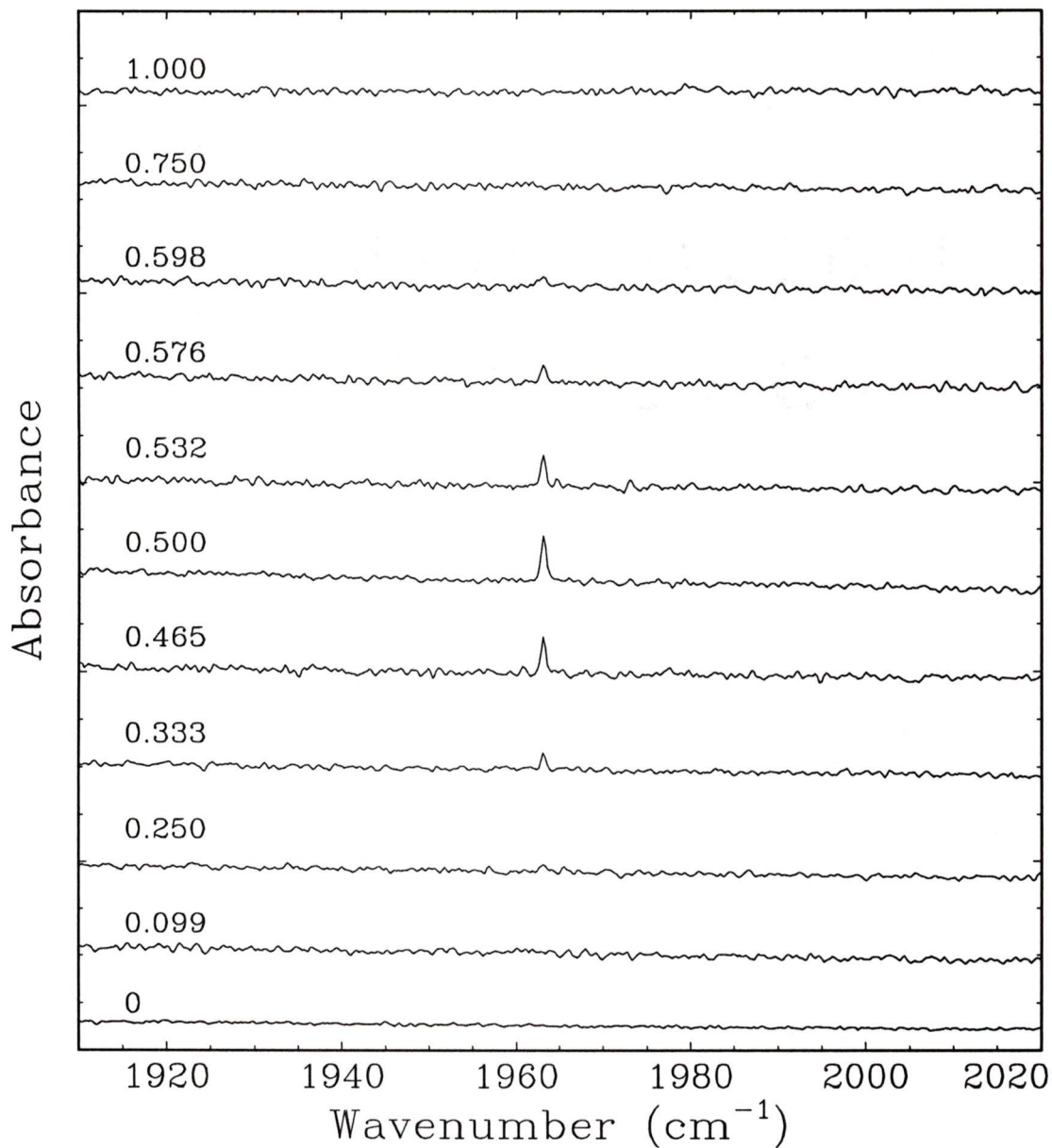


**Figure 3.9:** Selected spectra of the  $\nu_2$  fundamental band of  $C_2H_2$  in the binary phase. The spectra are labelled with gaseous mixture composition given in mole fraction of  $CO_2$ . The experimental conditions for recording these spectra are listed in Table 3.1.

phase is present. The intensity ratio is plotted as a function of mole fraction of carbon dioxide in the gas supply mixture. Intensity is expressed as the area under a particular absorption band as determined by curve fitting to a mixed Gaussian and Lorentzian profile. Asymmetric lineshapes were reproduced by adding extra Gaussian/Lorentzian curves to the fitting equation. No physical significance was given to the number of curves used. The error bars were generated from the error of the fit and from replicate fits. A weighted average value of this constant is  $13.9 \pm 0.5$  compared with the average value of  $15.3 \pm 1.0$  from the data given by Gough and Wang [1].

The good agreement between intensity ratios from this present method and the method described by Gough and Wang [1] as well as the similarity between peak shapes, peak frequencies, and the presence of new peaks at  $1962 \text{ cm}^{-1}$  has led to the conclusion that the same crystalline binary phase (with the same stoichiometry) is being produced by both methods. The slight difference between the intensity ratios may be due to the different methods of measuring the area under the curves. Previously, integration was used to determine the areas under each curve. The accuracy was thus limited by the uncertainty in the baseline.

The purpose of this work was to produce the same binary phase produced by Gough and Wang and to determine the stoichiometry. The series shows clearly that the new binary phase is most dominant at  $X_{\text{CO}_2} = 0.501$ , indicating that a 1:1 stoichiometry for  $\text{CO}_2 \cdot \text{C}_2\text{H}_2$ .

The previously suggested stoichiometry was 1:2 ( $\text{CO}_2 \cdot (\text{C}_2\text{H}_2)_2$ ). This was deter-

mined by comparing the ratio of the intensities of the acetylene  $\nu_3$  and carbon dioxide  $\nu_1 + \nu_3$  absorptions in the gas phase ( $7.1 \pm 0.8$ ) to the ratio obtained in the binary solid phase ( $15 \pm 1$ ). However, this assumes that the intensity in the gas phase is the same as the intensity in the solid phase *as well as* the solid binary phase. In light of the discrepancy between the stoichiometry determined from both methods, this assumption would seem questionable. It would thus be beneficial to know the relative absorption intensity between pure chromophore and its binary complexed counterpart. Since the stoichiometry of the binary phase, and the relative intensity between the absorption due to the binary acetylene  $\nu_3$  and the binary carbon dioxide  $\nu_1 + \nu_3$  are known, the relative intensity of the other two absorptions may be determined based on the following assumption: The concentration in the pulse of gas is conserved in the solid film.

In the range  $X_{\text{CO}_2}=0.372$  to  $X_{\text{CO}_2}=0.555$ , the major component is the binary complex. Three, at most, of the four bands shown in Figures 3.3 to 3.8 are present in appreciable amounts within this range. The curve fitted areas under these bands are thus used to calculate the intensities of the pure  $\text{CO}_2$  and  $\text{C}_2\text{H}_2$  absorptions relative to the complexed counterpart. This was calculated in the following manner: If  $X_{\text{CO}_2}=0.400$  and only bands due to pure  $\text{C}_2\text{H}_2$ , complexed  $\text{C}_2\text{H}_2$  and complexed  $\text{CO}_2$  are present, then 20% of the molecules are pure  $\text{C}_2\text{H}_2$ , 40% are complexed  $\text{C}_2\text{H}_2$  and 40% are complexed  $\text{CO}_2$ . Once the ratio of the areas under the acetylene bands ( $A_\alpha/A_P$ ) and the ratio of each type of molecule ( $N_\alpha/N_P$ ) has been established,

determination of the intensity ratio between complexed  $C_2H_2$  and pure  $C_2H_2$  ( $I_\alpha/I_P$ ) is trivial, since

$$\frac{I_\alpha}{I_P} = \frac{N_P A_\alpha}{N_\alpha A_P}. \quad (3.2)$$

The resulting values are averaged and shown in Table 3.3 as the absorption intensity relative to the  $\nu_3$  absorption of acetylene in the pure crystalline environment.

| Absorption                |                   | Intensity relative to pure solid $C_2H_2(\nu_3)$ |
|---------------------------|-------------------|--|
| $CO_2$<br>$\nu_1 + \nu_3$ | $\alpha$ -complex | 0.059  |
|                           | pure              | 0.042  |
| $C_2H_2$<br>$\nu_3$       | $\alpha$ -complex | 0.83   |
|                           | pure              | 1.0  |
| $C_2H_2$<br>$\nu_2$       | $\alpha$ -complex | 8.6 E-4  |
|                           | pure              | infrared inactive                                |

Table 3.3: Relative intensities for acetylene  $\nu_3$  and carbon dioxide  $\nu_1 + \nu_3$ .

Using these relative intensity values, the area under each peak may be converted to the relative number of moles. The mole fraction of each component present in the cryofilm may then be calculated and plotted as a function of  $CO_2$  mole fraction in the cryofilm. The resulting plot (Figure 3.11) is similar to a Job plot with the binary phase components reaching a maximum at  $X_{CO_2}=0.501$ . Figure 3.11 shows that the values given in Table 3.3 are appropriate over the entire range of mole fractions. This supports the redetermined 1:1 stoichiometry of the binary phase.

Note in Figure 3.11 that the cryofilms with a slight excess of  $C_2H_2$  ( $X_{CO_2}=0.489$  to  $X_{CO_2}=0.372$ ) contain pure  $C_2H_2$  as well as binary  $CO_2-C_2H_2$ . A pure  $CO_2$  phase, however, is absent. Note also that the cryofilms with a slight excess of  $CO_2$  ( $X_{CO_2}=0.511$  to  $X_{CO_2}=0.532$ ) contain pure  $CO_2$ , binary  $CO_2-C_2H_2$  and only trace amounts of pure  $C_2H_2$ . This is similar to a Job plot in which the equilibrium constant for formation of the complex is very large. Since only the complex and the component in excess are in solution in appreciable amounts, the amount of complex in the system decreases linearly as the mole fraction of either component is increased. The  $CO_2-C_2H_2$  system exhibits this linear behaviour in the region  $X_{CO_2}=0.372$  to  $X_{CO_2}=0.532$ . Outside this region, the amount of binary phase in the solid does not decrease linearly from the maximum in Figure 3.11. This deviation from linearity suggests that  $CO_2-CO_2$  and  $C_2H_2-C_2H_2$  interactions compete with  $CO_2-C_2H_2$  in the formation of the cryofilm solid. This will be examined in more detail in Chapter 5. Deviation from linearity is much greater on the  $CO_2$  rich side (binary phase is almost absent in the  $X_{CO_2}=0.598$  cryofilm). This is due to  $CO_2-CO_2$  interactions being stronger than  $C_2H_2-C_2H_2$  interactions and therefore more effectively inhibit  $CO_2-C_2H_2$  formation.

### 3.4 Conclusion

Spectroscopic evidence has been presented for the existence of a bulk crystalline mixed phase containing carbon dioxide and acetylene in a specific stoichiometry amount.

With the assumption that the gas mixture concentration is preserved in the deposited solid, due to a high sticking coefficient, the stoichiometry of the novel binary complex formed from  $\text{CO}_2$  and  $\text{C}_2\text{H}_2$  has been shown to be 1:1. The previous assumptions concerning the absorption intensities have been shown to be unjustified. For instance, the intensity ratio between pure  $\text{CO}_2$   $\nu_1 + \nu_3$  and pure  $\text{C}_2\text{H}_2$   $\nu_3$  has tripled from 7.1 [26] in the gas phase to 23.7 in the solid phase.

It appears that only through non-equilibrium pathways is  $\text{CO}_2 \cdot \text{C}_2\text{H}_2$  formed. This apparent behaviour leads to questions about the nucleation mechanism and stability of  $\text{CO}_2 \cdot \text{C}_2\text{H}_2$  with respect to the pure phases. Experiments were carried out in order to characterize the stability of the binary phase; the results of which are covered in Chapter 5.

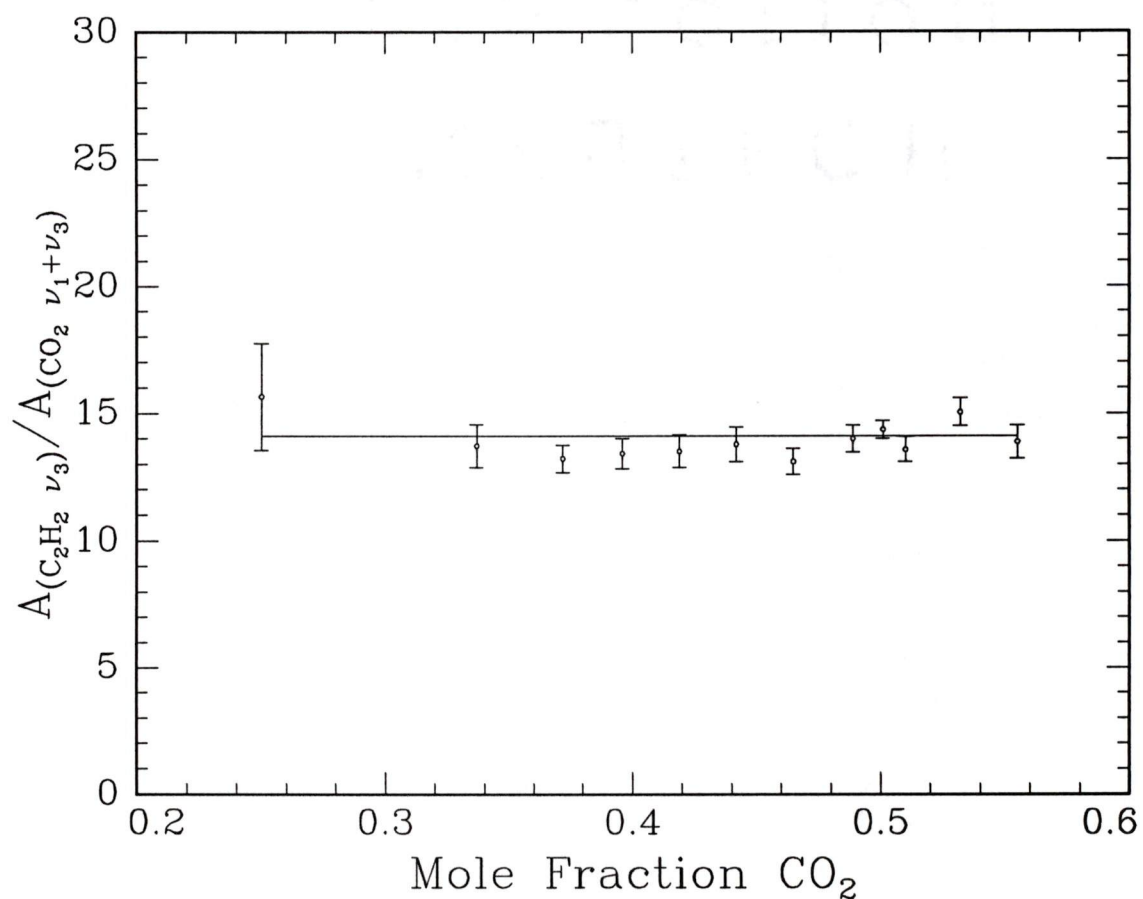


**Figure 3.10:** The intensity ratio of the shifted  $\nu_3$  fundamental absorption of acetylene to the shifted  $\nu_1 + \nu_3$  combination band absorption of carbon dioxide plotted as a function of  $\text{CO}_2$  mole fraction.  $A_{\text{CO}_2}$  and  $A_{\text{C}_2\text{H}_2}$  are the curve fitted areas corresponding to the absorptions in Figures 3.3 through 3.8.

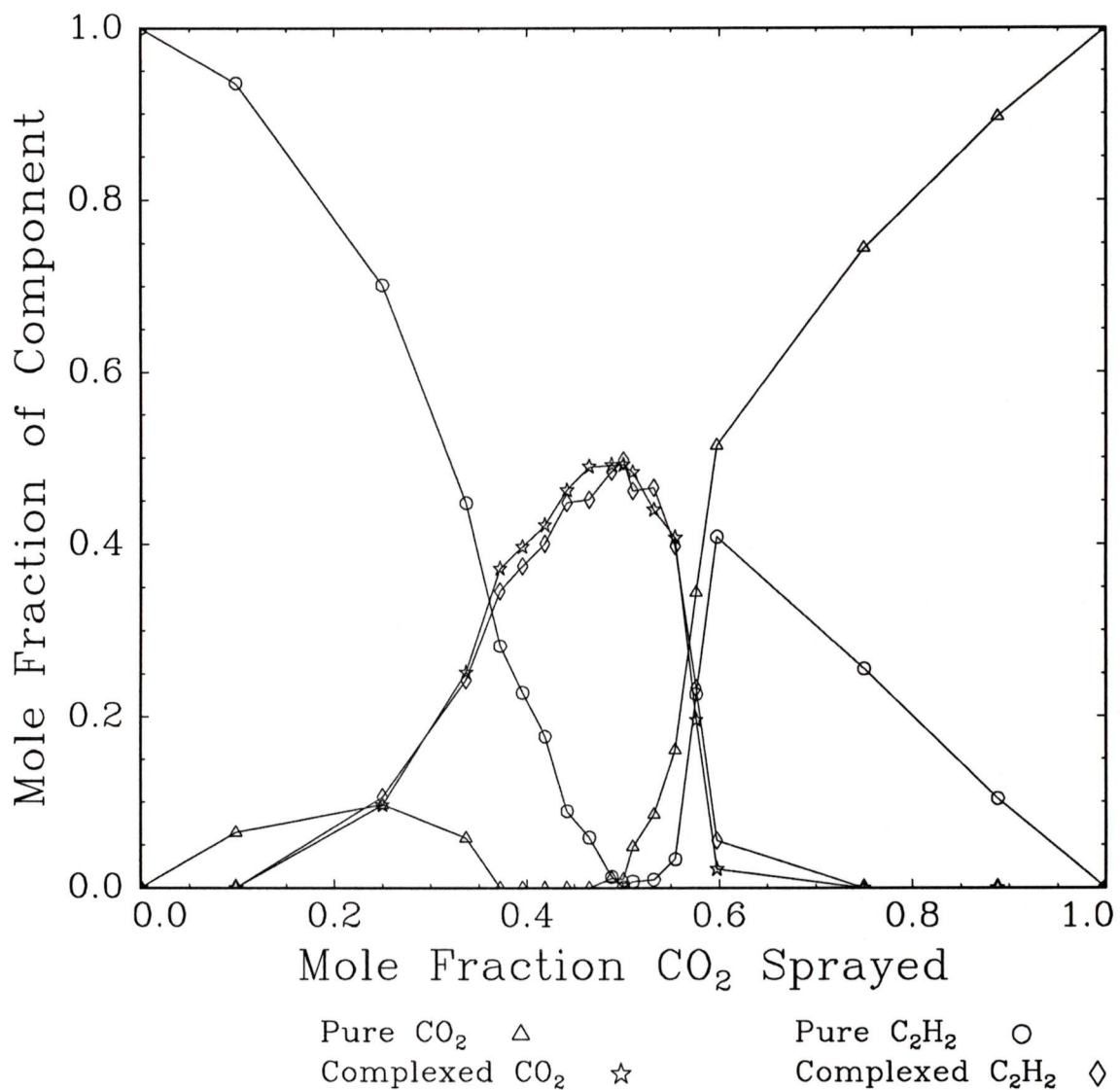


**Figure 3.11:** A systematic variation graph derived from the fitted areas under each curve. Relative band intensities given in Table 3.3 are used to convert area to mole fraction.

## Chapter 4

# Nitrous Oxide - Acetylene

## Cryofilm

### 4.1 Introduction

In Chapter 3, a novel binary crystalline phase containing carbon dioxide and acetylene was shown to have a stoichiometry of 1:1. The success in producing bulk  $\text{CO}_2\cdot\text{C}_2\text{H}_2$  on a cooled window leads to the prospect of expanding the study to include other species. For this purpose we recently investigated the mixtures of nitrous oxide and acetylene using the same cold window/supersonic nozzle assembly as described previously.

The existence of  $\text{CO}_2\cdot\text{C}_2\text{H}_2$  is due to several key  $\text{CO}_2$  properties. It has a similar magnitude quadrupole moment as  $\text{C}_2\text{H}_2$  but an opposite sign. Carbon dioxide is

linear and similar in length to acetylene. The two pure substances have similar crystal structures, both being face centered cubic.

With regard to these properties,  $N_2O$  is very similar to  $CO_2$ . It is because of these similarities that  $N_2O$  and  $CO_2$  are mutually miscible [2] with  $N_2O$  molecules most likely substituting  $CO_2$  molecules in the crystal lattice. It is conceivable that a mixed binary phase of  $N_2O$  (in place of  $CO_2$ ) and  $C_2H_2$  may be formed by the same procedure outlined in Chapter 3.

Unlike carbon dioxide, however, nitrous oxide is not symmetric, thus having a permanent electric dipole moment. It also has a higher vapour pressure, closer to that of acetylene. As mentioned, the symmetry of the  $N_2O$  molecule is lower than the  $CO_2$  molecule. As a result, the  $N_2O$  crystal structure ( $T^4 - P_{2,3}$ ) is lower in symmetry than the structure of the  $CO_2$  crystal ( $T_h^6 - P_3$ ) [29]. The consequence is that the solid nitrous oxide infrared spectrum exhibits many more transitions than carbon dioxide. This means that more information on the structure of the binary solid may be extracted.

Frequency shifted absorption bands were, in fact, observed in spectra of cryofilm consisting of a mixture of nitrous oxide and acetylene. The spectra obtained are very similar to the ones shown for the  $CO_2$ - $C_2H_2$  system. The shifted absorption of the  $\nu_3$  fundamental stretch of  $C_2H_2$ , for instance, was almost identical in shape and position to its  $CO_2$ - $C_2H_2$  counterpart. A major difference is the presence of a *second* distinct binary phase in the  $N_2O$ - $C_2H_2$  system. This new binary phase will be

referred to as the  $\beta$ -phase while the binary phase similar to  $\text{CO}_2\cdot\text{C}_2\text{H}_2$  will be referred to as the  $\alpha$ -phase. In the same manner as discussed in Chapter 3, a concentration dependent series of nitrous oxide and acetylene mixed cryofilms was used to determine the specific stoichiometry of the binary phase produced.

## 4.2 Experimental Conditions

The apparatus and technique used in this study are the same as those described in Chapters 2 and 3 . Unless otherwise specified, all cryofilms were condensed onto a ZnSe window cooled to 90 K using a single 500 ms pulse from the mixing board; the temperature was then held constant at 90 K while each FTIR spectrum was recorded at a resolution of  $0.50\text{ cm}^{-1}$  with 64 co-added scans. The spectral range is 550 to  $4000\text{ cm}^{-1}$ .

Table 4.1 gives the experimental conditions used in the preparation of each  $\text{N}_2\text{O}$  and  $\text{C}_2\text{H}_2$  containing cryofilm. The mass flow controller used previously for  $\text{CO}_2$  was re-calibrated for  $\text{N}_2\text{O}$ . Concentration, given in mole fraction of nitrous oxide ( $X_{\text{N}_2\text{O}}$ ), was varied across the entire range from pure  $\text{N}_2\text{O}$  to pure  $\text{C}_2\text{H}_2$ .

As with the carbon dioxide - acetylene system, attention will be focused on the  $\nu_3$  fundamental absorption of acetylene and the  $\nu_1 + \nu_3$  absorption of nitrous oxide. Assigned frequencies for these bands are given in Table 4.2. The features due to acetylene are very similar to the  $\text{CO}_2\text{-C}_2\text{H}_2$  system. Peak shapes are indistinguishable

from one binary system to the other, and frequency shifts are similar. For instance, the absorption due to the  $\nu_3$  fundamental band of acetylene in the binary phase occurs at  $3256.5\text{ cm}^{-1}$  for  $\text{CO}_2\text{-C}_2\text{H}_2$ , at  $3256.0\text{ cm}^{-1}$  for the  $\text{N}_2\text{O-C}_2\text{H}_2$  binary  $\alpha$  phase. A “new” absorption located at  $3239\text{ cm}^{-1}$  is due to acetylene in a second binary ( $\beta$ ) phase not observed in the  $\text{CO}_2\text{-C}_2\text{H}_2$  study.

The shift in frequency for  $\text{N}_2\text{O}$  absorptions due to the binary phase are not as large as those found in the  $\text{CO}_2\text{-C}_2\text{H}_2$  system. The  $\nu_1 + \nu_3$  absorption of nitrous oxide in the binary  $\alpha$  phase, for instance, is only red shifted by  $3.5\text{ cm}^{-1}$  from the absorption due to pure nitrous oxide. With an FWHM greater than  $3\text{ cm}^{-1}$ , the peaks are not completely resolved. The absolute absorption intensity ratios given in Table 4.3 are therefore not as accurate as the ratios deduced for the  $\text{CO}_2\text{-C}_2\text{H}_2$  system.

Figures 4.1 to 4.3 show FTIR spectra of the  $\nu_1 + \nu_3$  absorption of nitrous oxide for various  $\text{N}_2\text{O-C}_2\text{H}_2$  mixtures and Figures 4.4 to 4.6 show FTIR spectra of the  $\nu_3$  absorption of acetylene for various  $\text{N}_2\text{O-C}_2\text{H}_2$  mixtures. The spectra are labelled with gaseous mixture composition given in mole fraction of  $\text{N}_2\text{O}$ .

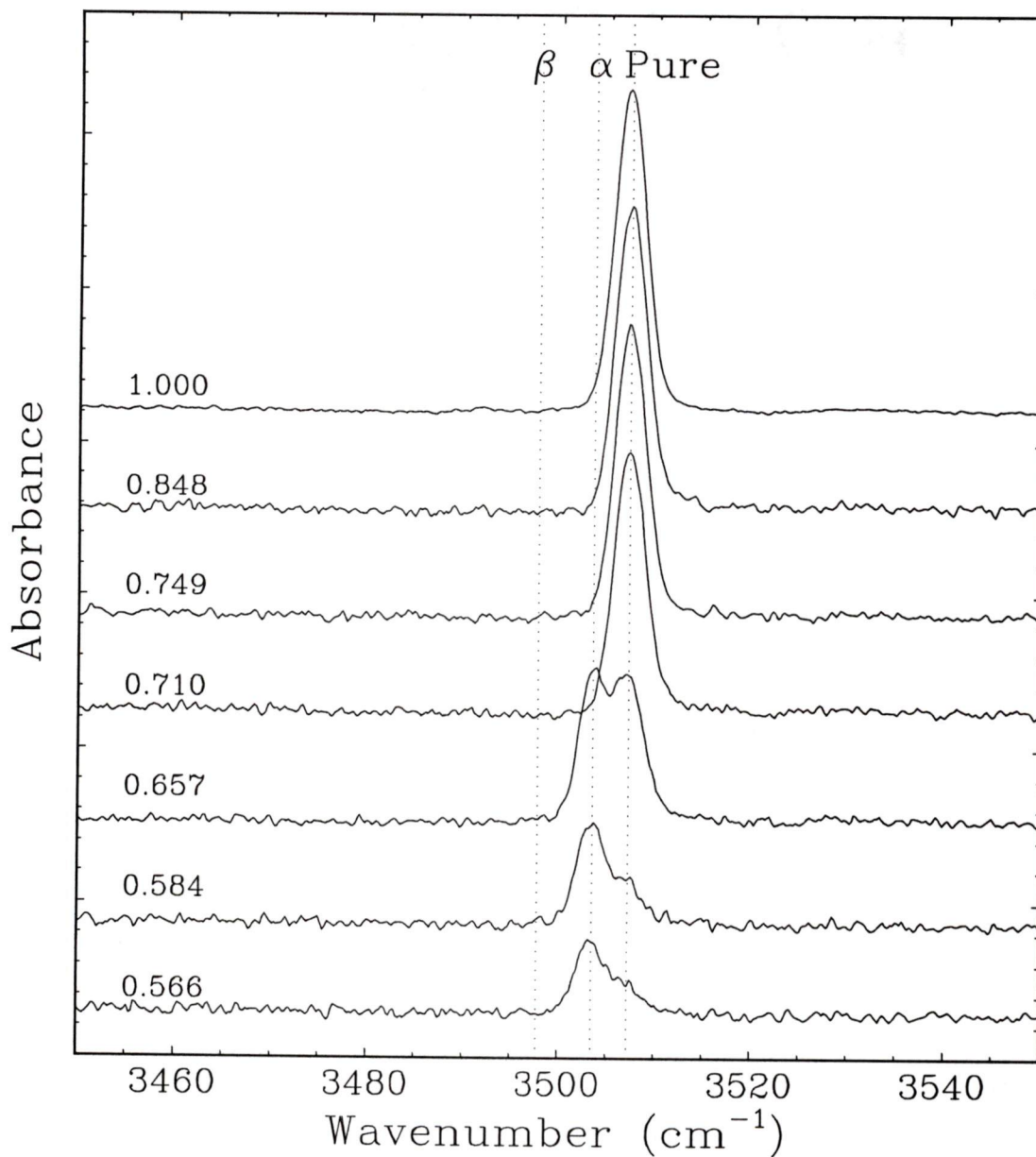


**Figure 4.1:** Spectra of the  $\nu_1 + \nu_3$  combination band of  $N_2O$  for various  $N_2O-C_2H_2$  mixtures rich in  $N_2O$ . The spectra are labelled with gaseous mixture composition given in mole fraction of  $N_2O$ . The experimental conditions for recording these spectra are listed in Table 4.1.

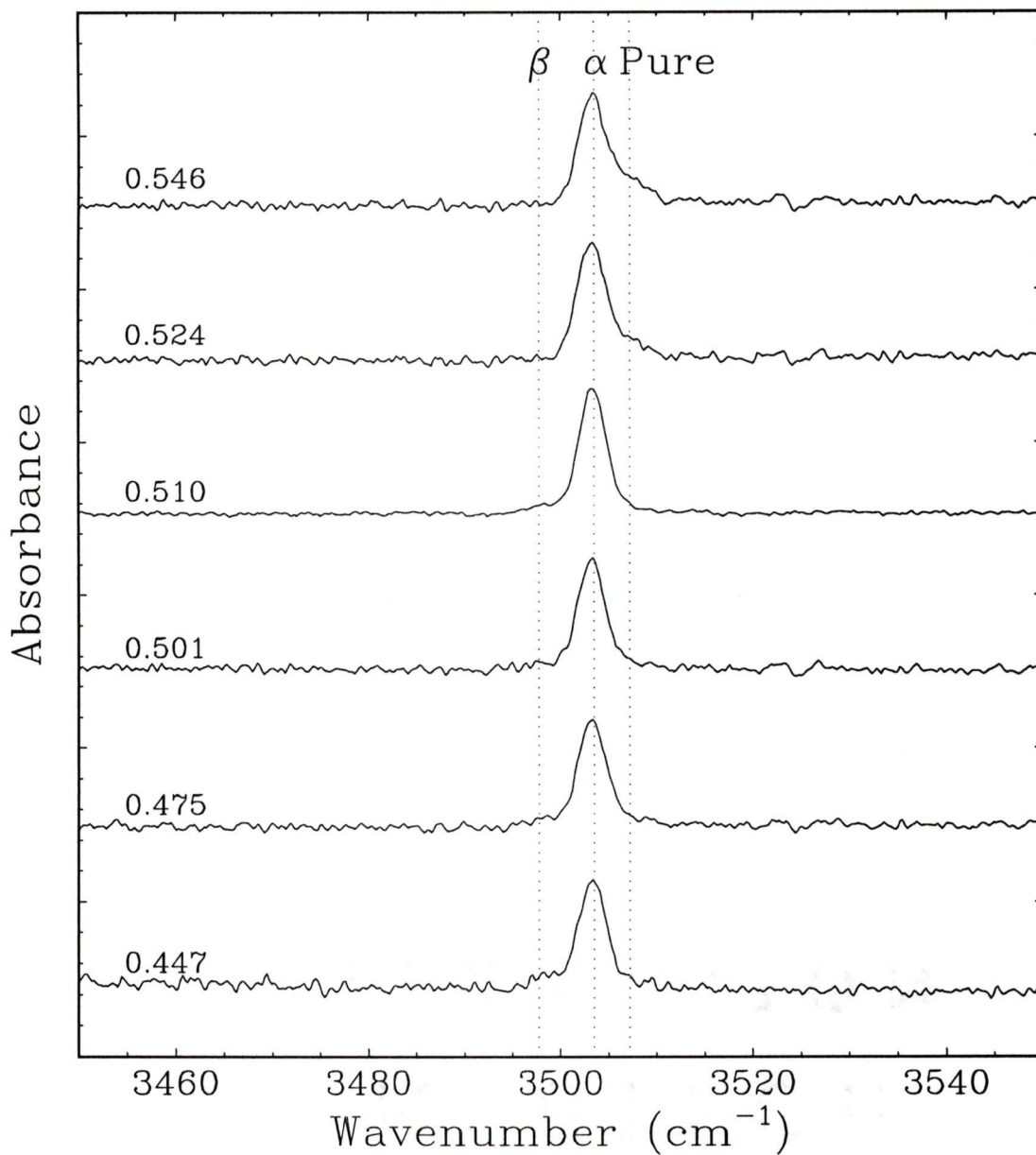


**Figure 4.2:** Spectra of the  $\nu_1 + \nu_3$  combination band of  $\text{N}_2\text{O}$  for various  $\text{N}_2\text{O}$ - $\text{C}_2\text{H}_2$  mixtures containing roughly equal amounts of  $\text{N}_2\text{O}$  and  $\text{C}_2\text{H}_2$ . The spectra are labelled with gaseous mixture composition given in mole fraction of  $\text{N}_2\text{O}$ . The experimental conditions for recording these spectra are listed in Table 4.1.

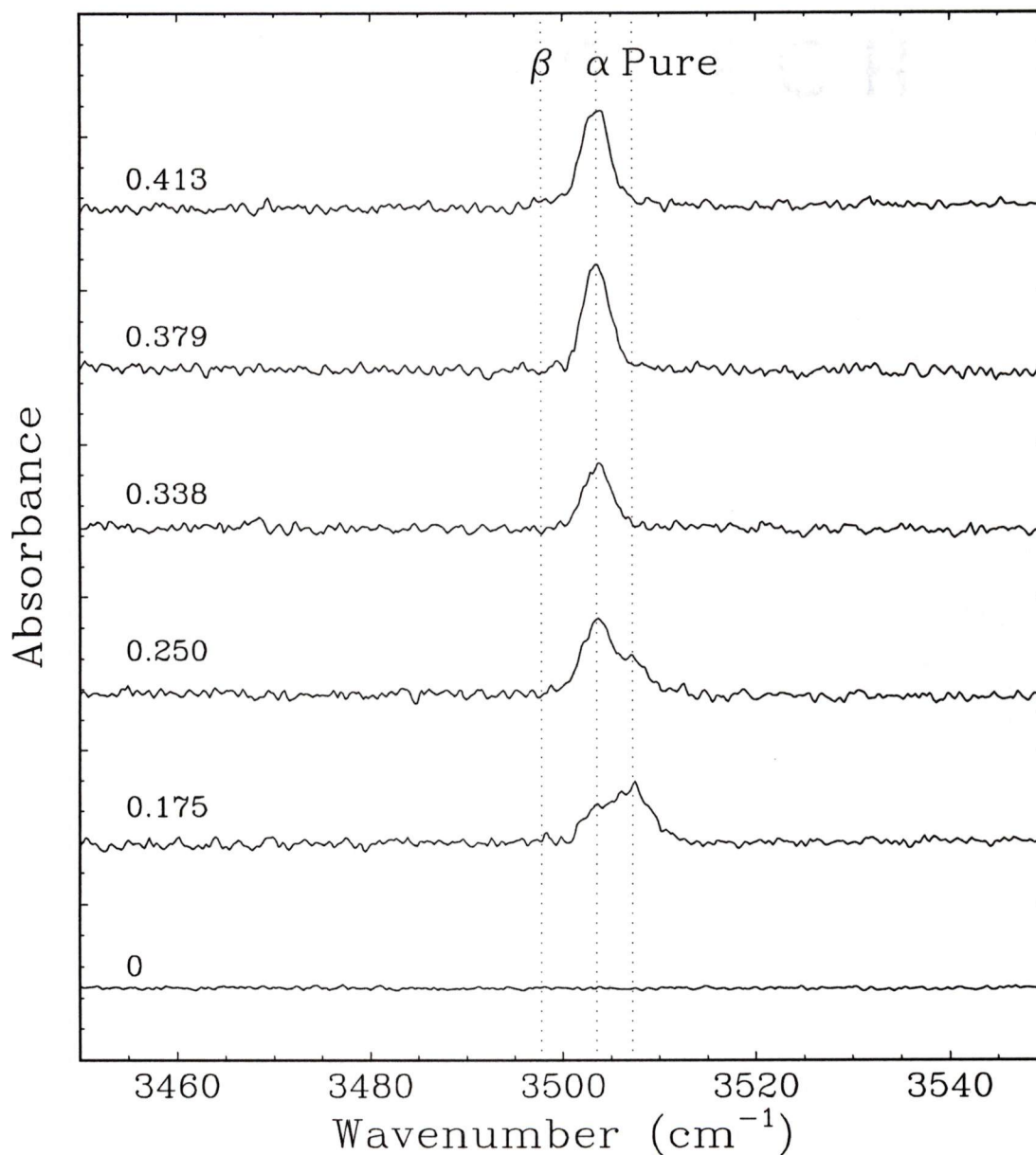


**Figure 4.3:** Spectra of the  $\nu_1 + \nu_3$  combination band of  $N_2O$  for various  $N_2O$ - $C_2H_2$  mixtures rich in  $C_2H_2$ . The spectra are labelled with gaseous mixture composition given in mole fraction of  $N_2O$ . The experimental conditions for recording these spectra are listed in Table 4.1.

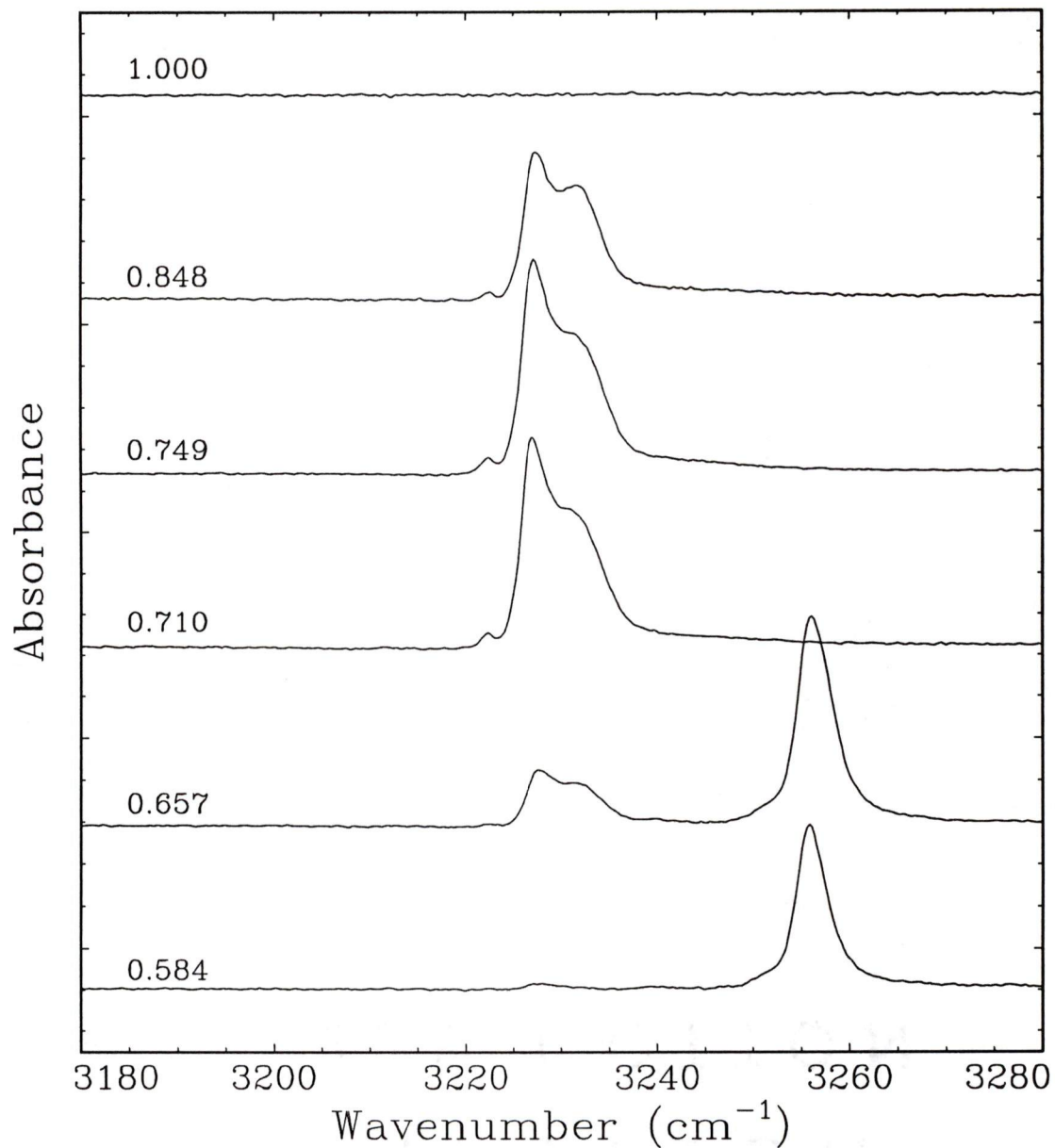


**Figure 4.4:** Spectra of the  $\nu_3$  fundamental band of  $C_2H_2$  for various  $N_2O-C_2H_2$  mixtures rich in  $N_2O$ . The spectra are labelled with gaseous mixture composition given in mole fraction  $N_2O$ . The experimental conditions for recording these spectra are listed in Table 4.1.

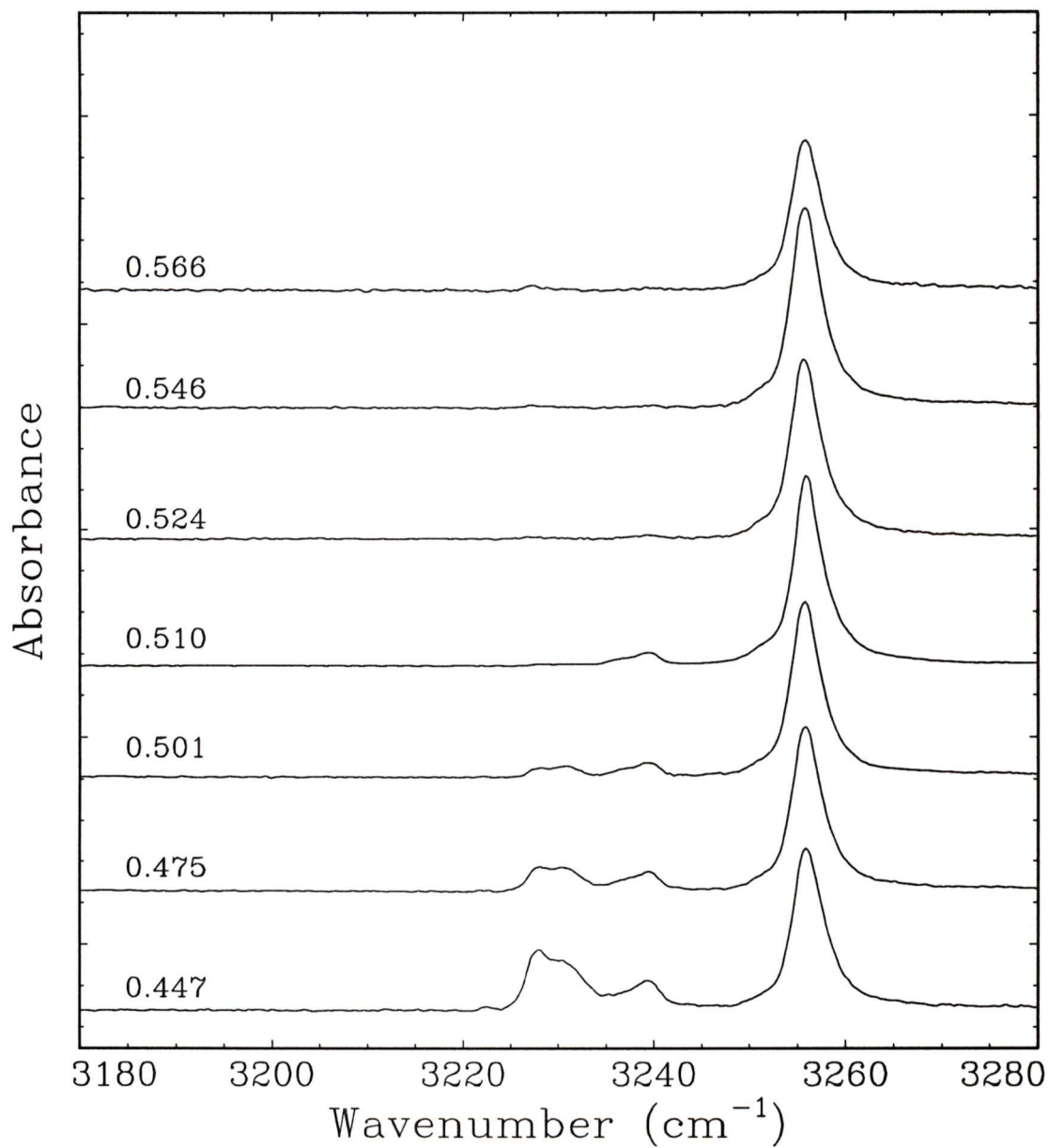


**Figure 4.5:** Spectra of the  $\nu_3$  fundamental band of  $C_2H_2$  for various  $N_2O$ - $C_2H_2$  mixtures containing roughly equal amounts of  $N_2O$  and  $C_2H_2$ . The spectra are labelled with gaseous mixture composition given in mole fraction  $N_2O$ . The experimental conditions for recording these spectra are listed in Table 4.1.

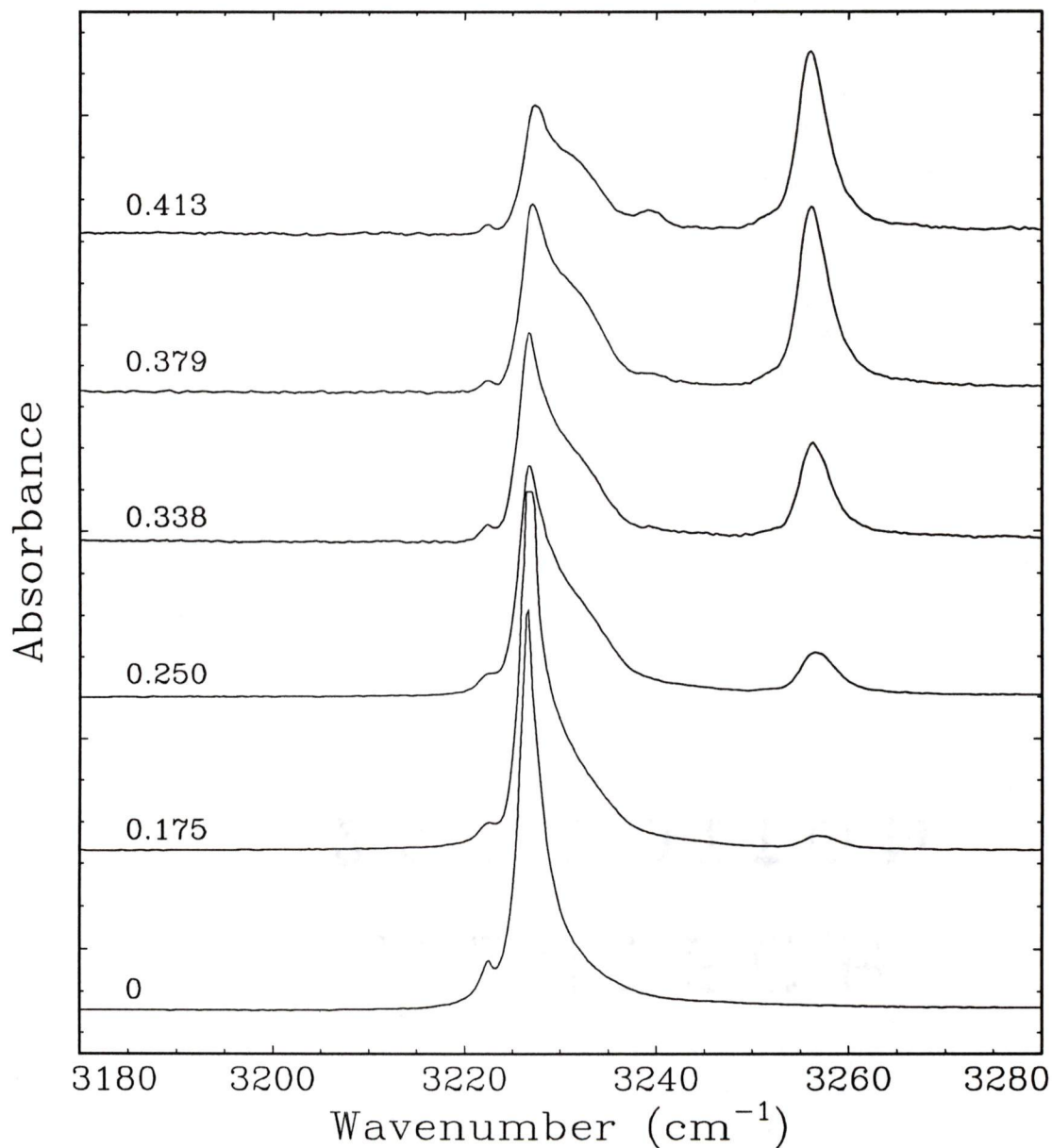


**Figure 4.6:** Spectra of the  $\nu_3$  fundamental band of  $C_2H_2$  for various  $N_2O$ - $C_2H_2$  mixtures rich in  $C_2H_2$ . The spectra are labelled with gaseous mixture composition given in mole fraction  $N_2O$ . The experimental conditions for recording these spectra are listed in Table 4.1.

| Mole Fraction<br>N <sub>2</sub> O | V <sub>N<sub>2</sub>O</sub><br>(mV) | F <sub>N<sub>2</sub>O</sub><br>(SCCM) | V <sub>C<sub>2</sub>H<sub>2</sub></sub><br>(mV) | F <sub>C<sub>2</sub>H<sub>2</sub></sub><br>(SCCM) |
|-----------------------------------|-------------------------------------|---------------------------------------|---|---|
| 0.00                              | 0.0                                 | 0.0                                   | 0.550   | 0.995   |
| 0.175                             | 0.580                               | 1.275                                 | 0.550   | 6.017   |
| 0.250                             | 0.580                               | 1.275                                 | 2.00  | 3.83  |
| 0.338                             | 0.190                               | 0.508                                 | 0.550   | 0.995   |
| 0.379                             | 0.240                               | 0.606                                 | 0.550   | 0.995   |
| 0.413                             | 0.288                               | 0.701                                 | 0.550   | 0.995   |
| 0.447                             | 0.340                               | 0.803                                 | 0.550   | 0.995   |
| 0.475                             | 0.389                               | 0.899                                 | 0.550   | 0.995   |
| 0.501                             | 0.439                               | 0.997                                 | 0.550   | 0.995   |
| 0.510                             | 0.459                               | 1.037                                 | 0.550   | 0.995   |
| 0.524                             | 0.489                               | 1.096                                 | 0.550   | 0.995   |
| 0.546                             | 0.540                               | 1.196                                 | 0.550   | 0.995   |
| 0.566                             | 0.592                               | 1.298                                 | 0.550   | 0.995   |
| 0.584                             | 0.642                               | 1.397                                 | 0.550   | 0.995   |
| 0.657                             | 0.900                               | 1.904                                 | 0.550   | 0.995   |
| 0.684                             | 1.025                               | 2.15                                  | 0.550   | 0.995   |
| 0.710                             | 1.172                               | 2.44                                  | 0.550   | 0.995   |
| 0.749                             | 1.438                               | 2.96                                  | 0.550   | 0.995   |
| 0.848                             | 2.76                                | 5.56                                  | 0.552   | 0.999   |
| 1.00                              | 2.76                                | 5.56                                  | 0.0   | 0.0   |

Table 4.1: Experimental conditions used for the recording of spectra in the nitrous oxide - acetylene series.  $V_{N_2O}$  and  $V_{C_2H_2}$  are the voltages applied to the corresponding mass flow controllers. Flow rates are given in standard cubic centimeters per minute (SCCM). The pressure in the gas mixing chamber was 60 Torr at the time of deposition. The temperature of the ZnSe window was held constant at 90 K during deposition and recording of spectra. One 500 ms pulse of gas was delivered for each film. Each spectrum was recorded at  $0.50 \text{ cm}^{-1}$  resolution and consists of 64 scans co-added. The spectral range is 550 to  $4000 \text{ cm}^{-1}$ .

C<sub>2</sub>H<sub>2</sub> Infrared Frequencies

| Gas                   | Crystalline <sup>a</sup><br>at 63 K | Pure Solid <sup>b</sup><br>at 90 K | $\alpha$ Phase <sup>b</sup><br>at 90 K | $\beta$ Phase <sup>b</sup><br>at 90 K | Assignment              |
|-----------------------|-------------------------------------|------------------------------------|--|---------------------------------------|-------------------------|
| 3296.8 <sup>c</sup>   | 3331                                | 3307.5                             | 3307.4                                 | 3326.9                                | $\nu_2 + \nu_4 + \nu_5$ |
| 3288.6 <sup>c</sup>   | 3226.3                              | 3227                               | 3256.0                                 | 3236.9, 3239.6                        | $\nu_3$                 |
| 1973.8 <sup>d,e</sup> |                                     | (1958) <sup>f</sup>                | 1962.5                                 | 1958.6                                | $\nu_2$                 |
| 1327 <sup>g</sup>     | 1422, 1390<br>1377                  | 1389.5                             | 1354.4                                 | 1380.8                                | $\nu_4 + \nu_5$         |
| 729.3 <sup>h</sup>    | 768.8, 760.7                        | 768, 760                           | 748.6                                  | 753.8, 768.2                          | $\nu_5$                 |

N<sub>2</sub>O Infrared Frequencies

| Gas <sup>d</sup>    | Crystalline <sup>j</sup><br>at 80 K | Pure Solid<br>at 90 K | $\alpha$ Phase<br>at 90 K | $\beta$ Phase<br>at 90 K | Assignment                |
|---------------------|-------------------------------------|-----------------------|---------------------------|--------------------------|---------------------------|
| 3482.2              | 3508.0                              | 3507.2                | 3503.5                    | 3498.1                   | $\nu_1 + \nu_3$           |
| 3365.6              |                                     | 3378.7                | 3368.8                    | 3367.9                   | $2\nu_2 + \nu_3$          |
| 2798.3              | 2813.7                              | 2813.4                | 2806.9                    | 2805.5                   | $\nu_2 + \nu_3$           |
| 2563.5              | 2579.5                              | 2579.5                | 2574.1                    | 2572.3                   | $2\nu_1$                  |
| 2461.5              | 2473.4                              | 2468.2                | 2456.4                    | 2458.5                   | $\nu_1 + 2\nu_2$          |
| 2223.5              | 2238                                | 2236.5                | 2236.3                    | 2235.9                   | $\nu_3$                   |
| 2201.0 <sup>i</sup> | 2219.7                              | 2218.4                | 2217.3                    | 2213.4                   | $N^{15}N^{14}O^{16}\nu_3$ |
| 2177.0 <sup>i</sup> | 2195.8                              | 2194.9                | 2193.4                    | 2189.7                   | $N^{14}N^{15}O^{16}\nu_3$ |
| 1868.0              | 1891                                | 1888.2                | 1878.1                    | 1880.2                   | $\nu_1 + \nu_2$           |
| 1285.4              | 1293.4                              | 1292.6                | 1289.8                    | 1291                     | $\nu_1$                   |
| 1167.3              | 1165.6                              | 1165.2                | 1157                      | 1159.9                   | $2\nu_2$                  |
| 588.8               | 591.0                               | 588.8                 | 581.2, 587                | 583, 584, 585.5          | $\nu_2$                   |

<sup>a</sup> Reference [17]

<sup>b</sup> Sprayed cryofilm, this work.

<sup>c</sup> Reference [20]

<sup>d</sup> Reference [22]

<sup>e</sup> Raman active

<sup>f</sup> Calculated from  $\nu_T$  combination modes. See Figure 3.2.

<sup>g</sup> Reference [23]

<sup>h</sup> Reference [24]

<sup>i</sup> Reference [30]

<sup>j</sup> Reference [29]

Table 4.2: Absorption frequencies (cm<sup>-1</sup>) of C<sub>2</sub>H<sub>2</sub> and N<sub>2</sub>O.

### 4.3 Results

In Figure 4.1, the spectrum labelled  $X_{\text{N}_2\text{O}}=1.000$  shows the  $\nu_1 + \nu_3$  combination band absorption of crystalline nitrous oxide with its peak maximum occurring at  $3507.3 \text{ cm}^{-1}$ . This agrees well with the value of  $3508 \text{ cm}^{-1}$  given by Dows for pure crystalline nitrous oxide  $\nu_1 + \nu_3$  at 80 K [29]. The appearance of a “new” peak red shifted to  $3503.5 \text{ cm}^{-1}$  at the higher acetylene concentration of  $X_{\text{N}_2\text{O}}=0.66$  indicates the presence of the binary  $\alpha$  phase of  $\text{N}_2\text{O}$  and  $\text{C}_2\text{H}_2$ . The peak due to pure  $\text{N}_2\text{O}$  continues to disappear until it no longer remains at  $X_{\text{N}_2\text{O}}=0.510$ . The  $\alpha$  binary peak remains dominant until  $X_{\text{N}_2\text{O}}=0.175$ .

The location of the  $\nu_1 + \nu_3$  absorption due to  $\text{N}_2\text{O}$  in the binary  $\beta$  phase is indicated at  $3498.1 \text{ cm}^{-1}$ . It is barely noticeable in Figure 4.2. In the region of the  $\text{C}_2\text{H}_2$  asymmetric C-H stretch, the binary phase appears as a pair of peaks at  $3236.9$  and  $3239.6 \text{ cm}^{-1}$ . It should be noted that the purpose of this series is to determine the stoichiometry of the  $\alpha$  phase. Thus, formation conditions were chosen such that the  $\alpha$  phase was favoured.

The acetylene  $\nu_3$  series shows the same behaviour as with the  $\text{CO}_2\text{-C}_2\text{H}_2$  system. Figure 4.6 shows the presence of the  $\alpha$  binary phase in mixtures very rich in  $\text{C}_2\text{H}_2$ . The pure phase gradually disappears until only the binary phases are present at  $X_{\text{N}_2\text{O}}=0.510$ . Pure acetylene reappears suddenly at  $X_{\text{N}_2\text{O}}=0.657$  and is the only acetylene phase present at  $X_{\text{N}_2\text{O}}=0.710$ .

As with the  $\text{CO}_2\text{-C}_2\text{H}_2$  system, the presence of a binary complex is indicated by an absorption in the region of the infrared inactive  $\nu_2$  symmetric C-C stretch of acetylene. The absorptions due to  $\text{C}_2\text{H}_2$  in the  $\alpha$  and  $\beta$  phases are centred at 1962.5 and 1958.6  $\text{cm}^{-1}$ , respectively. Selected spectra of the  $\nu_2$  fundamental band of  $\text{C}_2\text{H}_2$  are shown in Figure 4.7. Note the absence of absorption in the pure spectrum of either chromophore.

## 4.4 Discussion

The series shown clearly demonstrates that the binary  $\alpha$  phase is most dominant near  $X_{\text{N}_2\text{O}}=0.5$ . This suggests a 1:1 stoichiometry for the binary complex  $\alpha\text{-N}_2\text{O}\cdot\text{C}_2\text{H}_2$ .

The ratio of the intensity of the shifted  $\nu_3$  absorption of acetylene divided by the intensity of the shifted  $\nu_1 + \nu_3$  absorption of nitrous oxide appears to be independent of concentration. Thus, the new environment for nitrous oxide and the new environment for acetylene are the same binary phase containing  $\text{N}_2\text{O}$  and  $\text{C}_2\text{H}_2$  in a specific stoichiometry. In this case, 1:1. The intensity ratio is shown in Figure 4.8 plotted as a function of  $\text{N}_2\text{O}$  mole fraction. Intensity is expressed as the area under a particular absorption band. The method of determining the area by curve fitting was described in Chapter 3. Gough and Wang found the average intensity ratio of intensities for the  $\alpha$  phase  $\nu_3 \text{C}_2\text{H}_2/\nu_1 + \nu_3 \text{CO}_2$  to be 10.2. We determined the average value to be  $14.1 \pm 0.7$ . Oddly, while the values are dissimilar between the two studies, our

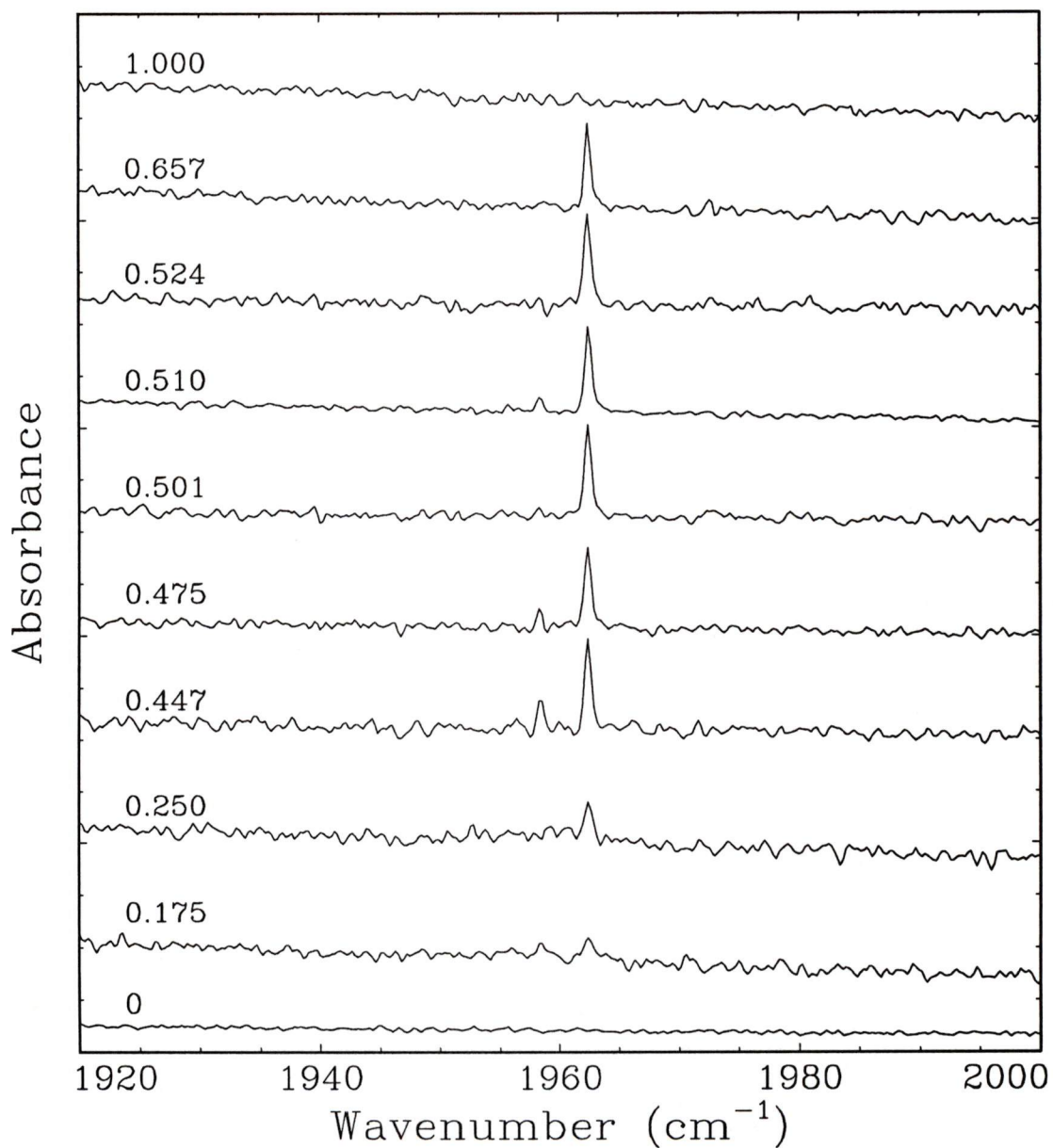


**Figure 4.7:** Selected spectra of the  $\nu_2$  fundamental band of  $C_2H_2$  in the binary phases. The spectra are labelled with gaseous mixture composition given in  $N_2O$  mole fraction. The experimental conditions for recording these spectra are listed in Table 4.1.

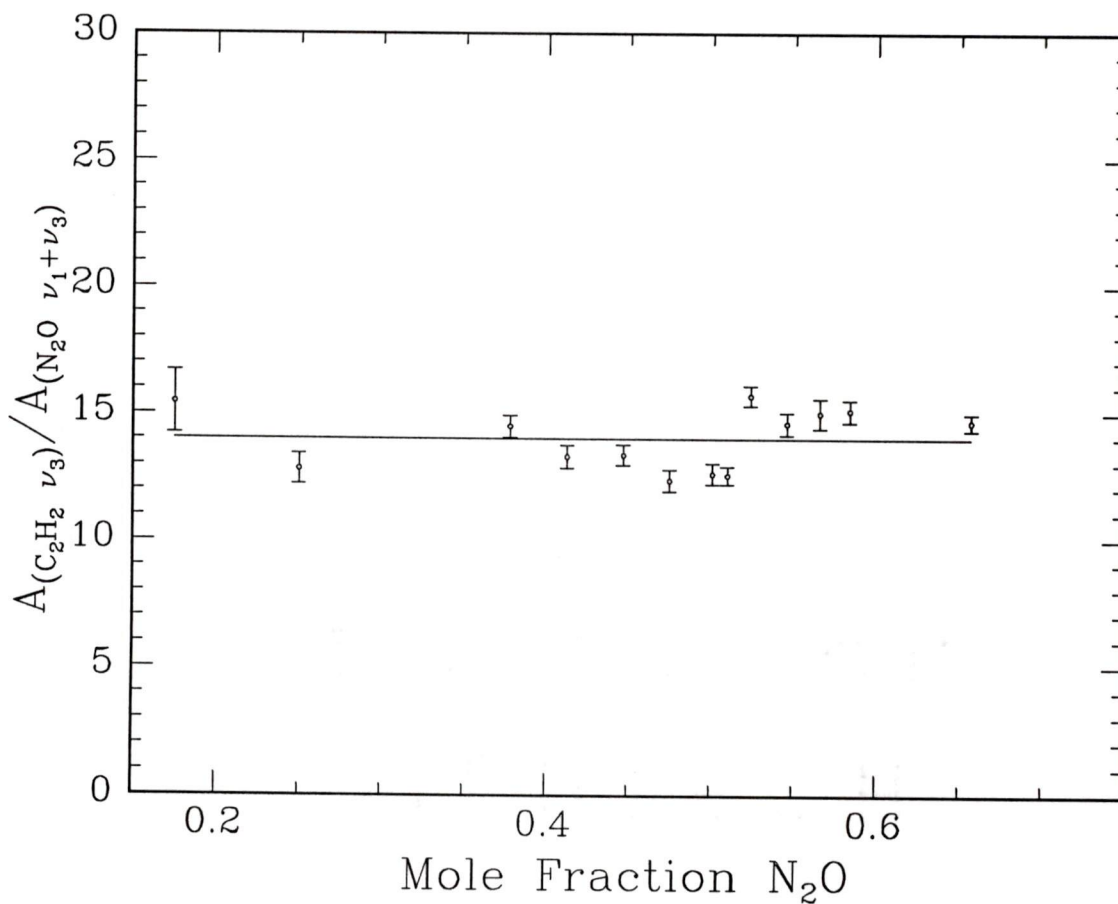


**Figure 4.8:** The intensity ratio of the shifted  $\nu_3$  fundamental absorption of acetylene to the shifted  $\nu_1 + \nu_3$  combination band absorption of nitrous oxide plotted as a function of  $\text{N}_2\text{O}$  mole fraction.  $A_{\text{N}_2\text{O}}$  and  $A_{\text{C}_2\text{H}_2}$  are the curve fitted areas corresponding to the absorptions in Figures 3.3 through 3.8.

present value is very close to the  $\text{CO}_2\cdot\text{C}_2\text{H}_2$  ratio of  $13.9 \pm 0.5$ .

The areas under the  $\beta\text{-N}_2\text{O}\cdot\text{C}_2\text{H}_2$  absorptions shown in this chapter are much too small to accurately determine a value for the ratio of intensities. Thus, a ratio of intensities value for the  $\beta$  phase was determined using data presented in Chapter 5, Section 5.1.2. We found the ratio,  $22 \pm 4$ , to be markedly different than the  $\alpha$  phase ratio as well as the value of 10.2 determined by Gough and Wang for the  $\beta$  phase. The relative intensities for this study are tabulated in Figure 4.3.

| Absorption                              |                   | Intensity relative to the $\nu_3$ absorption of $\text{C}_2\text{H}_2$ in the pure solid environment |
|---|-------------------|--|
| $\text{N}_2\text{O}$<br>$\nu_1 + \nu_3$ | pure              | 0.0394   |
|   | $\alpha$ -complex | 0.0435   |
|   | $\beta$ -complex  | 0.020  |
| $\text{C}_2\text{H}_2$<br>$\nu_3$       | pure              | 1.00   |
|   | $\alpha$ -complex | 0.6097   |
|   | $\beta$ -complex  | 0.442  |
| $\text{C}_2\text{H}_2$<br>$\nu_2$       | pure              | inactive   |
|   | $\alpha$ -complex | 0.0014   |
|   | $\beta$ -complex  | 0.0018   |

Table 4.3: Relative intensities for acetylene  $\nu_3$  and nitrous oxide  $\nu_1 + \nu_3$ .

These relative intensity values have been used to convert the area under each absorption to relative number of moles. The mole fraction of each component in the cryofilm may then be calculated and plotted as a function of  $\text{N}_2\text{O}$  mole fraction in the gas mixture. Assuming the gas mixture concentration is preserved in the deposited solid, the stoichiometry of the  $\alpha$  binary phase is clearly shown to be 1:1 in Figure 4.9. The stoichiometry for the  $\beta$  phase is a little more ambiguous. However, it will be shown in Chapter 5 that the stoichiometry of  $\beta\text{-N}_2\text{O}\cdot\text{C}_2\text{H}_2$  is also 1:1.

In order to compare the systematic variation in the  $\text{N}_2\text{O}-\text{C}_2\text{H}_2$  system with that of the  $\text{CO}_2-\text{C}_2\text{H}_2$  system, a second Job-like plot was plotted combining the two binary phase contributions. The curves due to  $\text{N}_2\text{O}\cdot\text{C}_2\text{H}_2$  complexes decrease linearly over a greater portion of the graph than is observed with the  $\text{CO}_2\cdot\text{C}_2\text{H}_2$  complex. This would suggest that the  $\text{N}_2\text{O}-\text{C}_2\text{H}_2$  interaction competes more successfully with  $\text{CO}_2-\text{CO}_2$  and  $\text{C}_2\text{H}_2-\text{C}_2\text{H}_2$  interactions during the formation stages of the cryofilm. This will be discussed in greater detail in Chapter 5.

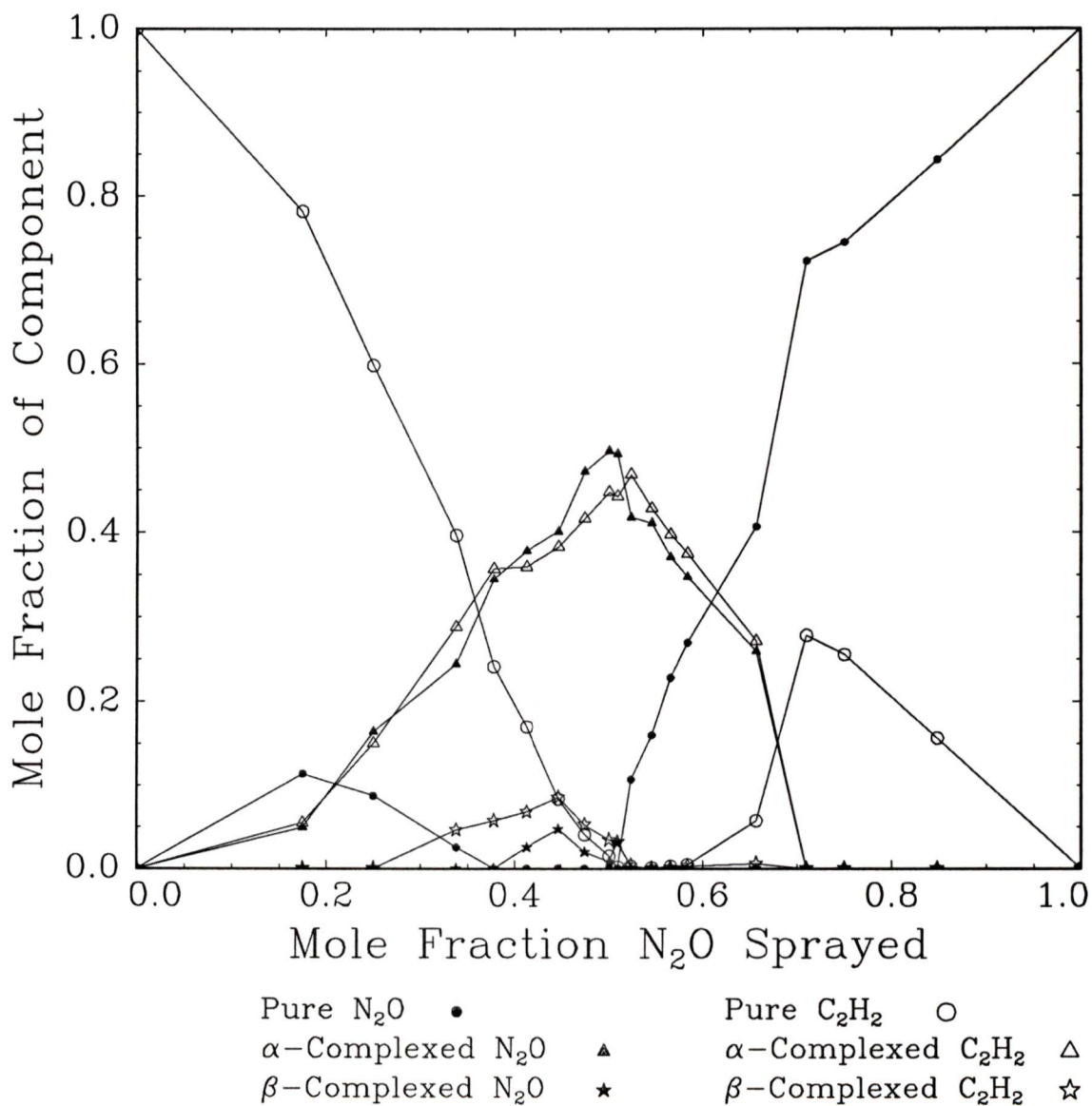


**Figure 4.9:** A systematic variation graph derived from the fitted areas under each curve. Relative band intensities given in Table 4.3 are used to convert area to mole fraction.

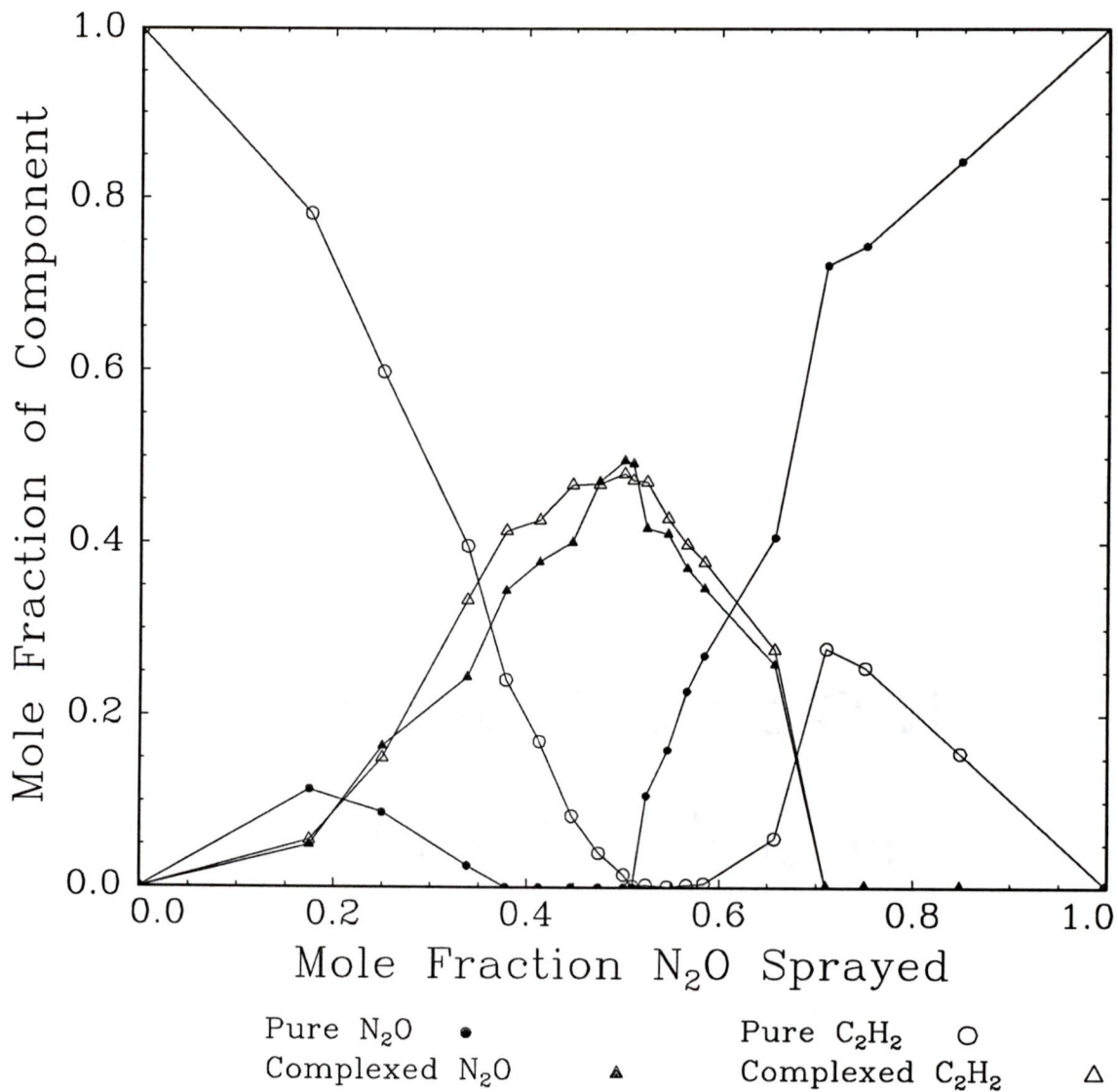


**Figure 4.10:** A systematic variation graph derived from the fitted areas under each curve. The mole fractions of both the  $\alpha$  and  $\beta$  phase are combined and represented as "Complexed" chromophore. Relative band intensities given in Table 4.3 are used to convert area to mole fraction.

## Chapter 5

# Growth and Stability of the Binary Phase

### 5.1 The Stability of the Binary Phases

Previously, the binary phases of  $\text{CO}_2\cdot\text{C}_2\text{H}_2$  and  $\text{N}_2\text{O}\cdot\text{C}_2\text{H}_2$  were prepared using the diffusive trapping technique [1]. The stability of these mixed phases with respect to the pure components could not be determined. In the diffusive trapping cell, cluster formation is a continuous flow process. Newly formed microcrystallites entering the optical path of the cell are immediately evacuated from the cell through an exit tube to a vacuum pump. Thus, the residence time of the newly formed cluster complexes was much too short to observe decomposition if the binary phases were metastable.

### 5.1.1 The $\text{CO}_2\cdot\text{C}_2\text{H}_2$ Phase

Results presented in Chapter 3, Section 3.2.1 show that formation of the binary phase was not possible under equilibrium conditions. This strongly suggests that the binary complex  $\text{CO}_2\cdot\text{C}_2\text{H}_2$  is not thermodynamically stable with respect to the pure phases. This may be confirmed by demonstrating the conversion of  $\text{CO}_2\cdot\text{C}_2\text{H}_2$  into pure solid  $\text{CO}_2$  and  $\text{C}_2\text{H}_2$ . Conversion of a binary complex cryofilm into pure carbon dioxide and acetylene did occur while holding the temperature of the window and sample constant at 90 K. FTIR spectra were recorded during this conversion.

Figure 5.1 shows spectra recorded in the  $\nu_1 + \nu_3$  region of  $\text{CO}_2$  at various times after the initial deposition of an equimolar gas mixture of  $\text{CO}_2$  and  $\text{C}_2\text{H}_2$ . The series clearly demonstrates the decomposition of the binary phase and the subsequent growth of the carbon dioxide solid phase. It is important to point out that the sample chamber was isolated from the vacuum pump prior to deposition and for the duration of the experiment, the purpose of which was to prevent sublimation of the sample. It can be shown that  $\text{CO}_2\cdot\text{C}_2\text{H}_2$  quantitatively decomposes to form solid carbon dioxide; the total amount of  $\text{CO}_2$  in the path of the infrared beam remained constant. From Table 3.3 the ratio of intensities  $\nu_1 + \nu_3$  binary :  $\nu_1 + \nu_3$  pure is 1.4:1. The area of the  $\text{CO}_2$   $\nu_1 + \nu_3$  binary peak at 0 minutes is 1.44 times larger than the area of the  $\text{CO}_2$   $\nu_1 + \nu_3$  pure peak at 300 minutes which is well within experimental error. Any difference between the two ratios could be accounted for by a small loss of  $\text{CO}_2$  due to sublimation.

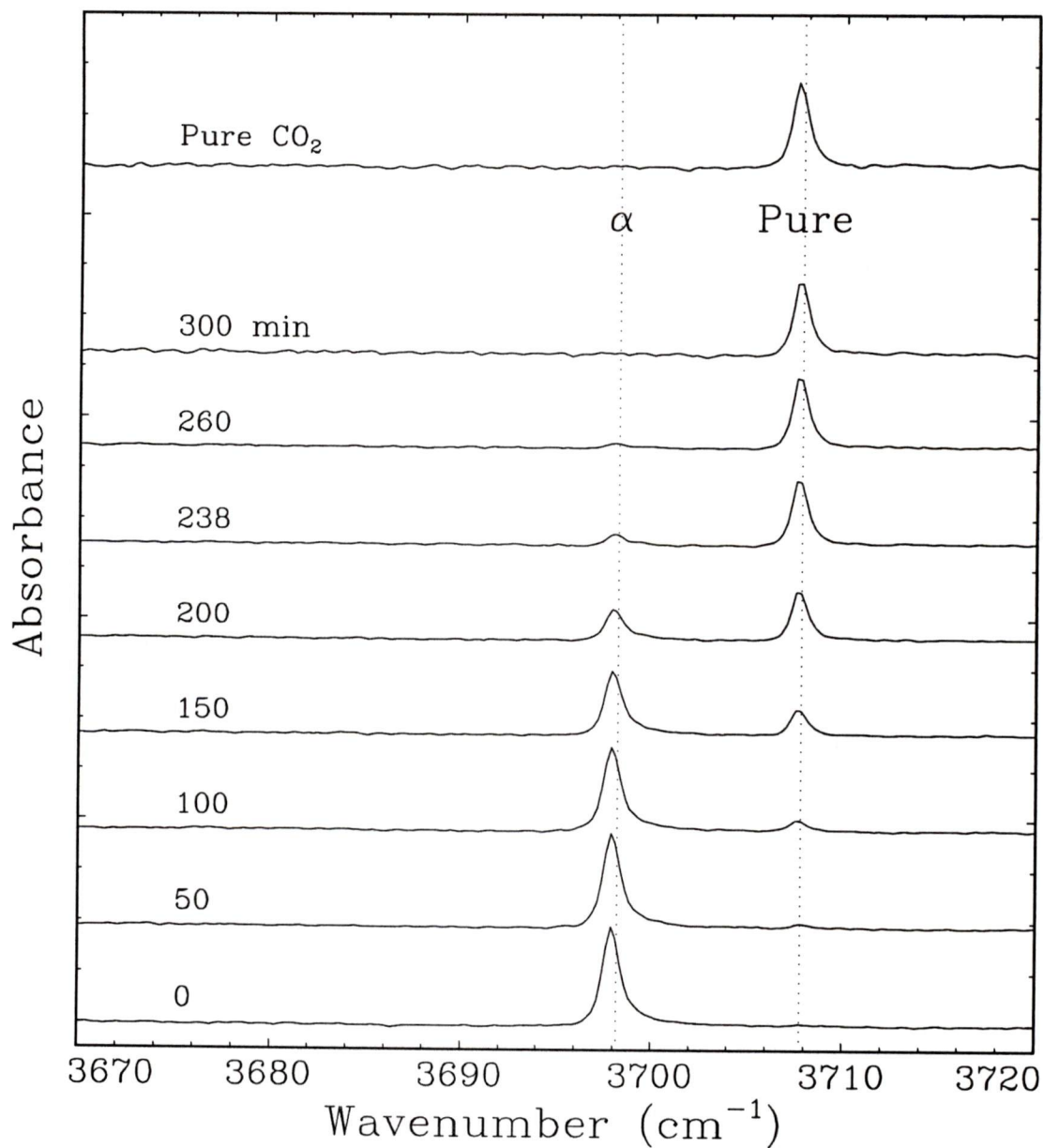


**Figure 5.1:** Spectra in the  $\nu_1 + \nu_3$  region of CO<sub>2</sub> recorded at various times (labelled in minutes) with the initial deposition from one 500 ms pulse of an equimolar gas mixture of CO<sub>2</sub> and C<sub>2</sub>H<sub>2</sub> taken as 0 minutes. The temperature was held constant at 90 K and the vacuum chamber was isolated from external pumps for the duration of the experiment.

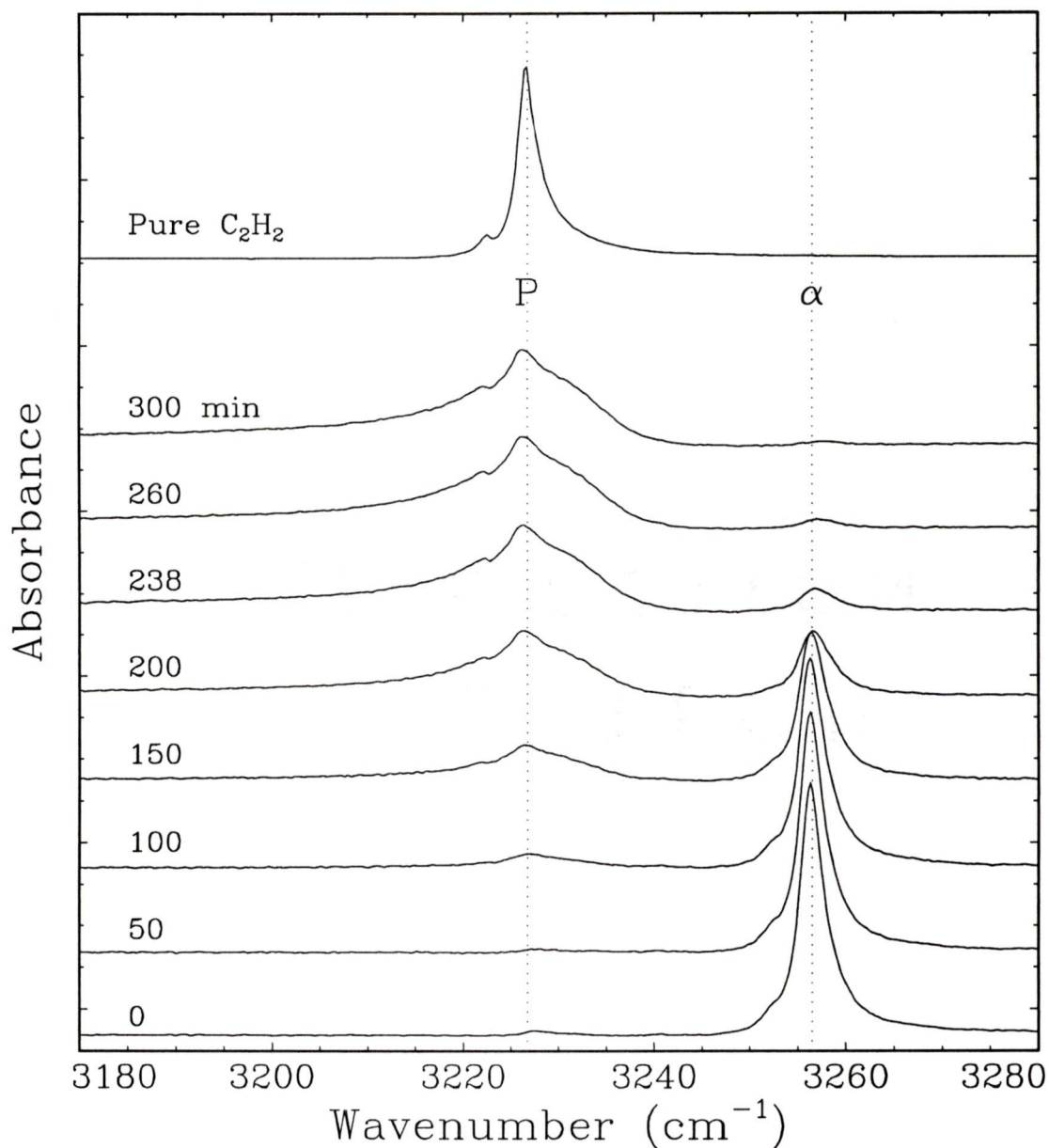


**Figure 5.2:** Spectra in the  $\nu_3$  region of  $\text{C}_2\text{H}_2$  recorded at various times (labelled in minutes) with the initial deposition from one 500 ms pulse of an equimolar gas mixture of  $\text{CO}_2$  and  $\text{C}_2\text{H}_2$  taken as 0 minutes. The temperature was held constant at 90 K and the vacuum chamber was isolated from external pumps for the duration of the experiment.

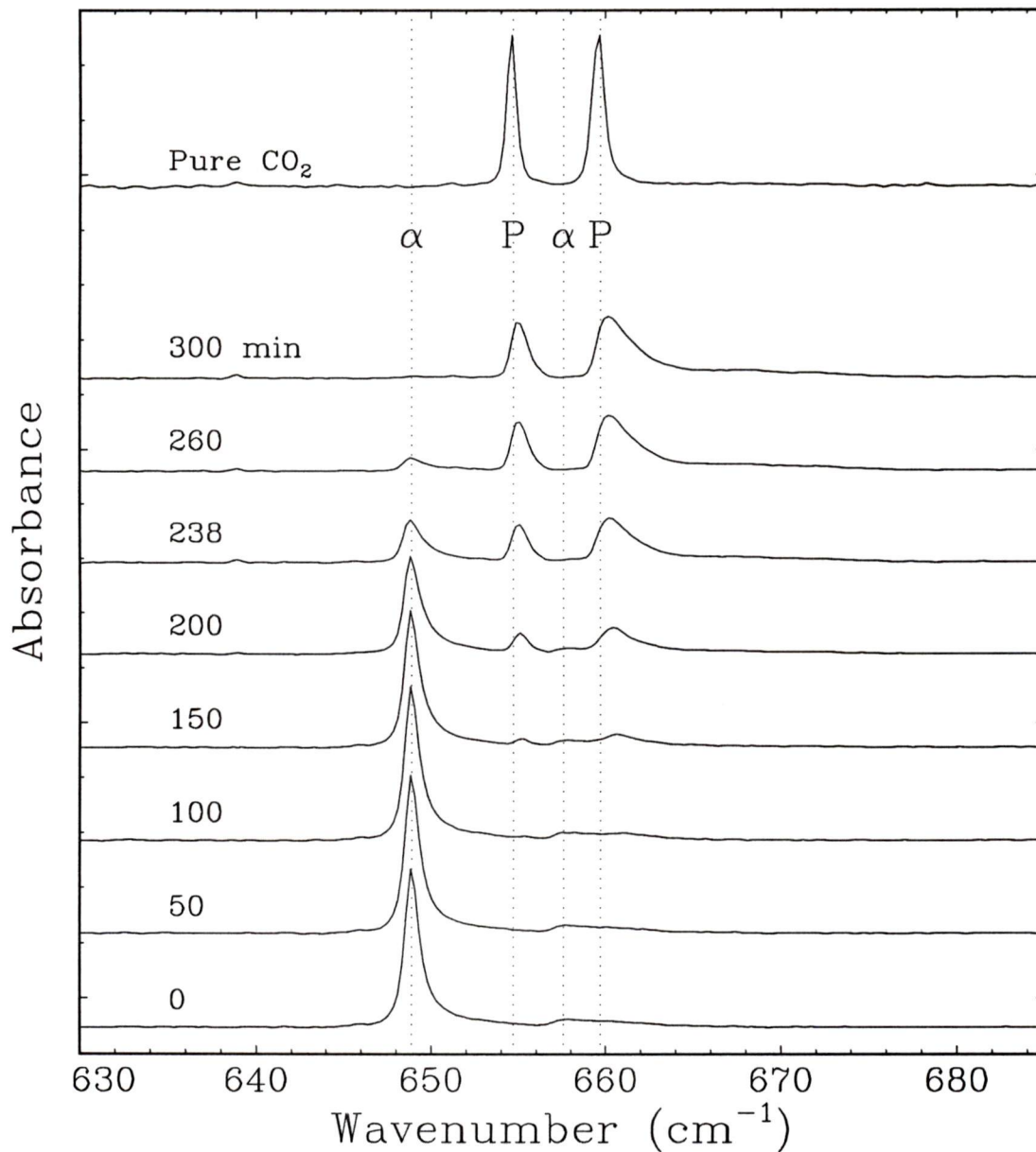


**Figure 5.3:** Spectra in the  $\nu_2$  region of CO<sub>2</sub> recorded at various times (labelled in minutes) with the initial deposition from one 500 ms pulse of an equimolar gas mixture of CO<sub>2</sub> and C<sub>2</sub>H<sub>2</sub> taken as 0 minutes. The temperature was held constant at 90 K and the vacuum chamber was isolated from external pumps for the duration of the experiment. Absorptions due to CO<sub>2</sub> in the binary phase are labelled as  $\alpha$ . Absorptions due to CO<sub>2</sub> in the pure phase are labelled as  $P$ .

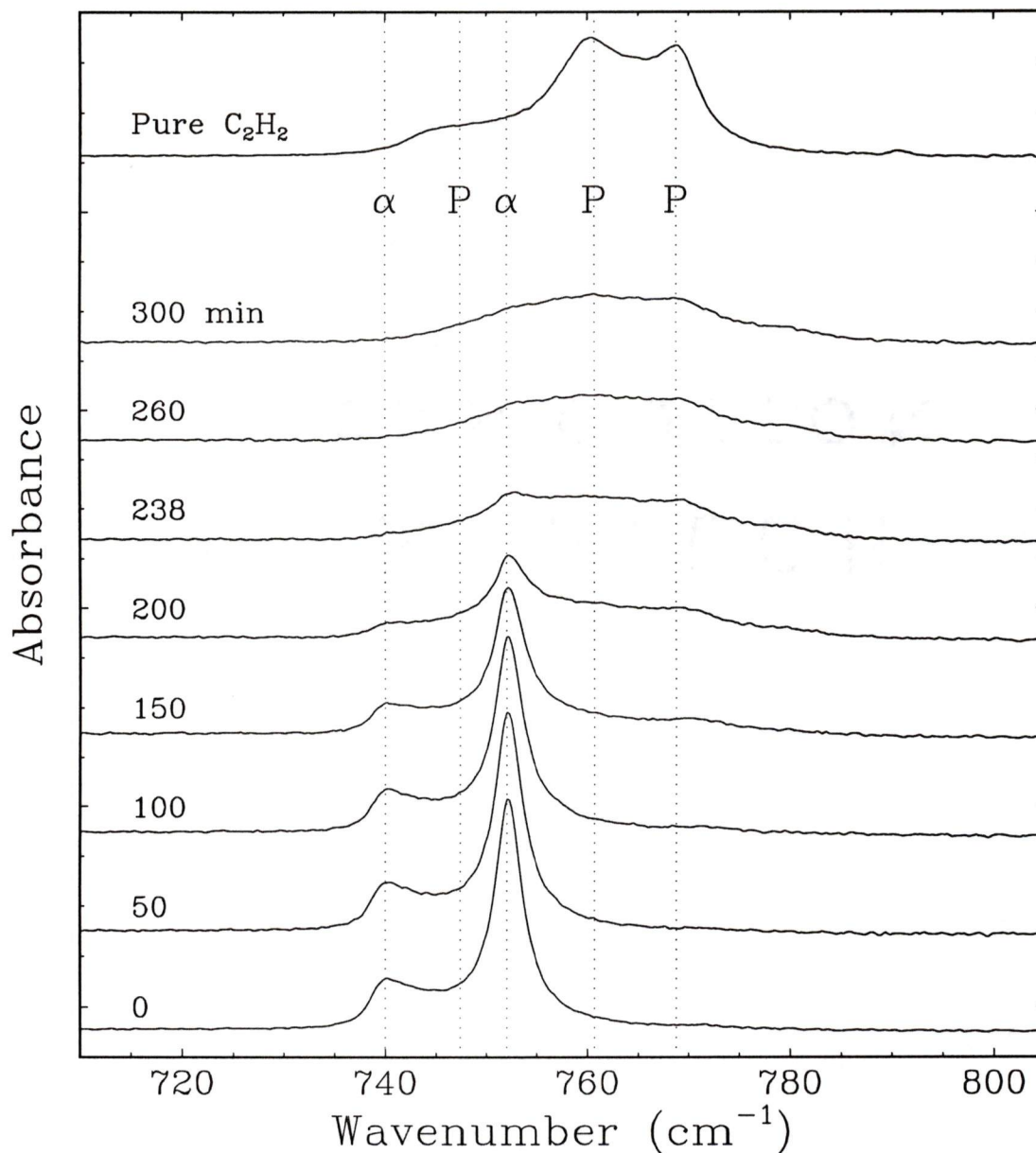


**Figure 5.4:** Spectra in the  $\nu_5$  region of  $\text{C}_2\text{H}_2$  recorded at various times (labelled in minutes) with the initial deposition from one 500 ms pulse of an equimolar gas mixture of  $\text{CO}_2$  and  $\text{C}_2\text{H}_2$  taken as 0 minutes. The temperature was held constant at 90 K and the vacuum chamber was isolated from external pumps for the duration of the experiment.

The same quantitative decomposition appears to occur in the  $\nu_3$  region of acetylene (see Figure 5.2). However, due to the broadness of the  $\nu_3$  pure band of  $C_2H_2$  upon conversion, the areas could not be measured as accurately as the areas under the  $\nu_1 + \nu_3$  pure  $CO_2$  band. The increased broadness and asymmetry of the  $C_2H_2$   $\nu_3$  band located at  $3226\text{ cm}^{-1}$  indicates that the pure phase being formed lacks the crystallinity of the pure acetylene sample formed previously (see Figure 3.6).

The fractional conversion of  $CO_2 \cdot C_2H_2$  into its pure components as a function of time is shown in Figure 5.5. Raw data is given in Table 5.1. Each point is determined from the area under the binary phase absorptions shown in Figures 5.1 and 5.2 (labelled as  $\alpha$ ). The areas under the absorption bands due to  $CO_2$  and to  $C_2H_2$  in the binary phase are normalized with the relative intensity ratios (Table 3.3) and then averaged. The error bars represent the accuracy of the curve fitting and the time taken to record one spectrum. Because the decomposition was slow, each spectrum was generated from 64 scans (3 minutes) in order to obtain a better signal-to-noise ratio. The solid line is a best fit of the expression

$$\chi = 1 - \exp(-(b \times t)^n) \quad (5.1)$$

where  $\chi$  is the fraction of volume that has changed. The term  $b$  is a measure of the rapidity of the transformation. The value  $n$  is a potential source of information on the mechanism of the transformations. Best fit values were  $b=0.3149 \pm 0.0022$  and  $n=3.29 \pm 0.12$ .

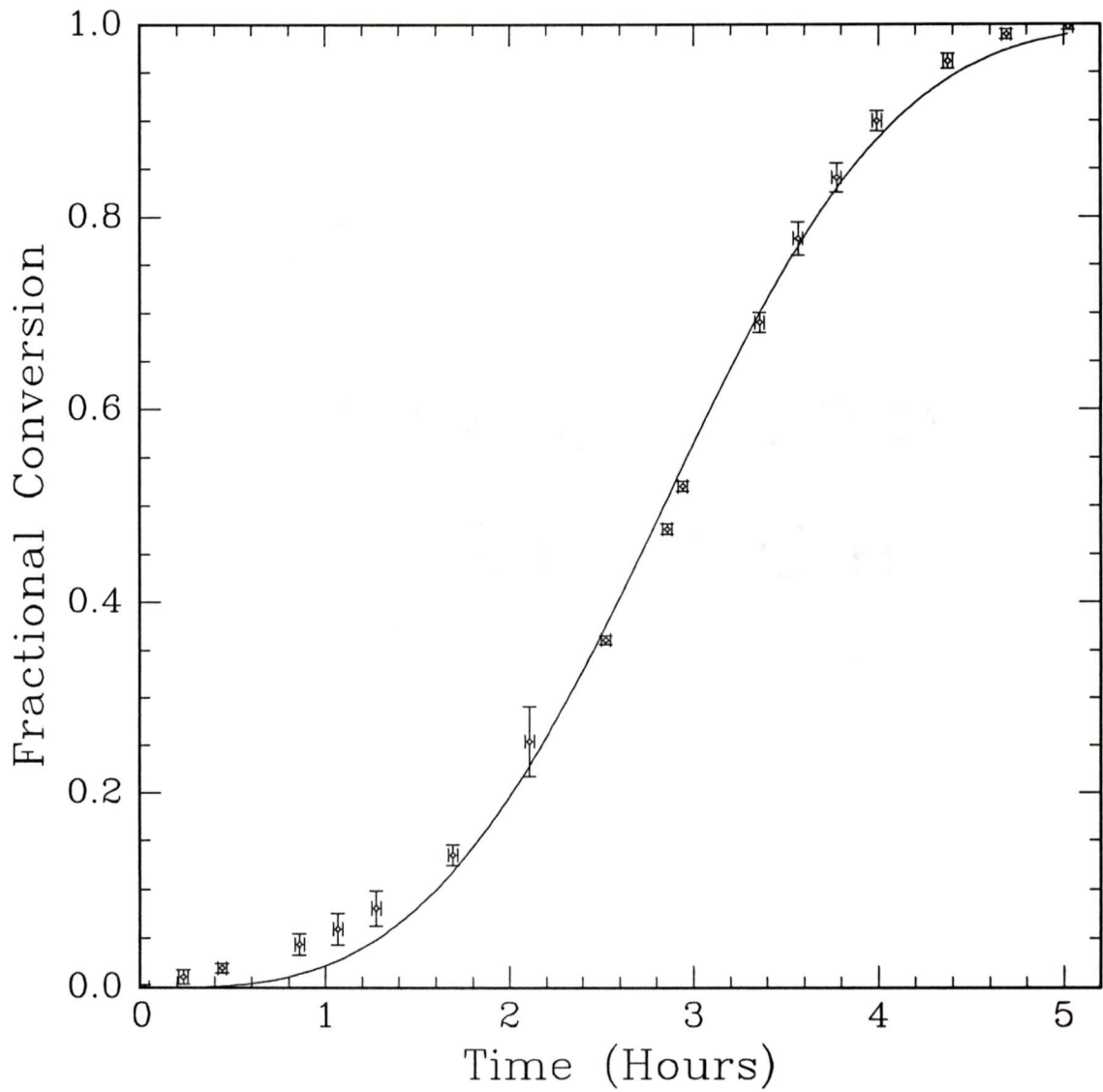


**Figure 5.5:** Conversion of the binary carbon dioxide-acetylene phase into pure components. The solid line represents a fit of the data in Table 5.1 to the Avrami equation, Equation 5.1.

| Time<br>(Hour)<br>$\pm 0.025$ | Fractional<br>Conversion<br>$\chi$ |              |
|-------------------------------|------------------------------------|--------------|
| 0                             | 0                                  |              |
| 0.233                         | 0.011                              | $\pm 0.007$  |
| 0.442                         | 0.020                              | $\pm 0.005$  |
| 0.858                         | 0.044                              | $\pm 0.011$  |
| 1.067                         | 0.059                              | $\pm 0.016$  |
| 1.275                         | 0.081                              | $\pm 0.018$  |
| 1.692                         | 0.135                              | $\pm 0.011$  |
| 2.108                         | 0.25                               | $\pm 0.04$   |
| 2.525                         | 0.361                              | $\pm 0.005$  |
| 2.858                         | 0.476                              | $\pm 0.005$  |
| 2.942                         | 0.520                              | $\pm 0.005$  |
| 3.358                         | 0.690                              | $\pm 0.010$  |
| 3.567                         | 0.777                              | $\pm 0.018$  |
| 3.775                         | 0.841                              | $\pm 0.015$  |
| 3.992                         | 0.900                              | $\pm 0.010$  |
| 4.375                         | 0.962                              | $\pm 0.008$  |
| 4.692                         | 0.989                              | $\pm 0.005$  |
| 5.025                         | 0.9972                             | $\pm 0.0028$ |

Table 5.1: Conversion of  $\text{CO}_2 \cdot \text{C}_2\text{H}_2$  into pure components. Fractional conversion is the ratio of the amount of substance converted to the initial amount. The amount of  $\text{CO}_2 \cdot \text{C}_2\text{H}_2$  converted is determined from the area under the bands due to complex in Figures 5.1 and 5.2.

Equation 5.1 is frequently referred to as the Avrami [31] equation. It adequately describes the kinetics of a three dimensional growth of spherical nuclei of a second phase inside the matrix of the first phase. The lower limit of  $n = 3$  for spherical growth can be described by phase transformation from predetermined nuclei with no subsequent nucleation (athermal). A value of  $n=4$  corresponds to a time-independent rate of nucleation ( $R$ ) which is referred to as thermal crystallization. The experimental value of  $n = 3.29$  lies between 3 and 4 where it may be suggested that the nuclei are hemispherical, appearing at a time-independent rate perhaps at the crystal-window boundary, thus being truncated. However, the exponent  $n$  is also influenced by the shape of the growing particles. Table 5.2 shows a collection of some of the possible values of  $n$  for the Avrami equation in various cases. For instance, for spherical nuclei where  $R$  decreases with time (exhaustion) the order would initial be 4 and decrease as the conversion proceeded.

The fit to Equation 5.1 is not a good fit at all. It appears that the value  $n$  is not constant. A plot of  $\log(-\ln(1 - \chi))$  versus  $\log(t)$  is typically used in Avrami analyses. The value  $n$  is determined from the slope. Manipulation of Equation 5.1 in this manner yields a linear equation of the form

$$\log(-\ln(1 - \chi)) = n \log b + n \log t \quad (5.2)$$

in which it is assumed that  $b$  is constant. In this case  $n$ , from the slope between consecutive points in Figure 5.6(a), is found to increase with time (see Figure 5.6(b)).

Initially  $n$  is close to 1.3. It reaches approximately 4.2 at 3 hours and begins to drop near the end.

Because of this change in  $n$ , a better fit to the data may be obtained by allowing the exponent to vary linearly with time (see Figure 5.7). This modified Avrami function is given in Equation 5.3.

$$\chi = \frac{5-t}{5} [1 - \exp(-(b \times t)^m)] + \frac{t}{5} [1 - \exp(-(c \times t)^n)] \quad (5.3)$$

Best fit values were  $b=0.297 \pm 0.020$  and  $m=2.25 \pm 0.17$ ,  $c=0.309 \pm 0.003$  and  $n=4.29 \pm 0.16$ . Equation 5.3 fits the conversion data much better than Equation 5.1. Note that the pre-exponential factors appear to be constant while the order changes from 2.25 to 4.29. Spherical growth of nuclei as a model only allows for a constant value of  $n$  or a decreasing value in the case of exhaustion, so it is very unlikely that the geometry of the growing nuclei is such.

A model which *does* allow  $n$  to increase is that of branching fibrillar growth [32]. In this model, fibers of cross section  $d^2\pi/4$  grow for  $l$  cm until they branch into two separate fibers with the same cross section as the parent. Both daughter fibers branch again after  $l$  cm of growth. This growth can be described by the following equation

$$\chi = 1 - \exp\left(-\frac{\pi N d^2 l (2^{\frac{t}{l}} - 1)}{(2 \ln 2)}\right) \quad (5.4)$$

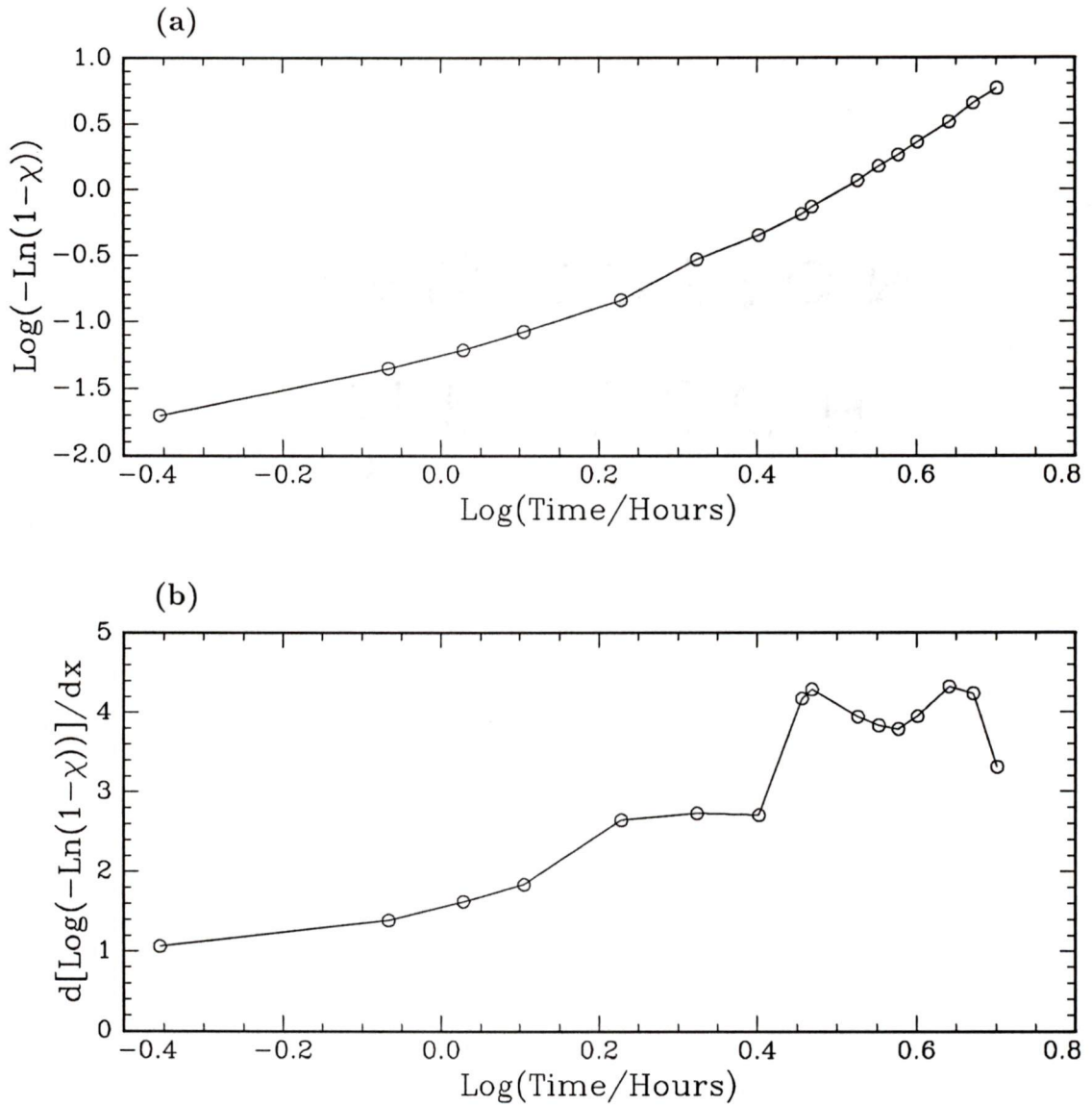


**Figure 5.6:** Determination of the value 'n' by manipulation of the Avrami equation using data from Table 5.1. 'χ' is the fractional conversion of the binary carbon dioxide-acetylene phase to pure components.

(a) Plot of Equation 5.2 using data from Table 5.1.

(b) First derivative plot of graph (a).

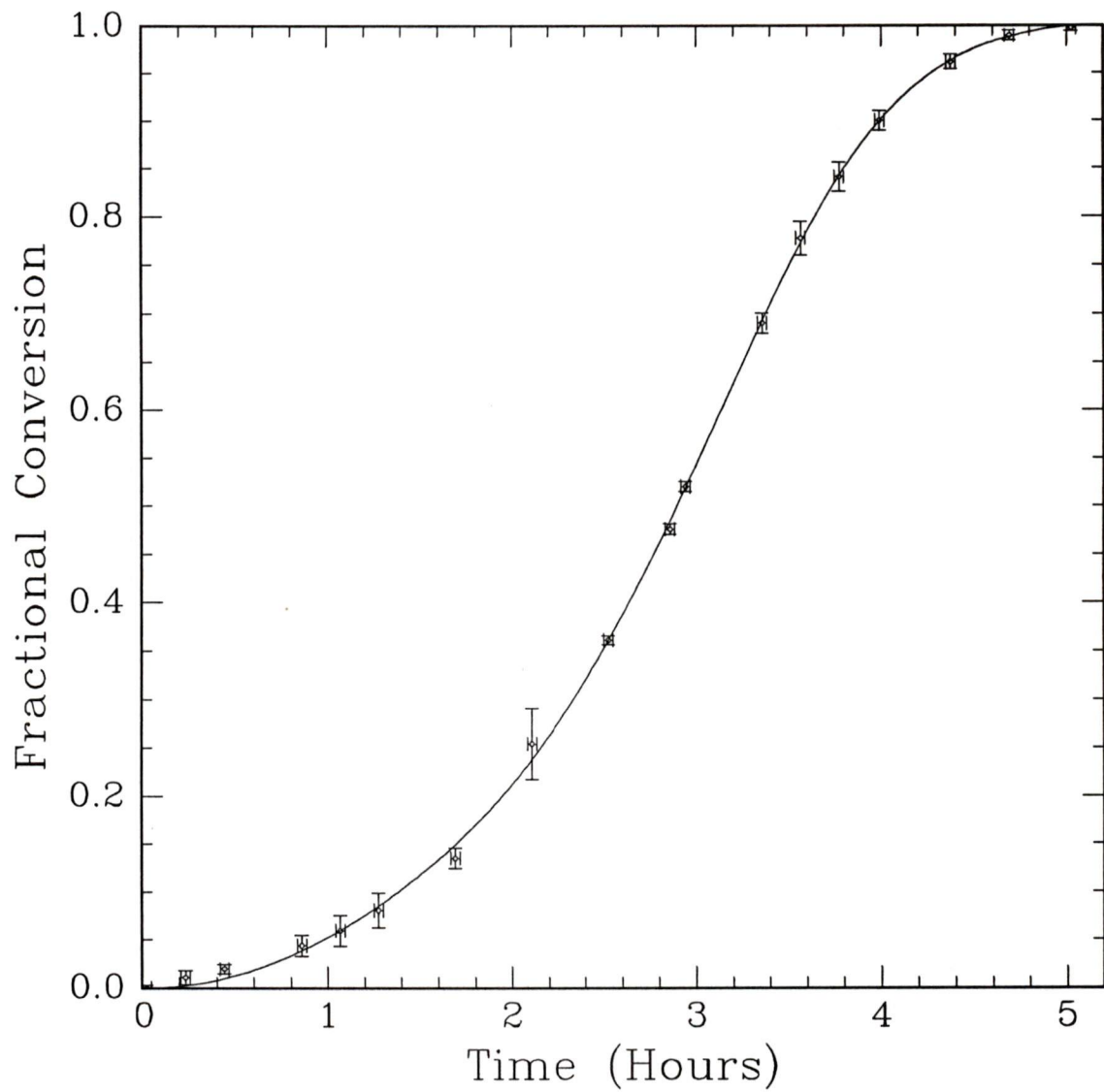


**Figure 5.7:** Conversion of the binary carbon dioxide-acetylene phase to pure components. The solid line represents a fit of the data in Table 5.1 to the modified Avrami equation, Equation 5.3.

which may be rewritten as

$$1 - \chi = \exp \left( -A \left[ Bt + \frac{(Bt)^2}{2!} + \frac{(Bt)^3}{3!} + \dots \right] \right) \quad (5.5)$$

using a power series expansion.  $A = \pi N d^2 l / (2 \ln 2)$  and  $B = (v \ln 2) / l$ . Taking the natural log of  $(1 - \chi)$  in Equation 5.5 leaves a simple polynomial on the right side. The resulting plot may be fit to successively higher order polynomials until there is no further improvement in the fit. This occurs at an order of five, in close agreement with the results shown in Figure 5.6(b). Figure 5.8 shows a natural log plot of the decomposition data. The solid line is a fit to the data using the following equation.

$$f(t) = -A \left[ Bt + \frac{(Bt)^2}{2!} + \frac{(Bt)^3}{3!} + \frac{(Bt)^4}{4!} + \frac{(Bt)^5}{5!} \right] \quad (5.6)$$

Best fit values were  $A = 0.0087 \pm 0.0013$  and  $B = 0.0277 \text{ min}^{-1} \pm 0.0011 \text{ min}^{-1}$

Blocking of fibers by other growing sheafs of fibers could result in a reduction of the exponent of  $t$  near the final stages of growth.

The wide variety of possible exponents for the Avrami equation show that it is not possible to conclusively determine the nucleation and growth behaviour of the phase transformation from the time-dependence data represented in Figure 5.5. However, it appears that an Avrami analysis has ruled out the possibility of two-dimensional and spherical growth, amongst others, of pure phase nuclei. Perhaps the best model describing the conversion of the binary phase into its pure components

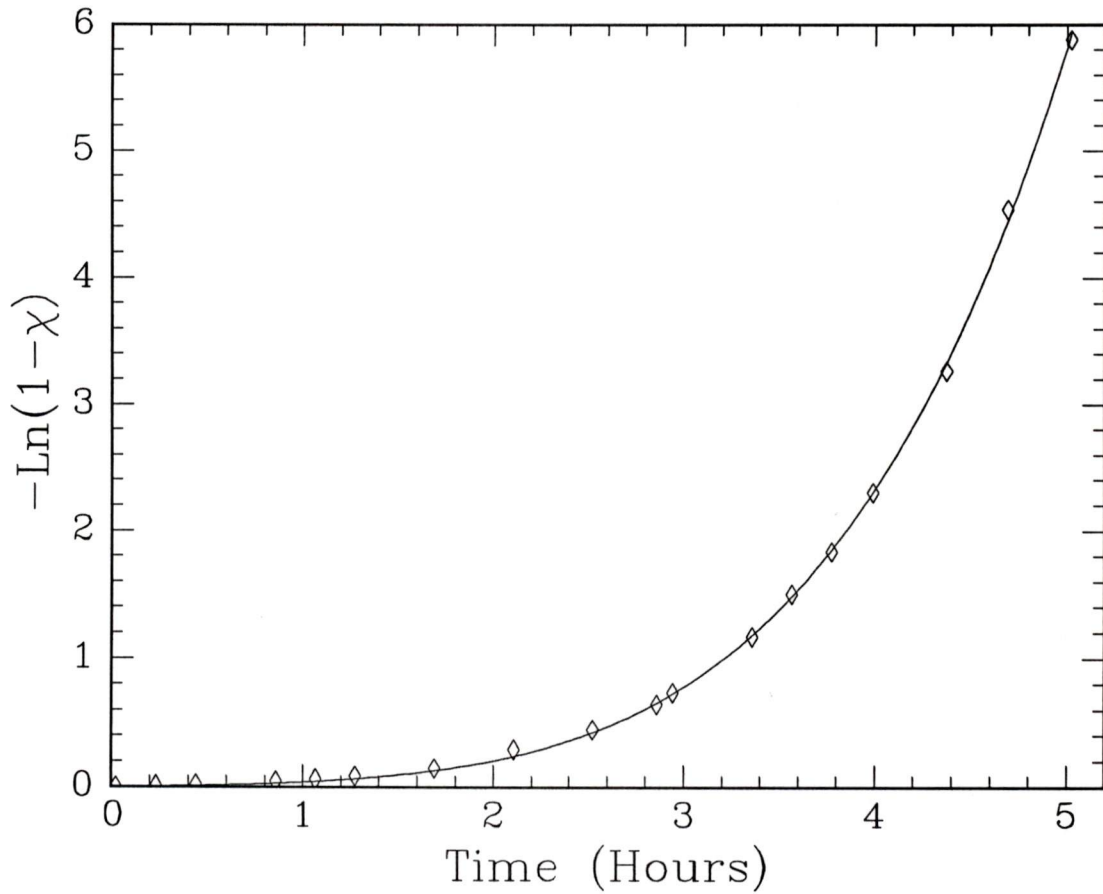


**Figure 5.8:** Natural logarithm plot using data from Figure 5.1. ' $\chi$ ' is the fractional conversion of the binary carbon dioxide-acetylene phase to pure components. The solid line represents a fit of the data in Table 5.1 to Equation 5.6 using a fifth order polynomial.

is that of growing sheafs of fibers which branch after a certain period of growth. If this is the correct geometry of growth then nuclei appear continuously throughout the conversion at a constant rate since initially the value of  $n$  is approximately 2 and the pre-exponential factor  $b$  remains constant. An upper bound of  $n \approx 4$  from the fit to Equation 5.3 and from the slope of the last nine points in Figure 5.6(a) indicates that the branching is efficient enough that the geometry approaches that of growing spheres in the latter stages. An inherent problem with this model is the fact that it was designed to model the growth of macromolecule solids from the liquid phase. In this work, the initial phase as well as the final phase are solid. If there is no intermediate vapor or liquid phase, one must consider that the molecular transport processes occur through the solid phase.

Presently, other models such as evaporative processes are under consideration. However, the area under the pure  $\nu_1 + \nu_3$  band of  $\text{CO}_2$  at 300 minutes is 54% of the area under the same peak observed in a pure  $\text{CO}_2$  cryofilm produced under the same conditions as the binary cryofilm (time=0 minutes). As  $\text{CO}_2 \cdot \text{C}_2\text{H}_2$  is 1:1 stoichiometry, a value of 50% is expected. Further evidence that the number of  $\text{CO}_2$  molecules in the field of view remains relatively constant can be found in an overlay plot in the  $\nu_2$  region of  $\text{CO}_2$ . The same spectra from Figure 5.3 are shown overlain in Figure 5.9. The presence of three isosbestic points at 654.2, 656.8 and 659.1  $\text{cm}^{-1}$  is clearly seen. The presence of isosbestic points does not necessarily imply that there are only two chromophores present, but we already know this to be true from inspection of the

rest of the spectra available. The presence of these remarkable isosbestic points does indicate strongly that there is no significant net change in the number carbon dioxide molecules. The same can be said for acetylene. Figure 5.10 shows an isosbestic point at  $755.8 \text{ cm}^{-1}$  in the  $\nu_5$  region of  $\text{C}_2\text{H}_2$  which also indicates that the number of acetylene molecules in the field of view remains relatively constant. It is most likely, then, that the decomposition of  $\text{CO}_2\cdot\text{C}_2\text{H}_2$  occurs through the solid phase.

The results described above do give further confirmation to the 1:1 stoichiometry of  $\text{CO}_2\cdot\text{C}_2\text{H}_2$  as well as the relative intensity ratios that were determined in Chapter 3. They also show the metastability of  $\text{CO}_2\cdot\text{C}_2\text{H}_2$  with respect to the pure phases. Any speculation on the process of conversion of  $\text{CO}_2\cdot\text{C}_2\text{H}_2$  will be reserved for the Discussion section later in this chapter.

### 5.1.2 The $\text{N}_2\text{O}\cdot\text{C}_2\text{H}_2$ Phase

A similar kinetic study was conducted for  $\text{N}_2\text{O}\cdot\text{C}_2\text{H}_2$ . The results were surprisingly different than those for  $\text{CO}_2\cdot\text{C}_2\text{H}_2$ . Using the same approach as we did for  $\text{CO}_2\cdot\text{C}_2\text{H}_2$ , an  $\alpha\text{-N}_2\text{O}\cdot\text{C}_2\text{H}_2$  cryofilm was prepared on the ZnSe window. The window was held at 90 K. After five hours at 90 K, no appreciable changes were noted. There was no growth of either pure  $\text{N}_2\text{O}$  or pure  $\text{C}_2\text{H}_2$  and only minimal loss of the  $\alpha$  phase of  $\text{N}_2\text{O}\cdot\text{C}_2\text{H}_2$  due to sublimation. The spectra also showed a gradual contamination of the sample with atmospheric water.

Since little conversion of  $\alpha\text{-N}_2\text{O}\cdot\text{C}_2\text{H}_2$  was observed at 90 K, the temperature

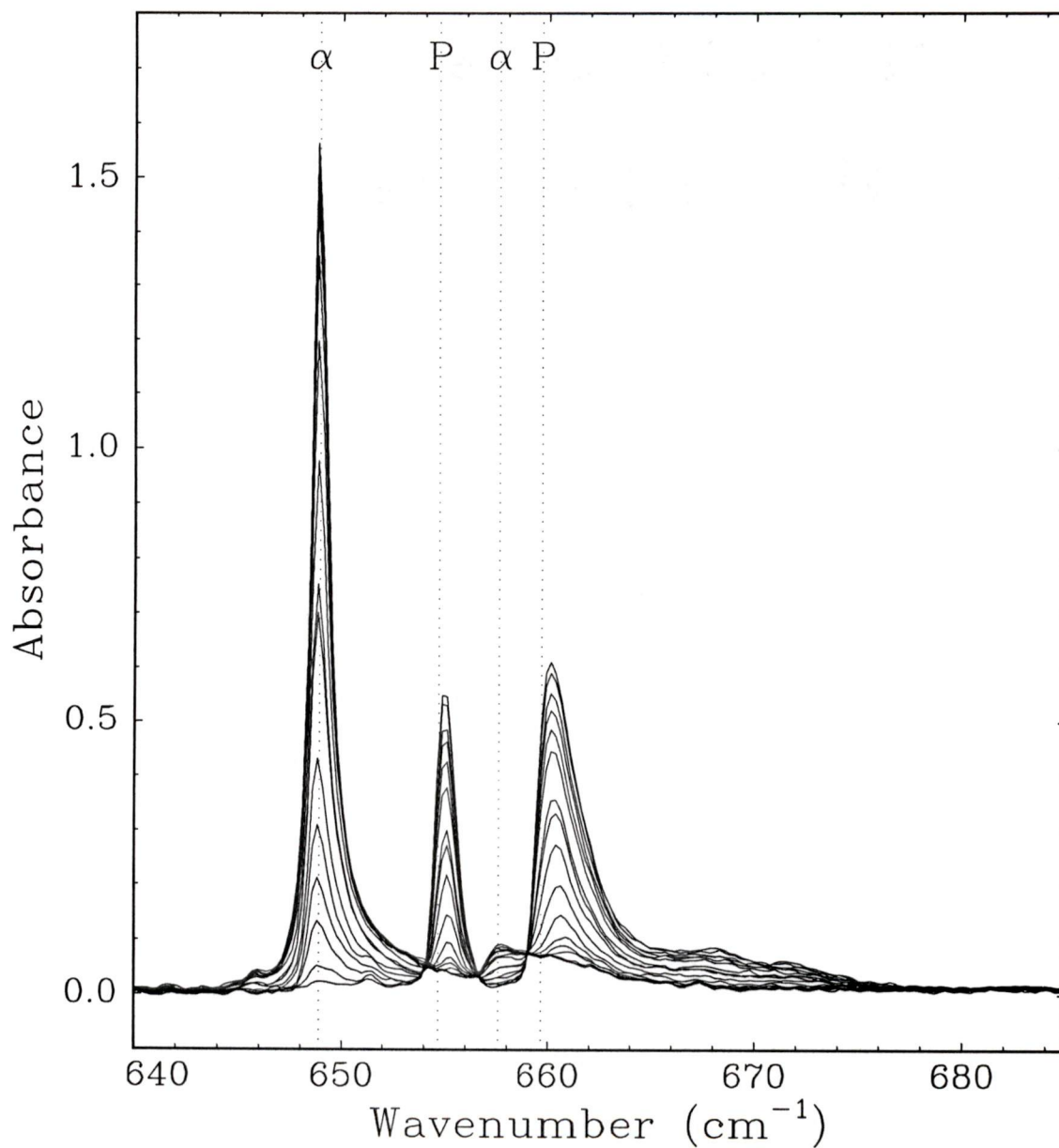


**Figure 5.9:** Spectra in the  $\nu_2$  region of  $\text{CO}_2$  recorded at various times during decomposition of  $\text{CO}_2 \cdot \text{C}_2\text{H}_2$ . The initial deposition is from one 500 ms pulse of an equimolar gas mixture of  $\text{CO}_2$  and  $\text{C}_2\text{H}_2$ . The temperature was held constant at 90 K and the vacuum chamber was isolated from external pumps for the duration of the experiment.

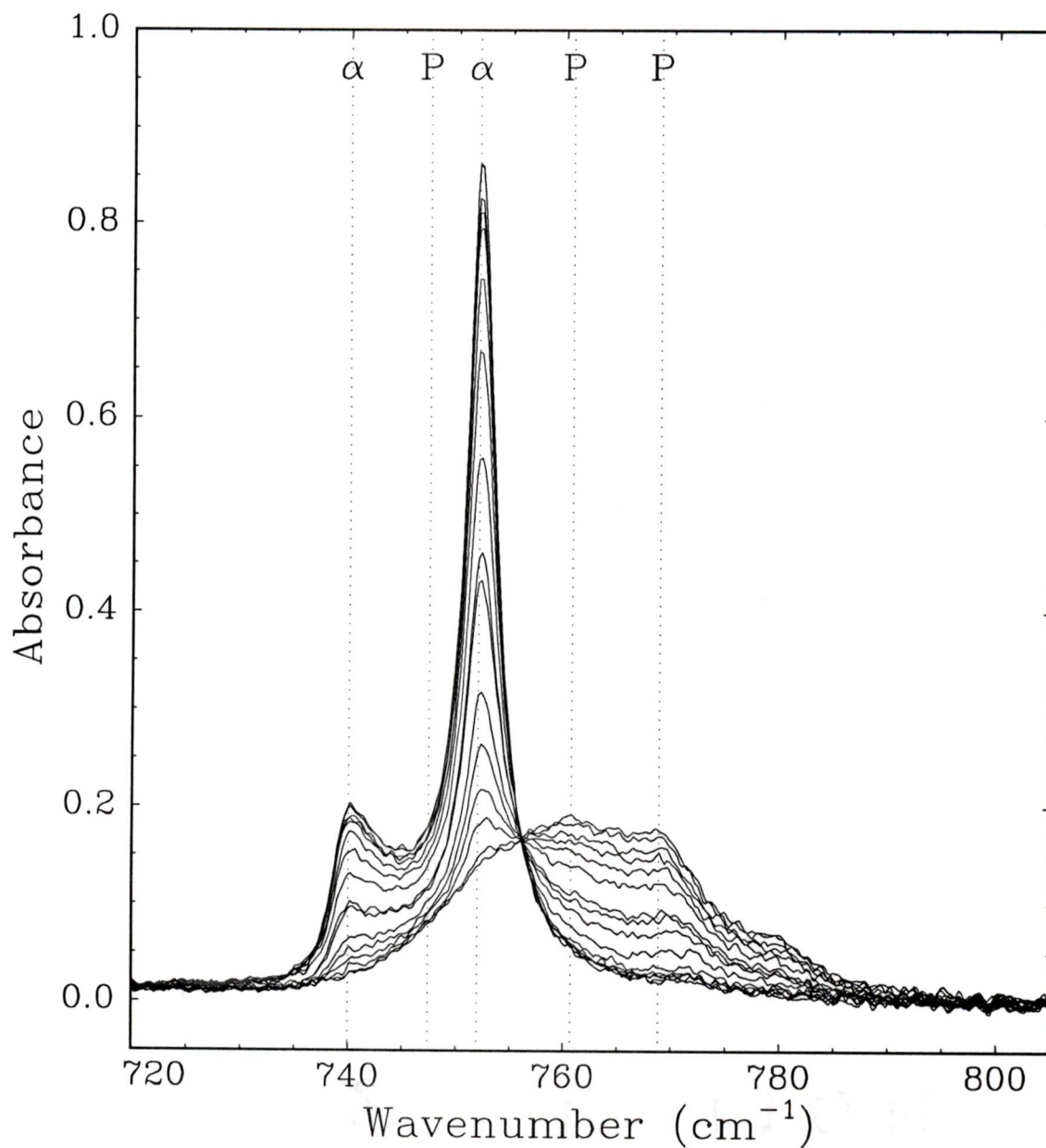


**Figure 5.10:** Spectra in the  $\nu_5$  region of  $C_2H_2$  recorded at various times (labelled in minutes) with the initial deposition from one 500 ms pulse of an equimolar gas mixture of  $CO_2$  and  $C_2H_2$  taken as 0 minutes. The temperature was held constant at 90 K and the vacuum chamber was isolated from external pumps for the duration of the experiment.

of the window was gradually raised. Figure 5.11 shows  $\alpha\text{-N}_2\text{O}\cdot\text{C}_2\text{H}_2$  undergoing a phase transition into  $\beta\text{-N}_2\text{O}\cdot\text{C}_2\text{H}_2$  during this period. Note that absorptions due to acetylene in the pure phase are absent. Continued warming of the sample above 101 K resulted in a rapid increase in the sublimation rate of the cryofilm. That acetylene is more volatile than nitrous oxide at this temperature is seen in the same series featuring the  $\nu_1 + \nu_3$  combination band of  $\text{N}_2\text{O}$  (see Figure 5.12). A band due to  $\text{N}_2\text{O}$  in the pure phase begins to appear at 104 K due to excess loss of acetylene. This series gives evidence that the  $\beta$  binary phase is more thermodynamically stable than the  $\alpha$  binary phase and possibly more stable than the separate pure phases of  $\text{N}_2\text{O}$  and  $\text{C}_2\text{H}_2$ .

With respect to the  $\text{N}_2\text{O}\text{-C}_2\text{H}_2$  series discussed in Section 4.3,  $\beta\text{-N}_2\text{O}\cdot\text{C}_2\text{H}_2$  was present only in small amounts. Therefore, the relative intensities of the beta phase absorption could not be determined. For this reason, the relative intensity ratios for the  $\beta$  phase were determined from the areas under the absorption bands in Figures 5.11 and 5.12 with the assumption that the conversion is quantitative. This should be a good assumption since neither pure  $\text{N}_2\text{O}$  nor  $\text{C}_2\text{H}_2$  are formed.

Similar results, showing the thermodynamic stability of the  $\beta$  phase over the  $\alpha$  phase are represented in Figure 5.13. All cryofilm spectra shown up to this point are taken from solids deposited from a single 500 ms pulse of gas. This was determined to be the optimal setting for preparing bulk  $\alpha\text{-CO}_2\cdot\text{C}_2\text{H}_2$  and  $\alpha\text{-N}_2\text{O}\cdot\text{C}_2\text{H}_2$ . At the onset of the study it was felt that the most crystalline solid could be grown from

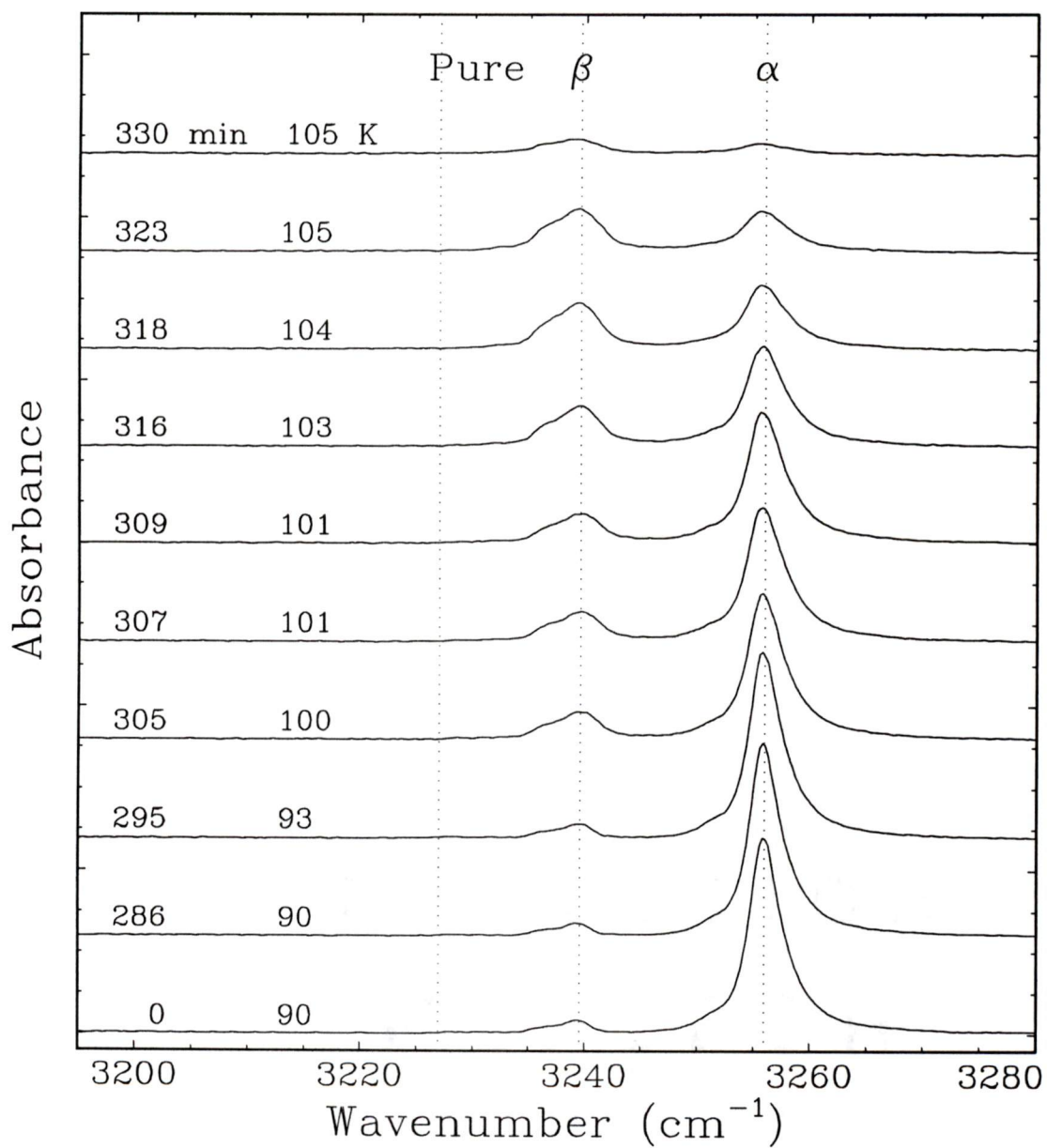


**Figure 5.11:** Spectra of the  $\nu_3$  fundamental band of  $C_2H_2$ . Conversion of  $\alpha-N_2O \cdot C_2H_2$  into  $\beta-N_2O \cdot C_2H_2$ .

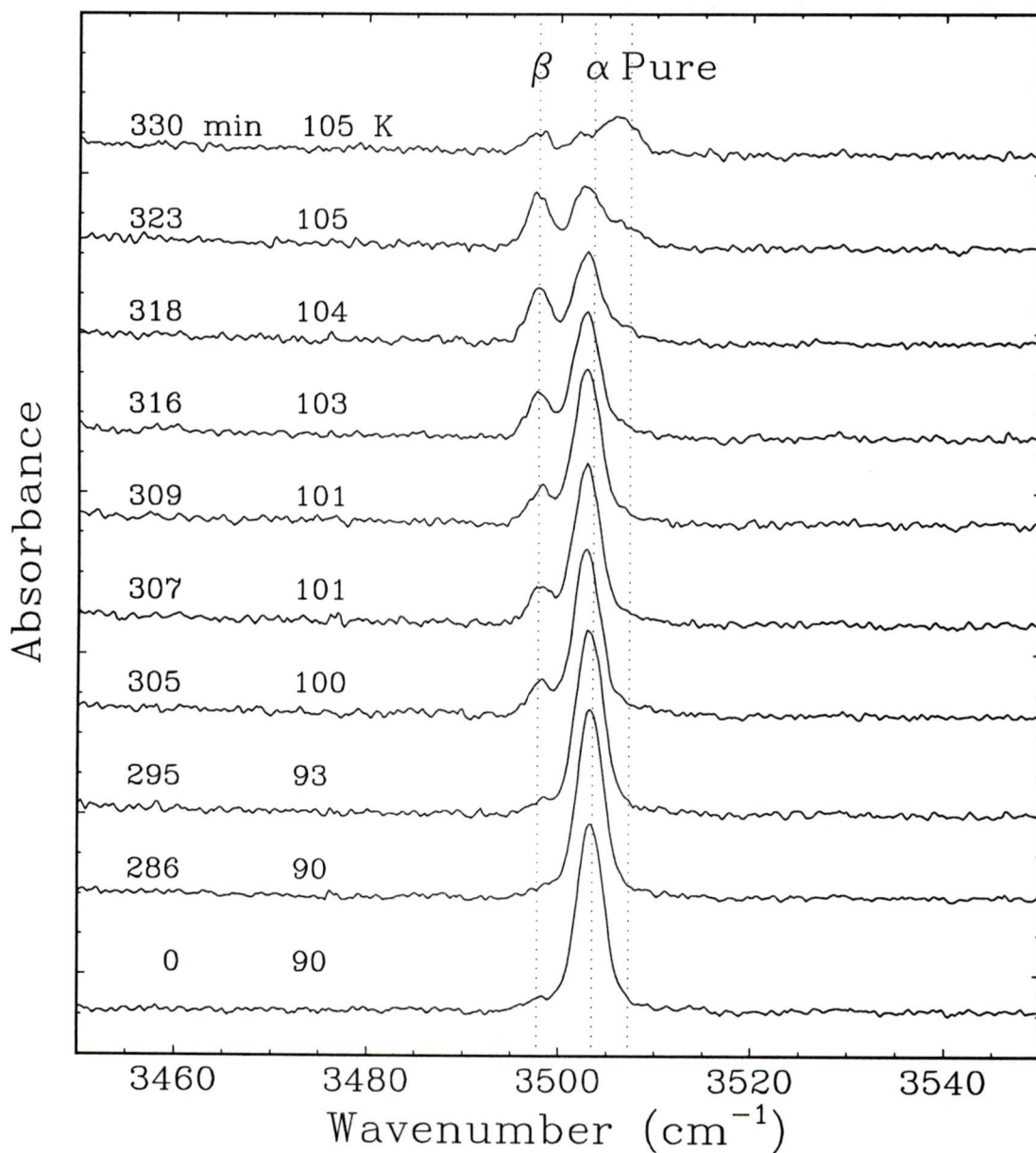


**Figure 5.12:** Spectra of the  $\nu_1 + \nu_3$  combination band of  $\text{N}_2\text{O}$ . Conversion of  $\alpha\text{-N}_2\text{O}\cdot\text{C}_2\text{H}_2$  into  $\beta\text{-N}_2\text{O}\cdot\text{C}_2\text{H}_2$ .

many short pulses of gas deposited over a long period of time [25]. This approach favoured formation of pure phases over the  $\alpha$  phase. As seen in Figure 5.13 it also favours growth of the  $\beta$  phase over the  $\alpha$  phase of  $\text{N}_2\text{O}\cdot\text{C}_2\text{H}_2$ . The series shows the spectra of a 50% mixture of  $\text{N}_2\text{O}$  and  $\text{C}_2\text{H}_2$  taken after consecutive 100 ms pulses. There was a 4 minute interval between each pulse and the window was held at 90 K for the entire experiment.

These results show that  $\beta\text{-N}_2\text{O}\cdot\text{C}_2\text{H}_2$  is more stable than  $\alpha\text{-N}_2\text{O}\cdot\text{C}_2\text{H}_2$ . They also strongly suggest that  $\beta\text{-N}_2\text{O}\cdot\text{C}_2\text{H}_2$  is thermodynamically stable with respect to the pure phases. The stoichiometry of the  $\beta$  phase appears to be the same as the  $\alpha$  phase since conversion of the  $\alpha$  phase into the  $\beta$  phase did not result in growth of any pure phase. The stoichiometry of  $\beta\text{-N}_2\text{O}\cdot\text{C}_2\text{H}_2$  is therefore 1:1.

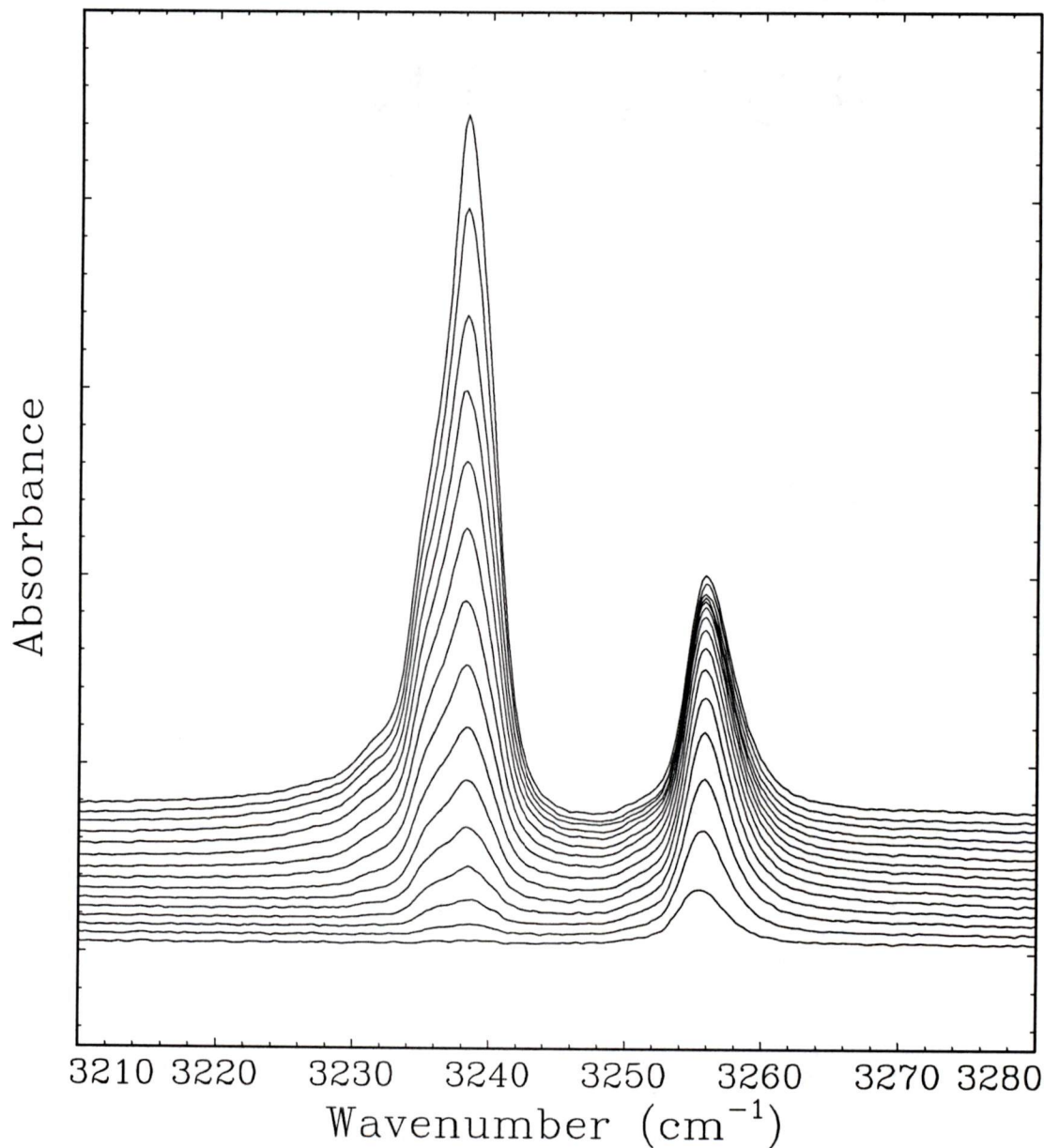


**Figure 5.13:** Growth of the nitrous oxide-acetylene binary phases showing the favourable growth of the  $\beta$  binary phase over the  $\alpha$  phase with additional pulses. The spectra represent the cryofilm deposited from an equimolar mixture of  $\text{N}_2\text{O}$  and  $\text{C}_2\text{H}_2$  with each successive spectrum representing an additional 100 ms pulse. The temperature of the window is 90 K and the interval between pulses is 240 seconds.

## 5.2 Nucleation and Growth of the Binary Phase

### 5.2.1 Cluster Formation in a Free Jet Expansion

Clusters have been characterized as assemblies of atoms or molecules bound together by bulk-phase intermolecular forces and ranging in size from a dimer up to micro-crystals or micro-droplets of many million particles [34]. In the early 1950's, Kantrowitz and Grey [35] suggested that a supersonic jet could be used in the place of the effusive flow field of the conventional oven beam in order to increase molecular beam intensities. Five years later, Becker, Bier and Henkes [36] published the first report on the formation of cluster beams from free jet expansion through a supersonic nozzle. In the past two decades, the field of cluster research has seen tremendous activity. Experimental and theoretical investigations on clusters, as intermediates between gas phase and condensed matter, are mainly focused on “(i) the characterization of the building blocks involved in nucleation and crystal growth processes, and (ii) the understanding of the emergence of bulk-like properties from clusters of increasing size.” [37]

In most studies involving molecular beams from supersonic jets, cluster formation is seen as a nuisance to be avoided. The generation of clusters in an expanding flow field for a given gas depends on: source pressure,  $P_0$ ; source temperature,  $T_0$ ; and the nozzle geometry. Therefore, considerable effort has gone into the effect of these variables upon complex formation in expanding supersonic jets [38–40]. Cluster

formation is promoted by increasing  $P_0$ , decreasing  $T_0$ , and using nozzles which give a less rapid expansion.

Figure 2.3 contains the schematic of four different types of nozzles which have been used in molecular beam studies. They have been labelled with the nomenclature of Hagen and Obert [38]. For the same  $\text{CO}_2$  source pressure, source temperature and throat diameter,  $d$ , the highest average cluster size was observed for the conical nozzle. A converging-diverging (Laval) nozzle gave the next largest clusters and a sonic nozzle produced the smallest average cluster size. Similarly, more recent studies [41] indicate that a conical nozzle is more efficient in producing large alkali metal clusters than a comparable sized cylindrical nozzle. These observations can be rationalized in terms of constrained expansion [7]. The lateral expansion is restricted by the diverging walls. Thus, there is a higher density at the time of cluster growth and more collisions are possible prior to termination of the expansion, resulting in larger clusters.

For any of these supersonic nozzles the following condensation model may be applied. Figure 5.14 shows the expansion isentrope of a condensing gas. The stagnation conditions ( $P_0, T_0$ ) are represented by point A. For ideal isentropic expansions, a gas expands adiabatically along an isentrope  $P \times T^n = \text{constant}$ . The gas follows this isentrope,  $P(T)$ , to point B. Because this is not an equilibrium process, some regions of the expansion zone become supersaturated. That is, the subsequent expansion continues to follow the isentrope rather than the equilibrium curve. This supersaturation leads to the formation of clusters at point C if there is sufficient time

remaining before collisions have essentially ceased. The formation of clusters leads to a drop in pressure, resulting in a collapse of the supersaturated state. Simultaneously, the expansion warms, due to the release of cohesive energy upon condensation, and gradually returns to the equilibrium line  $P_v(T)$ .

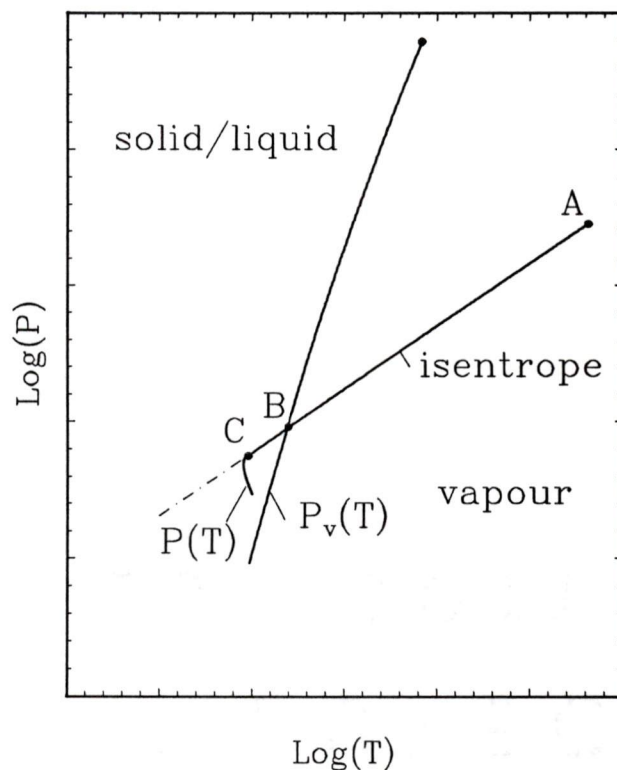


**Figure 5.14:** Log-log schematic showing the expansion isentrope and equilibrium vapour pressure of a condensing gas.

### 5.2.2 Cluster Growth as a Precursor to Binary Formation

In the present study, a 200  $\mu\text{m}$  diameter cylindrical nozzle was used at room temperature. The pressure inside the mixing chamber was 60 Torr and the gas pulse through

the solenoid valve was 500 milliseconds. In this time, the stagnation pressure reached nearly 60 Torr (see Figure 2.4).

An important constant used to determine the likelihood of the onset of significant clustering is  $P_0d$ , based on scaling laws proposed by Hagen [34]. Significant clustering of  $N_2$  occurs at  $P_0d$  values greater than 5 Torr·cm [42]. It is, therefore, reasonable to suggest that clustering should occur in the present arrangement since  $P_0d=1.2$  Torr·cm.

We can further show the likelihood of cluster formation using the pressure and temperature of the expansion flow which were approximated previously in Section 2.3.1. Figure 5.15 shows the  $CO_2$  pressure as a function of distance calculated from Equation 2.2 (using  $\gamma=9/7$ ). The second curve is the flat surface equilibrium vapour pressure of  $CO_2$  calculated from constants given in the CRC Handbook [5] incorporating the temperature of the expansion flow. Considering the condensation model discussed at the beginning of this section, the expanding gas will become supersaturated after the passing through the equilibrium line at  $x/d \approx 1.1$ . Soon after, clusters will begin to form. The pressure will further decrease as the expansion returns to the equilibrium line.

It is easy to see from Figure 5.15 that  $CO_2$  cluster formation is very likely using the present setup. One condition, which has not yet been discussed, which might prevent the condensation of  $CO_2$  (or  $C_2H_2$  or  $N_2O$ ) is the location of the Mach shock disk. This is the region where the overexpanded flow field is recompressed by a series of shocks

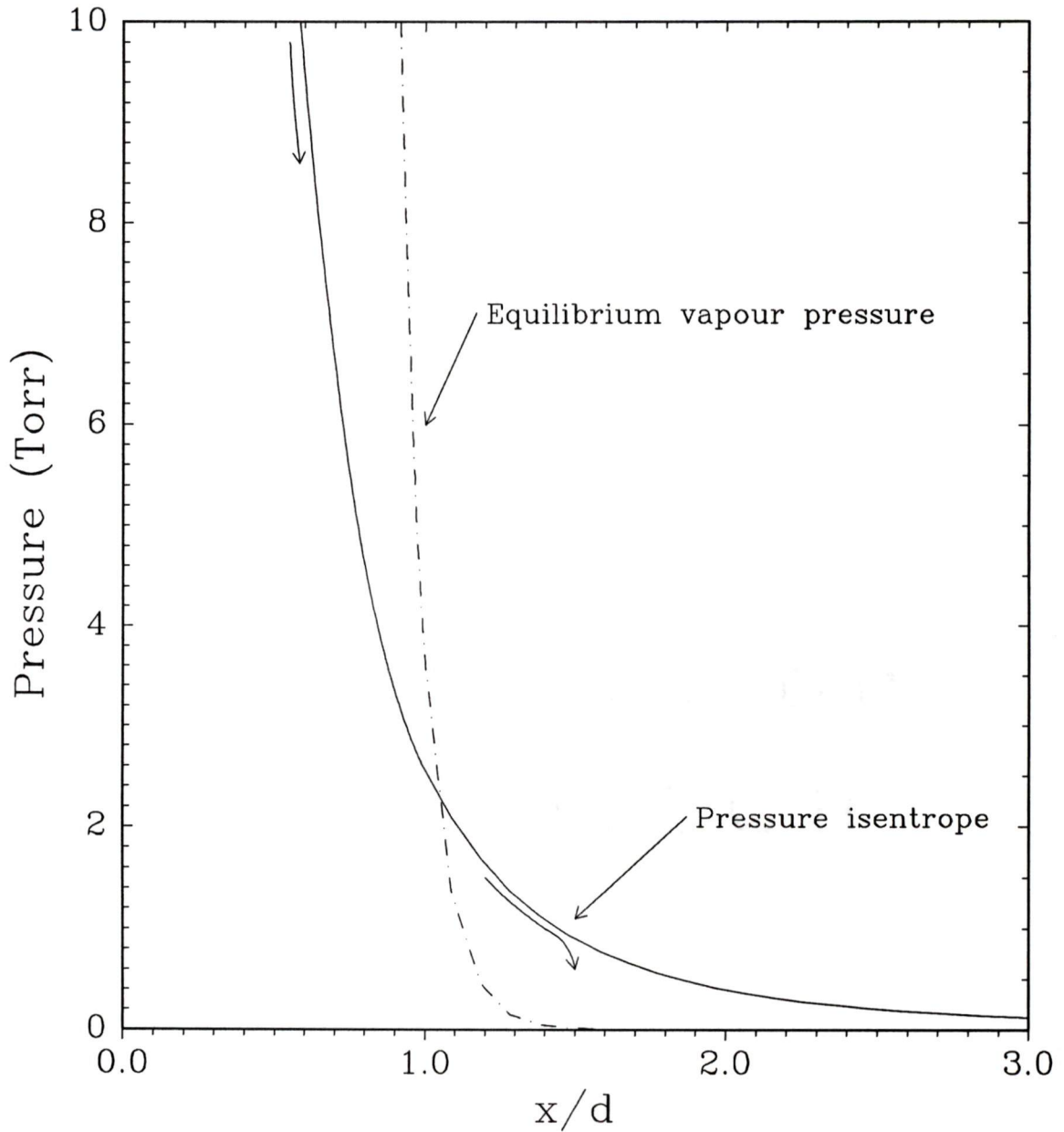


**Figure 5.15:** Free jet centerline  $\text{CO}_2$  pressure and equilibrium vapour pressure as a function of distance in source diameters. Free jet pressure is calculated from Equation 2.2 using the  $M$  values shown in Figure 2.5(a);  $\gamma = 9/7$ .

normal to the centerline flow. It is characterized by large density gradients. The Mach disk location, in nozzle throat diameters, is given by  $(x_M/d) = 0.67\sqrt{(P_0/P_b)}$ . It is near this region that the pressure is raised to the background pressure and the flow proceeds subsonically. The temperature of the flow field also rises as molecules collide with thermalized species returning from the walls. If clusters are present, they will begin to dissociate due to these collisions. Due to cryopumping, the background partial pressure of carbon dioxide, acetylene, or nitrous oxide near  $1 \times 10^{-4}$  Torr. The background pressure due to nitrogen is near  $1 \times 10^{-1}$ . This yields a pressure ratio of  $6 \times 10^2$  and a Mach disk location of  $x_M/d \approx 16$ . This is sufficiently far away to allow significant condensation to occur. The cooled window is located 30 mm ( $x/d = 150$ ) from the nozzle exit. Thus, the Mach disk shock occurs prior to the cooled window. This is sufficient distance for extensive cooling and clustering to occur. There is little distance left for thermalized species to warm the flow and fragment the clusters.

The initial condensation products resulting from the expansion are dimers as a result of three-bodied collisions. Symmetric dimers consisting of linear molecules with large quadrupole moments of the same sign are arranged in either slipped parallel or T-shaped geometries. For instance, the homomolecular  $C_2H_2$  dimer is T-shaped [43] while  $(N_2O)_2$  exhibits a slipped parallel geometry [44]. The carbon dioxide dimer is also slipped parallel [45] as shown experimentally and predicted by high level calculations [46]. This appears to be an exception. The higher oligomers as well as the most

stable crystalline phase of  $\text{CO}_2$  (fcc) exhibit structures that maximize the number of T-shaped interactions.

The energy of a quadrupole-quadrupole interaction is proportional to the product of the quadrupole moments. Thus, the T-shaped and slipped parallel geometries which are attractive for two quadrupole moments of the same sign are repulsive for asymmetric dimers containing two centrosymmetric molecules having quadrupole moments of opposite sign. The quadrupole-quadrupole interaction in the latter case strongly favours a symmetric parallel planar geometry. An example is the  $\text{CO}_2\text{-C}_2\text{H}_2$  dimer pictured in Figure 5.16. The same equilibrium structure for this heterodimer has been determined by two independent groups [40,47]. This same geometry is exhibited in the nitrous oxide-acetylene dimer [48].

Each of the above mentioned heterodimers are more strongly bound than either of their homomolecular counterparts. The stability of the symmetric parallel configuration can easily be visualized. The parallel configuration of the carbon dioxide-acetylene dimer places the positive hydrogen atoms near the negative oxygen atoms and the positive carbon atom opposite the  $\pi$  electron density of the alkyne bond. The same argument applies to the stability of the parallel nitrous oxide-acetylene dimer. It is well known [49] that the central nitrogen in  $\text{N}_2\text{O}$  has substantial  $\text{N}^+$  character, while the terminal N is quite negative.

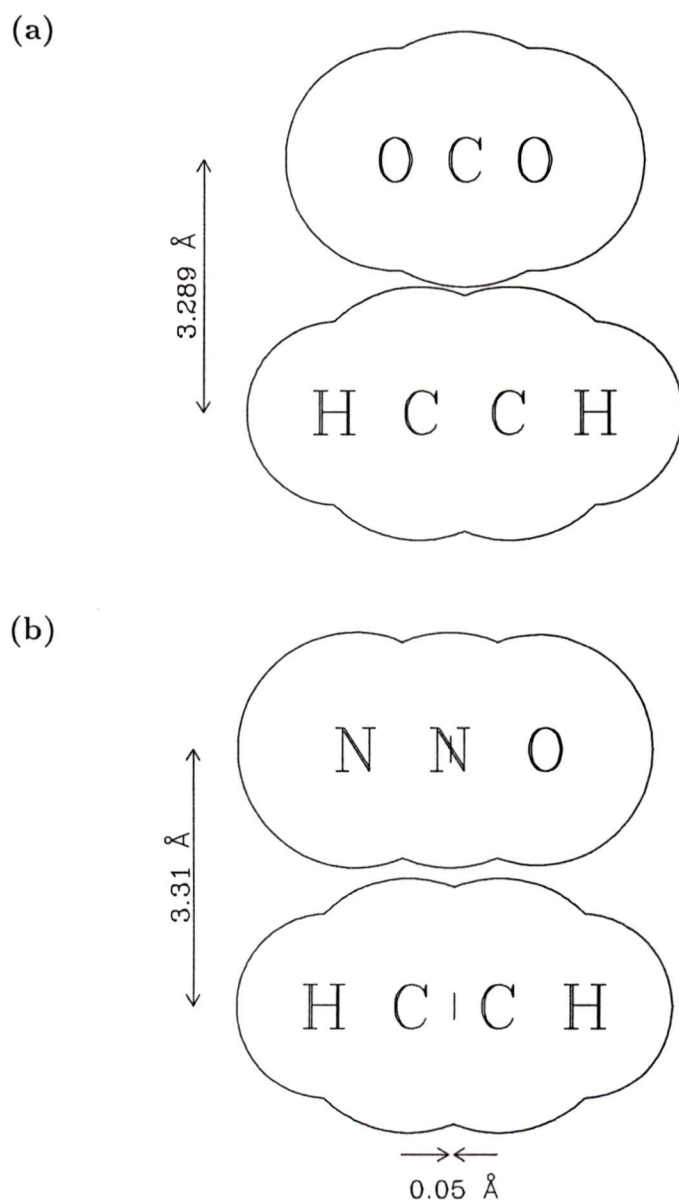


Figure 5.16: (a) Equilibrium Geometry of the  $\text{CO}_2 \cdot \text{C}_2\text{H}_2$  Dimer. (b) Equilibrium Geometry of the  $\text{N}_2\text{O} \cdot \text{C}_2\text{H}_2$  Dimer.

### 5.3 Discussion

In view of the complexity of the processes which occur between the nozzle orifice and the window, any comprehensive model of formation of the binary complexes is not possible. A speculative description of the nucleation, growth, structure, and decomposition of the binary complexes  $\text{CO}_2 \cdot \text{C}_2\text{H}_2$  and  $\alpha\text{-N}_2\text{O} \cdot \text{C}_2\text{H}_2$  may be given which accounts for the above observations.

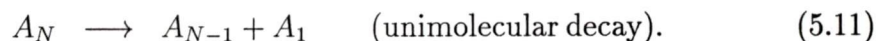
It has been shown that cluster formation is extremely likely in the present circumstances. The nucleation is a non-equilibrium process, so, rather than supersaturation in terms of equilibrium vapour pressure, the internal energy of the resulting dimer should be considered. The heterodimers  $\text{CO}_2 \cdot \text{C}_2\text{H}_2$  and  $\text{N}_2\text{O} \cdot \text{C}_2\text{H}_2$  have greater stabilization energies than their homomolecular counterparts. Thus, in the reaction



more energy needs to be removed by the third molecule if a heterodimer is formed: Heterodimerization likely occurs earlier on in the flow field than homodimerization. For a 50/50 mixture, the formation of a heterodimer is also statistically more favourable by a factor of two.

The reactions of N-size clusters that subsequently occur are:





The formation of homodimers may still occur, however, they are more likely to decay either by sputtering or by unimolecular decay; further reducing the chance that they reach the critical size necessary to continue growing without unimolecular decay being predominant. This model seems to fit the observation that the metastable phases form to the almost complete exclusion of the more stable phases.

The first product of condensation is the 1:1 heterodimer. Monomers add to this dimer adopting the same parallel configuration. This parallel arrangement is optimized by molecules having quadrupole of opposite sign, so a two-dimensional array is made up of alternating  $C_2H_2$  and  $CO_2$  (or  $N_2O$ ) molecules. The result is a hexagonal close packed array with the unit cell containing one  $C_2H_2$  molecule and one  $CO_2$  (or  $N_2O$ ) molecule. There are four attractive and two repulsive interactions. Thus, in the early stages, growth in this manner is energetically favourable.

As condensation proceeds, the energetically favourable two-dimensional array must eventually become unstable as the three-dimensional structure grows maintaining 1:1 stoichiometry. The size and morphology of the growing clusters prior to deposition are too difficult to determine. It is not known whether two-dimensional 'rafts' or spheres are the most common shape of the clusters.

Very minimal rearrangement occurs upon collision with the liquid nitrogen cooled window. Otherwise, relaxation into a more stable structure would likely happen at this stage. Due to rotational cooling in the expansion, motion along surfaces or grain boundaries as well as reorientation are minimized.

The  $\text{CO}_2 \cdot \text{C}_2\text{H}_2$  complex has been shown to be thermodynamically less stable than the pure phases. The binary phase formed under non-equilibrium conditions undergoes complete solid state conversion into pure phase  $\text{CO}_2$  and  $\text{C}_2\text{H}_2$ .

The nitrous oxide-acetylene system, however, has two binary phases. The phase  $\alpha\text{-N}_2\text{O} \cdot \text{C}_2\text{H}_2$  forms kinetically but converts to the more stable  $\beta\text{-N}_2\text{O} \cdot \text{C}_2\text{H}_2$ . No evidence exists to suggest that the pure phases of  $\text{N}_2\text{O}$  and  $\text{C}_2\text{H}_2$  are more stable than  $\beta\text{-N}_2\text{O} \cdot \text{C}_2\text{H}_2$ .

| Geometry                   | Type of Nucleation  | $n$                             |
|----------------------------|---------------------|---------------------------------|
| Linear problem:            |                     |                                 |
| Line                       | Athermal            | 1                               |
| Line                       | Thermal             | 2                               |
| Two-dimensional problem:   |                     |                                 |
| Ribbon                     | Athermal            | $\leq 1$                        |
| Ribbon                     | Thermal             | $\leq 2$                        |
| Circular                   | Athermal            | 3                               |
| Circular                   | Thermal             | 4                               |
| Circular                   | Thermal, exhaustion | $3 \rightarrow 2$               |
| Three-dimensional problem: |                     |                                 |
| Fibrillar                  | Athermal            | $\leq 1$                        |
| Fibrillar                  | Thermal             | $\leq 2$                        |
| Circular lamellar          | Athermal            | $\leq 2$                        |
| Circular lamellar          | Thermal             | $\leq 3$                        |
| Spherical                  | Athermal            | 3                               |
| Spherical                  | Thermal             | 4                               |
| Spherical                  | Thermal, exhaustion | $4 \rightarrow 3$               |
| Branching fibrillar        | Athermal/thermal    | $1, 2 \rightarrow \text{large}$ |
| Truncated sphere           | Athermal            | 2-3                             |
| Truncated sphere           | Thermal             | 3-4                             |

Table 5.2: Exponents of Time in the Avrami Equation.  
 These values have been collected from references [31–33]

## Chapter 6

### Summary

An effective method of preparation of binary acetylene containing crystals has been established. As a result, the stoichiometry of the  $\text{N}_2\text{O}\cdot\text{C}_2\text{H}_2$  complex as well as the  $\text{CO}_2\cdot\text{C}_2\text{H}_2$  complex have been determined. There is an understanding of the processes of formation as well as decomposition of these binary phases. This understanding arises from the infrared spectra collected in this study, ab initio calculations on the stabilization energy of small  $\text{CO}_2$  clusters [46], formation of binary dimers in a molecular beam [40, 47, 48] and formation of binary microcrystallites in a diffusive trapping cell [1].

Infrared spectroscopy is limited in giving any comprehensive morphological or structural information. Thus, further study of these binary complexes must include microscopy, X-ray crystallography and, possibly, electron diffraction. As the binary

phases are metastable the crystals would need to be prepared *in situ* by free jet expansion onto a cooled surface.

Stabilization energy calculations using ab initio assuming various configurations of 1:1 mixtures of CO<sub>2</sub> or N<sub>2</sub>O with C<sub>2</sub>H<sub>2</sub> would likely result in a more in-depth understanding of the stability of binary acetylene containing complexes as well as the most favourable structures. The difference in structure between  $\alpha$ -N<sub>2</sub>O·C<sub>2</sub>H<sub>2</sub> and  $\beta$ -N<sub>2</sub>O·C<sub>2</sub>H<sub>2</sub> may also be revealed.

The scope of the present study could be enlarged to include other binary mixtures. For instance, CS<sub>2</sub> may form a binary complex with C<sub>2</sub>H<sub>2</sub> since it is isostructural and isoelectronic with CO<sub>2</sub>.

In addition, a computer model could be used to further verify the proposed phase conversion mechanism.

# Bibliography

- [1] T.E. Gough and T. Wang, *Journal of Chemical Physics*, **102**(10), 3992(1995).
- [2] T. Wang, **Fourier Transform Infrared Spectroscopy of Molecular Aerosols Using the Diffusive Trapping Technique**, PhD thesis. University of Victoria, Victoria, 1996.
- [3] II-VI Optics Manual II-VI Incorporated: Saxonburg, Pennsylvania, 1991.
- [4] C.C. Lim, *Rev. Sci. Instrum.* **57**(1), 108(1986).
- [5] R.C. Weast and M.J. Astle, editors **CRC Handbook of Chemistry and Physics**, 63rd edition, CRC Press, Inc.: Boca Raton, Florida, 1982.
- [6] H. Murphy, **The Effects of Source Geometry on Free Jet Expansions**, PhD thesis. University of California, San Diego, 1984.
- [7] G. Scoles, editor **Atomic and Molecular Beam Methods (I)**, Oxford University Press: New York, 1988.

- [8] T.E. Gough, R.E. Miller, and G. Scoles, *Journal of Physical Chemistry* **85**(26), 4041(1981).
- [9] K.D. Möller and W.G. Rothschild, **Far-Infrared Spectroscopy**, Wiley-Interscience: Toronto, 1971.
- [10] E.G. Steward **Fourier Optics: an Introduction**, Ellis Horwood Limited: Chichester, England, 1983.
- [11] R.G. Bell, **Introductory Fourier Transform Spectroscopy**, Academic Press, 1972.
- [12] Bomem Inc., **Spectrophotometer System Manual**, Revision 2-0, 1981.
- [13] P.R. Griffiths, **Chemical Infrared Fourier Transform Spectroscopy**, John Wiley & Sons: New York, 1975.
- [14] J. Chamberlain, **The Principles of Interferometric Spectroscopy**, John Wiley & Sons: New York, 1979.
- [15] J.A. Barnes, T.E. Gough, and M. Stoer, *Journal of Chemical Physics*, **95**(7), 4840 (1991).
- [16] G. Glockler and M.M. Renfrew, *Journal of Chemical Physics*, **6**, 340 (1938).
- [17] G.L. Bottger and D.F. Eggers, J.R., *Journal of Chemical Physics*, **40**(7), 2010 (1964).

- [18] E.P. Dudek, *Specrophotometric Determination of the Formula of a Complex Ion*, Willard Grant Press: Boston, 1977.
- [19] David A. Dows and Vincenzo Schettino, *Journal of Chemical Physics*, **58**11, 5009 (1973).
- [20] J. Vander Auwera, D. Hurtmans, M. Carleer, and M. Herman, *Journal of Molecular Spectroscopy*, **157**, 337 (1993).
- [21] T.A. Wiggins, E.K. Plyler and E.D. Tidwell, *Journal of the Optical Society of America* **51**, 1219 (1961).
- [22] G. Herzberg, **Infrared and Raman Spectra**, Van Nostrand Reinhold Company, New York, 1945.
- [23] E.E Bell and H.H. Nielsen, *Journal of Chemical Physics*, **18**, 1382 (1950).
- [24] G.L. Bottger and D.F. Eggers, J.R., *Journal of Chemical Physics*, **40**(7), 2010 (1964). Reference 9 within.
- [25] M. Falk and P.F. Seto, *Canadian Journal of Spectroscopy*, **31**(5), 134 (1986).
- [26] K.N. Rao, **Molecular Spectroscopy: Modern Research (II)**, Academic Press, Inc.: New York, 1976.
- [27] R. Fuchs, *Physics Review B* **11**(4), 1732(1975).
- [28] G. Mie, *Ann. Phys.* **25**, 377(1908).

- [29] David A. Dows, *Journal of Chemical Physics*, **24**(4), 745 (1957).
- [30] J. Bigeleisen and L. Friedman, *Journal of Chemical Physics*, **18**, 1656(1950).
- [31] M. Avrami, **Kinetics of Phase Change II** *Journal of Chemical Physics*, **8**, 212 (1940).
- [32] Hans George Elias, **Macromolecules**, translated from German by John W. Stafford, Plenum Press: New York, 1977.
- [33] C.N.R Rao and K.J. Rao, **Phase Transitions in Solids: An Approach to the Study of the Chemistry and Physics of Solids.**, McGraw-Hill Inc.: Toronto, 1978.
- [34] O. F. Hagena, *Surface Science*, **106**, 101(1981).
- [35] A. Kantrowitz and J. Grey, *Review of Scientific Instruments*, **22**, 328(1951).
- [36] E.W. Becker, K. Bier, and W. Henkes, *Z. Physik*, **146**, 333(1956).
- [37] E. Francisco, J. M. Recio, and A. Martin Pendas, *Journal of Chemical Physics*, **103**(1), 432(1995).
- [38] O. F. Hagena, and W. Obert, *Journal of Chemical Physics*, **56**(5), 1793(1972).
- [39] R. Campargue *Journal of Physical Chemistry*, **88**, 4466(1984).
- [40] Z.S. Huang and R.E. Miller, *Chemical Physics*, **132**, 185(1989).

- [41] M. Kappes, M. Schär, P. Radi, and E. Schumacher *Journal of Chemical Physics*, **84**, 1863(1986). M. Kappes, M. Schär, E. Schumacher, and P. Vayloyan, *Z. Physik* **5**, 359(1987).
- [42] H. Beijerinck and N. Verster, *Physica*, **111C**, 327(1981).
- [43] Z.S. Huang and R.E. Miller, *Journal of Chemical Physics*, **89**, 5408(1988).
- [44] D.G. Prichard, R.N. Nandi, J.S. Muentner and B.J. Howard, *Journal of Chemical Physics*, **89**(3), 1245 (1988) (reference 9 within).
- [45] M.A. Walsh, T.H. England, T.R. Dyke and B.J. Howard, *Chemical Physics Letters*, **142**, 265 (1987).
- [46] E. Knözinger, and P. Beichert, *Journal Physical Chemistry*, **99**, 4906(1995).
- [47] D.G. Prichard, R.N. Nandi, J.S. Muentner and B.J. Howard, *Journal of Chemical Physics*, **89**(3), 1245 (1988).
- [48] T.A. Hu, Ling Hong Sun, and J.S. Muentner, *Journal of Chemical Physics*, **95**(3), 1537 (1991).
- [49] C.H Townes and A.L. Schawlow, **Microwave Spectroscopy**, Dover Publications Inc.: New York, 1975.
- [50] K.F. Palmer, M.E. Mickelson, and K.N. Rao, *Journal of Molecular Spectroscopy*, **44**, 131 (1972).

- [51] S. Dushman and J.M. Lafferty, **Scientific Foundations of Vacuum Technique**, John Wiley and Sons: New York, 1962.
- [52] G. Scoles, editor **Atomic and Molecular Beam Methods (II)**, Oxford University Press: New York, 1991.
- [53] D.G. Prichard, R.N. Nandi and J.S. Muentner, *Journal of Chemical Physics* **89**, 115 (1988).
- [54] M. Falk, *Journal of Chemical Physics*, **86**(2), 560 (1987).
- [55] L.S. Bartell, L. Harsanyi, T.S. Dibble, and P.L. Lennon, *Journal of Physical Chemistry*, **94**, 6009 (1990).
- [56] U.R. Evans, *Transactions of the Faraday Society*, **41**, 365 (1945).
- [57] Y.A Schwartz, A.Ron, and S. Kimel, *Journal of Chemical Physics*, **51**, 1666 (1969).
- [58] B.E. Wood, and J.A. Roux, *Journal of the Optical Society of America* **72**(6), 720 (1982).
- [59] H. Yamada, and W.B. Person, *Journal of Chemical Physics*, **41**(8), 2478 (1964).
- [60] G.E. Ewing and De T. Sheng, *Journal of Physical Chemistry* **92**(14), 4063(1988).
- [61] T. Dunder and R.E. Miller, *Journal of Chemical Physics* **93**(5), 3693(1990).

- [62] P.M.A. Sherwood, **Vibrational Spectroscopy of Solids** Cambridge University Press, New York, 1972.

# VITA

Surname: Rowat

Given Names: Terence Edward

Place of Birth: Williams Lake, British Columbia Date of Birth: 17<sup>th</sup> of March, 1969

## Educational Institutions Attended:

University of Victoria 1990 to 1996

Cariboo College 1989 to 1990

## Degrees Awarded:

B.Sc. University of Victoria 1993

## Honours and Awards:

## Publications:

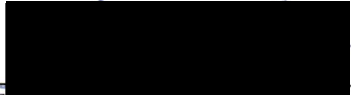
## PARTIAL COPYRIGHT LICENSE

I hereby grant the right to lend my thesis to users of the University of Victoria Library, and to make single copies only for such users or in response to a request from the Library of any other university, or similar institution, on its behalf or for one of its users. I further agree that permission for extensive copying of this thesis for scholarly purposes may be granted by me or a member of the University designated by me. It is understood that copying or publication of this thesis for financial gain shall not be allowed without my written permission.

Title of Thesis :

Stoichiometry and Stability of Binary Phase Crystals Formed  
Between Acetylene and Nitrous Oxide/Carbon Dioxide

Author:

  
Terence Edward Rowat

Date

*May 27/97*